

Ocean carbon sink assessment via temperature and salinity data assimilation into a global ocean biogeochemistry model

Frauke Bunsen¹, Judith Hauck¹, Sinhué Torres-Valdés¹, and Lars Nerger¹

¹Alfred-Wegener-Institut, Helmholtz Zentrum für Polar- und Meeresforschung, Bremerhaven, Germany

Correspondence: Frauke Bunsen (frauke.bunsen@awi.de)

Abstract. Global ocean biogeochemistry models are frequently used to derive a comprehensive estimate of the global ocean carbon uptake. These models are designed to represent the most important processes of the ocean carbon cycle, but the idealized process representation and uncertainties in the initialization of model variables lead to errors in their predictions. Here, observations of ocean physics (temperature and salinity) are assimilated into the ocean biogeochemistry model FESOM-REcoM over the period 2010-2020 to study the effect on the air-sea CO₂ flux and other biogeochemical variables. ~~While the free running model already represents~~ The assimilation nearly halves the model-observation differences in sea surface temperature and salinity ~~rather well, the assimilation further improves it and hence influences the~~, with modest effects on the modeled ecosystem and CO₂ fluxes. The ~~assimilation has mainly regional~~ main effects on the air-sea CO₂ flux, ~~with the occur on small scales in highly dynamic regions, which pose challenges to ocean models.~~ The largest imprint of assimilation is in the Southern Ocean during winter. South of 50°S, winter CO₂ outgassing is reduced and thus the mean regional CO₂ uptake increases by 0.18 Pg C yr⁻¹ through the assimilation. Other particularly strong regional effects on the air-sea CO₂ flux are located in the area of the North Atlantic Current. Yet, the effect on the global ocean carbon uptake is a comparatively small increase by 0.05 Pg C yr⁻¹ induced by the assimilation, yielding a global mean uptake of ~~2.78 Pg C yr⁻¹~~ 2.78 Pg C yr⁻¹ for the period 2010-2020.

15 *Copyright statement.* TEXT

1 Introduction

The ocean plays a pivotal role in regulating the global carbon budget and thereby mitigating the impacts of anthropogenic carbon dioxide (CO₂) emissions on the Earth's climate. Since the 1960s, the ocean has absorbed consistently around 25% of anthropogenic CO₂ emissions annually (Friedlingstein et al., 2023) and has cumulatively taken up 26–34% of fossil and land-use change ~~CO₂~~ CO₂ emissions since the onset of the ~~Industrial Revolution~~ industrial revolution (Crisp et al., 2022). However, quantification of air-sea CO₂ flux still remains challenging. Air-sea CO₂ flux is usually inferred from the gradient of partial pressure (pCO₂) or fugacity (fCO₂) of CO₂ across the air-sea interface (Wanninkhof, 2014). Yet, during 2010-2020, which constitutes the best-sampled decade in terms of surface ocean pCO₂ observations so far, observations covered merely

3% of the monthly global ocean (as calculated from the $1^\circ \times 1^\circ$ -gridded SOCAT product; Bakker et al., 2016). While the North Atlantic and North Pacific are comparably well observed, data remain scarce in vast regions, such as the Indian Ocean, South Pacific and areas south of 30°S during austral winter, where less than 1% of SOCAT grid cells have been sampled. Although these observations are thought to be representative of a larger area (Jones et al., 2012; Hauck et al., 2020), challenges in deriving a comprehensive global estimate of the global ocean CO_2 uptake arise due to substantial spatial and temporal pCO_2 variations and potential biases induced by the irregular sampling pattern (Denvil-Sommer et al., 2021; Gloege et al., 2021; Hauck et al., 2023b). Particularly in the Southern Ocean, the uncertainty is considerable (Gerber et al., 2009; Gloege et al., 2021), where estimates of the mean flux ~~deviate by 14–26% (Hauck et al., 2023b)~~ range from -0.37 to $-1.25 \text{ Pg C yr}^{-1}$ for the period 2010–2018 (data provided by Hauck et al., 2023b).

~~Initially~~In the Global Carbon Budget, estimates of the ocean carbon sink were initially derived from hindcast simulations of global ocean biogeochemistry models (GOBMs) (Le Quéré et al., 2009; Wanninkhof et al., 2013; Hauck et al., 2020). More recently, air-sea CO_2 flux estimates were added based on regression and machine learning techniques, interpolating pCO_2 observations to achieve global coverage through advanced statistical methods (referred to as pCO_2 products; Rödenbeck et al., 2015). Furthermore, atmospheric transport models that ingest atmospheric CO_2 measurements were employed to estimate the ocean carbon uptake (~~referred to as atmospheric inversions; Peylin et al., 2013~~)(referred to as atmospheric inversions; Peylin et al., 2013). Although the different estimation methods have provided valuable and robust insights into large-scale patterns of oceanic carbon uptake (Gruber et al., 2009), discrepancies have emerged. Assessments based on pCO_2 -products tend to yield larger estimates of the ocean carbon sink, with stronger trends towards more uptake, compared to estimates based on models (Friedlingstein et al., 2023; Terhaar et al., 2022). The larger estimates are supported by ocean interior observations (Müller et al., 2023), atmospheric oxygen data and atmospheric inversions (Friedlingstein et al., 2023). For the years 2010–2020, pCO_2 products included in the Global Carbon Project suggest a mean oceanic sink of $3.0 \pm 0.4 \text{ Pg C yr}^{-1}$, while the ~~model-mean-mean~~ of Global Carbon Project GOBMs is $2.5 \pm 0.4 \text{ Pg C yr}^{-1}$, ~~with trends of~~ (data provided by Friedlingstein et al., 2023). Trends over the same time period are $0.7 \text{ Pg C yr}^{-1} \text{ dec}^{-1}$ and $0.3 \text{ Pg C yr}^{-1} \text{ dec}^{-1}$, respectively~~(data provided by Friedlingstein et al., 2023)~~.

Machine learning estimates ~~on the one hand, perform better~~ perform well when trained with sufficient data ~~such as in the northern hemisphere~~ (Gloege et al., 2021). However, ~~as with other methods,~~ their performance is less reliable in data-sparse areas. Particularly in the Southern Ocean, many pCO_2 ~~products~~ products show diverging results from one another and are likely biased towards more ocean uptake (Hauck et al., 2023b). However even in parts of the North Pacific, which is undersampled in the 2010s, some pCO_2 products show spurious decadal trends (Mayot et al., 2024). Models provide process-driven estimates of the CO_2 flux across the entire global ocean, drawing from the theory of ocean dynamics, biological and chemical processes (Hauck et al., 2020; Fennel et al., 2022). Despite the growing confidence in our mechanistic understanding of the ocean carbon cycle (Crisp et al., 2022), models are also ~~subjected~~ subject to uncertainty. This uncertainty stems from uncertainties in model parametrizations, model spin-up and initial conditions, unresolved sub-gridscale processes and uncertainties in the atmospheric forcing (Hauck et al., 2020; Terhaar et al., 2024).

Data assimilation (DA) ~~has been~~ can be employed to address the emerging discrepancies between ~~data products and models~~. So far, DA studies of the air-sea CO₂ flux ~~pCO₂ products and models~~ (Carroll et al., 2020). Several studies assimilating ocean surface pCO₂ have focused on specific regions (e.g. the Southern Ocean; Verdy and Mazloff, 2017) (e.g., a baseline state of air-sea CO₂ flux, few years (e.g. 2009-2011; Brix et al., 2015) (e.g., optimized biogeochemical initial fields for the period 2009-2011 in Brix et al., 2015) or the climatological mean state (e.g. Gerber et al., 2009); apart from a single multidecadal study covering the global ocean (Carroll et al., 2020). In each of these studies, an Adjoint or Green's Function DA approach is used to determine optimised boundary conditions, forcing terms and/or parameter values for the simulation. (e.g., corrections of large-scale pCO₂ model biases in White

60 These studies capture well the assimilated pCO₂ observations, while obeying physical laws and biogeochemical (BGC) equations. Data assimilation also provides a better understanding of various components of the ocean carbon cycle, such as the transport of anthropogenic CO₂ in the ocean (e.g., a reconstruction of anthropogenic carbon storage since 1770 in Gerber et al., 2009), regional and interannual variability of the air-sea CO₂ flux (e.g., global reanalysis in Ford and Barciela, 2017; Carroll et al., 2020; Valsala, the biological carbon pump (e.g., carbon export at a nutrient-rich and nutrient-poor site and estimation of BGC parameters related to air-sea

70 and specific ecosystems (e.g., the North West European Shelf ecosystem in Ciavatta et al., 2016, 2018). So far, however, there is no data assimilation product that provides a long-term, annually updated estimate of global ocean CO₂ uptake.

While previous studies indicate that the available BGC observations, when assimilated in isolation, are too sparse to constrain the modeled carbon cycle (Verdy and Mazloff, 2017) (Verdy and Mazloff, 2017; Spring et al., 2021), the assimilation of physical variables is expected to have a significant indirect effect on the modeled CO₂ uptake because upwelling and

75 subduction of DIC, as well as the physical transport of other biogeochemical tracers, will be affected air-sea CO₂ fluxes (Bernardello et al., 2024). This is because the uptake of atmospheric CO₂ depends ultimately on the modeled physical carbon transport between the surface, the mixed layer and the deep ocean in the form of dissolved inorganic carbon (DIC) through mixing, upwelling and subduction (Doney et al., 2004). According to current knowledge, ocean physics is the dominant driver of interannual variability in the of the global air-sea CO₂ flux (Doney et al., 2009; Keppler and Landschützer, 2019; Mayot et al., 2023; Lia

80 . Furthermore, in GOBMs, well-constrained physics are particularly important to capture the ocean storage of anthropogenic carbon (C_{ant}), as the rate of anthropogenic CO₂ uptake depends ultimately on and also responsible for stagnation and acceleration of the modeled physical carbon transport from the CO₂ uptake on decadal scales (Doney et al., 2009; Keppler and Landschützer, 2019; Mayot et al., 2023). Related to the strong control that physics exert on the interannual variability of air-sea interface across the mixed layer into the deep ocean in the form of dissolved inorganic carbon (DIC) (Davila et al., 2022). It was shown CO₂ fluxes, it was shown

85 in one idealized study that assimilating ocean physics at the initial state of a model simulation has a stronger and more positive impact on the modeled carbon cycle on interannual time-scales than assimilating the BGC initial state (Fransner et al., 2020). Therefore the question arises which processes are most important when altered physics change CO₂ fluxes in DA approaches. We However, the relative importance of uncertainties in physical and biogeochemical fields generally remains an open research question (e.g. Séférian et al., 2014; Li et al., 2016; Lebehot et al., 2019). Therefore, we here use ensemble-based data assimilation of ocean physics into a global ocean biogeochemistry model aiming to improve the modeled air-sea CO₂ flux for the years 2010-2020. For assimilation we use an ensemble Kalman filter variant (Nerger et al., 2012). With this approach, we describe the impact of continuously assimilating ocean physics this, we continuously assimilate temperature and salinity observations from

~~remote-sensing at the surface and from in-situ profile measurements for eleven years on the model's air-sea CO₂ flux. Here, we identify the mechanisms of how physics DA affects the modeled air-sea CO₂ flux, differentiating between the thermally, DIC- and alkalinity induced components and changes in mixing, and lateral and vertical transport and update the modelled temperature, salinity, horizontal velocities and sea surface height, using an ensemble Kalman filter variant (Nerger et al., 2012)~~

~~An accurate representation of ocean physics is a prerequisite, but not necessarily sufficient for a realistic simulation of the CO₂ flux. Coupled ecosystem models are adapted to the associated physics. Several difficulties are associated with physics DA into GOBMs. A common issue is erroneous equatorial upwelling leading to unrealistically high biological productivity in the tropics (Park et al., 2018; Gasparin et al., 2021; Raghukumar et al., 2015). Furthermore, any coupled ecosystem model is adapted to its associated physical model with its strengths and weaknesses through carefully selected parameter values. Furthermore, the natural carbon cycle in models is tuned to an equilibrium for the physical model state at pre-industrial conditions without DA, and it was shown that the and a spin-up to near-equilibrium. Accordingly, the modeled carbon cycle may react very sensitive to deviations from this physical state, leading the physical state that is typical for this model (Kriest et al., 2020; Spring et al., 2021). Potentially, this leads to biases in the carbon cycle through data assimilation (Spring et al., 2021) physics DA. The question therefore arises as to what extent an ecosystem model coupled to a data-assimilated physical model also represents a more realistic biogeochemistry. We will present cases where physics data assimilation leads to worse and better agreement with BGC observations, and which mechanisms drive the response of the CO₂ flux in physics DA approaches. One possible driver is the physical transport of DIC and alkalinity because velocities and diffusivity are changed by the DA, affecting in particular the upwelling of carbon-rich waters and subduction, which is important to capture the ocean storage of anthropogenic carbon (Davila et al., 2022). Furthermore, physics DA may change pCO₂ directly through its temperature-dependence, an effect emphasized by Verdy and Mazloff (2017). Additionally, the modelled biological pump might be altered, for example through the temperature-dependency of phytoplankton growth or through effects of stratification on nutrient availability.~~

~~In this study, we describe the response of the model's air-sea CO₂ flux to physics DA and identify the underlying mechanistic drivers. To this end, we differentiate between the thermally, DIC- and alkalinity induced components and changes in lateral and vertical transport through mixing and advection. We focus, firstly, on the global air-sea CO₂ flux. Secondly, we investigate the Southern Ocean given the relevant impact of DA in Southern Ocean winter in our study. Thirdly, we present regions in the North Atlantic given observational coverage and relevant local processes there.~~

2 Methods

2.1 Model FESOM-REcoM

The oceanic model component, FESOM2.1, computes the advection, diffusion, and mixing of passive biogeochemical tracers. The model is based on hydrostatic primitive equations under the Boussinesq approximation and utilizes a finite-volume discretization approach with surface triangles projected vertically to form prisms. Salinity (S), temperature (T), and biogeochem-

ical (~~BGC~~) tracers are located at the vertices of triangles (nodes), while the horizontal velocities are centered at the triangles (elements). The model allows for a variable mesh resolution ([see Section 2.2](#)) and incorporates parametrizations for diffusion and eddy-stirring along isoneutral surfaces, for which parametrized mixing is scaled by mesh resolution (Danilov et al., 2017). Vertical mixing is parametrized through the KPP scheme and the mixing depth is specified through a ~~boundary-layer~~ [boundary layer](#) (the layer of active mixing, which may have a vertical structure because the mixing of all properties across the layer is not instantaneous), with an additional vertical mixing scheme used in the Southern Ocean ([Monin–Obukhov parametrization](#), [Timmermann and Beckmann, 2019](#)). The surface salinity (SSS) is restored towards ~~climatology and sealed by a fictional flux at the ocean surface of 0.1m/day~~ [the World Ocean Atlas climatology through a fictional surface flux with \$v_{SSS} = 50\text{ m}/300\text{ days}\$ according to equation 1 and as in \[Gürses et al. \\(2023\\)\]\(#\):](#)

$$135 \quad \frac{(SSS_{\text{clim}} - SSS_{\text{model}}) * v_{SSS} * (h_{\text{surf}})^{-1}}{\text{with surface-layer width } h_{\text{surf}}} \quad (1)$$

[with surface-layer width \$h_{\text{surf}}\$](#) . A detailed description of FESOM2.1 ~~is provided by Danilov et al. (2017)~~ and a model assessment ~~by~~ [are provided by Danilov et al. \(2017\) and Scholz et al. \(2019, 2022\)](#).

The ocean biogeochemistry component, the Regulated Ecosystem Model version 3 (REcoM3), describes processes in the ocean carbon cycle and represents oceanic carbon in the form of dissolved inorganic carbon (~~DIC~~), dissolved organic carbon (~~DOC~~), plankton and detritus ([Gürses et al., 2023](#)). REcoM3 contains 28 BGC tracers (listed in Appendix Table A1). There are two phytoplankton groups: diatoms and small phytoplankton with implicit representation of calcifiers; two zooplankton groups: mixed and polar macro zooplankton ([Karakuş et al., 2021](#)); and two classes of detritus: ~~fast and slow sinking~~. REcoM3 includes variable intracellular stoichiometry with ratios of C:N:Chl:CaCO₃ for the small phytoplankton and C:N:Chl:Si for diatoms, which is propagated to zooplankton and detritus ([Schartau et al., 2007](#); [Hohn, 2008](#)). The publicly available Routines [To Model The Ocean Carbonate System \(moesy2.0\) \(Orr and Epitalon, 2015\)](#) ([mocsy2.0, Orr and Epitalon, 2015](#)) are used to compute pCO₂ and air-sea CO₂ flux, employing the gas-exchange parameterization of [Wanninkhof \(2014\)](#). Alkalinity is restored by a fictional surface flux of ~~10m/yr~~ [10 m yr⁻¹ \(as in \[Hauck et al., 2013\]\(#\); \[Schourup-Kristensen et al., 2014\]\(#\); \[Gürses et al., 2023\]\(#\)\)](#). The current model version FESOM2.1–REcoM3 was assessed by [Gürses et al. \(2023\)](#) and previous versions were evaluated and applied in global and regional studies of the ocean carbon cycle and planktonic ecosystems ([Hauck et al., 2013](#); [Schourup-Kristensen et al., 2014](#); [Hauck et al., 2020](#); [Karakuş et al., 2021](#)).

2.2 [Simulation set-up](#)

[The model setup for both simulations closely follows \[Gürses et al. \\(2023\\)\]\(#\). The mesh resolution is nominally 1 degree, ranging between 120 km and 20 km with enhanced resolution in the equatorial belt and north of 50°N \(126858 surface nodes\). It has 47 vertical layers with thickness ranging from 5 m at the surface to 250 m in the deep ocean, as described by \[Scholz et al. \\(2019, CORE mesh\\)\]\(#\)](#). [The model time step is 45 minutes. For atmospheric forcing, JRA55-do v.1.5.0 is used, a reanalysis product tailored for driving ocean-sea-ice models \(\[Tsujino et al., 2018\]\(#\)\). The atmospheric CO₂ mixing ratio \(xCO₂\) values were taken from the Global Carbon Budget \(\[Joos and Spahni, 2008\]\(#\); \[Ballantyne et al., 2012\]\(#\); \[Friedlingstein et al., 2023\]\(#\)\). We use model restart fields from \[Gürses et al. \\(2023\\)\]\(#\) where the model was spun-up by repeating the year-1961 JRA forcing for 189 years with preindustrial](#)

atmospheric CO₂ conditions, followed by a period from 1800 to 1957 with increasing atmospheric CO₂. Subsequently, simulations
160 were continued with historical JRA forcing from 1958 to 2009. During the assimilation window (2010-2020), we conduct two
ensemble simulations to study the impact of data assimilation (DA): one without DA (referred to as FREE) and another identical
setup applying DA (referred to as ASML). For each simulation, the ensemble mean for the following variables is written as
output: temperature, salinity, velocity, boundary-layer depth, surface pCO₂, DIC, alkalinity, nutrients, chlorophyll, net primary
production and biological export through sinking of detritus at 190 m. For the year 2020, additional output is available for
165 individual ensemble members, mixed-layer depth, physical sources or sinks of DIC and alkalinity through horizontal and
vertical advection and diffusion, and biological net sources or sinks of DIC and alkalinity through combined processes: For
DIC, the net biological term is the sum of photosynthesis, respiration, remineralization of dissolved organic carbon, and
formation and dissolution of calcite (Gürses et al., 2023, equation A6). For alkalinity, the net biological term is the sum of
nitrogen assimilation and remineralization, and formation and dissolution of calcite (Gürses et al., 2023, equation A7).

170 2.3 Data Assimilation

2.3.1 Assimilated observations

The assimilated observations are sea surface temperature (SST), sea surface salinity and profiles of temperature and salinity.
The assimilated SST observations are from the Operational Sea Surface Temperature and Ice Analysis (OSTIA) data set
(CMEMS Marine Data Store; Good et al., 2020; Donlon et al., 2012; Stark et al., 2007). OSTIA provides daily gap-free maps
175 of SST at a horizontal resolution of $0.05^\circ \times 0.05^\circ$, compiled from in-situ and satellite data from infrared and microwave
radiometers. The OSTIA observations were averaged to the FESOM2.1 model grid because their spatial resolution is higher
than the nominal resolution of the model grid. An observation error standard deviation of 0.8°C is prescribed for the DA
following Nerger et al. (2020). Observations are excluded in the DA process if the difference between the model and observation
exceeds three times the observation error standard deviation, thus 2.4°C , and at grid points with sea ice in the model, as in
180 Tang et al. (2020) and Mu et al. (2022). This exclusion keeps the model stable despite large differences between model and
observations at these sites, in particular as water temperature and salinity develop differently under sea ice than under the
influence of the atmosphere (Tang et al., 2020). Instead, a ‘gentler’ correction is made by assimilating neighboring points.
After the initial phase, about 7% of SST observations are excluded because of the 2.4°C -threshold. Nevertheless, the data
assimilation still has a strong effect in areas where these large model-observation discrepancies are typically found (North
185 Atlantic, Japan and Southern Ocean).

The assimilated SSS data is taken from the European Space Agency (ESA) Sea Surface Salinity Climate Change Initiative
(CCI) v03.21 data set (Boutin et al., 2021). ESA-CCI contains daily data at a spatial resolution of 50 km, albeit not capturing
temporal variability below weekly. The ESA-CCI observations are averaged to the FESOM2.1 model grid. We prescribe a
constant observation error standard deviation of 0.5 psu following Nerger et al. (2024). Like for the SST data, SSS observations
190 are excluded at locations where sea ice is present in the model.

The assimilated temperature and salinity profiles are taken from the EN.4.2.2 data set (Good et al., 2013). The EN4 dataset contains quality-controlled profiles from various in-situ ocean profiling instruments. To assimilate the profiles, the observations are assigned to the respective model layers (depth range) in the vertical. In the horizontal, the model values are computed as the average of the grid points of the triangle enclosing the observation. The observation error standard deviation is set to 0.8°C for temperature and to 0.5 psu for salinity, as in Tang et al. (2020).

2.3.2 Assimilation method and implementation

For the assimilation, we use the Localized Error Subspace Transform Kalman Filter (LESTKF, Nerger et al., 2012). The LESTKF incorporates new observations as they emerge by updating the previous estimate of the state sequentially updates the model forecast, incorporating observations when and where available. The model state and error covariance are represented by an ensemble simulation. Thereby, the assimilation of temperature and salinity affects the state of the physical model in its whole, including the horizontal velocities and sea-surface height. A review of the LESTKF and other filters frequently used in geophysics can be found in Vetra-Carvalho et al. (2018). The assimilation is implemented using the Parallel Data Assimilation Framework (PDAF2.1), a software environment for data assimilation. PDAF is an open source project and provides fully implemented DA algorithms (Nerger et al., 2020, pdaf.awi.de). The current implementation builds on the works of Mu et al. (2022) who used DA of ocean temperature and salinity for sea-ice forecasts with FESOM2.0 coupled to an atmospheric model, and Tang et al. (2020) who studied the dynamic impact of oceanic DA into FESOM1.4 onto a coupled atmospheric component.

With localization of the LESTKF, observations are weighted by distance, thereby avoiding the model being the observation error is increased for an increasing horizontal distance between an observation and a model grid point, which weighs down the influence of a more distant observation. This avoids that the model is influenced by observations at distant locations through spurious ensemble estimated correlations. We use a localization radius of 200 km and choose a 5th-order polynomial weighting function that mimics a Gaussian function (Gaspari and Cohn, 1999). We apply daily analysis steps at 0 UTC model time, assimilating all available observations for the day. The DA process only directly updates the physical model variables temperature, salinity, horizontal velocities and sea surface height. After each assimilation step, corrections are applied to the analysis state to ensure the consistency of model physics: Salinity is set to a minimum value of zero and temperature to a minimum value of -2°C , if necessary. The the value is otherwise below. The increment of sea surface height (SSH) update is limited to two standard deviations of the ensemble. While in the simulation the correction was necessary for about 10% of SSH updates and 0.01% of temperature values at each step, the correction of salinity was never required. The analysis step is followed by an ensemble forecast of 1 day.

The ensemble size is 40, a compromise to balance computational resources while ensuring a sufficiently large ensemble with enough variability even in the deep ocean. The ensemble is generated through an initial perturbation of sea surface height, horizontal and vertical velocities, temperature, salinity and sea-ice concentration generated from a 1-year model run as described by Tang et al. (2020). based on the implementation of Tang et al. (2020). This initial ensemble perturbation is generated by second-order exact sampling (Pham, 2001) from a model trajectory of FESOM2.1. With this method, the leading Empirical Orthogonal Functions (EOFs) of a model trajectory are used to generate an ensemble perturbation that contains the

225 leading patterns of model variability. A time-scale must be chosen for the variability that is represented by the ensemble. Here, we chose variability on a weekly time-scale (Tang et al., 2020).

To maintain ensemble spread, we apply a perturbed atmospheric forcing with an autoregressive perturbation (~~perturb_n~~) (perturb_{e,n}) at every model time step (n) to each ensemble member (e), with:

$$\underline{\text{perturb}_{n+1} = (1 - \text{arc}) * \text{perturb}_n + \text{arc} * s * (N_{\text{ens}} - 1) * \text{rand}}$$

230

$$\underline{\text{perturb}_{e,n+1} = (1 - \text{arc}) * \text{perturb}_{e,n} + \text{arc} * s * \text{rand}_e} \quad (2)$$

where rand is a stochastic element~~that is based on a covariance matrix derived~~, again generated by second-order exact sampling from a 72-days-long ~~period trajectory~~ of atmospheric forcing ~~; the fields that captures patterns of day-to-day atmospheric variability.~~ The autoregression coefficient (arc) ~~is~~ can be used to tune how quickly the perturbation changes and is set to
235 the inverse number of model steps per day~~; and~~, s is a scaling factor for each perturbed atmospheric forcing field. For specific humidity, downwelling longwave radiation and air temperature $s = 10$ is used. The perturbation of winds is set to the smaller value $s = 2$ because the air-sea CO_2 flux in the model is particularly sensitive to perturbations of the wind fields.
~~Because the ensemble spread still~~ Due to the functioning of the Kalman filter (which updates the model error covariance in each analysis step to reflect the new reduced uncertainty), the ensemble spread decays at each analysis step. As the method
240 relies on a sufficiently large ensemble spread, an inflation of the ensemble ~~is applied in each analysis step by applying a forgetting factor ρ (see e.g. Nerger et al., 2005). This inflation uses a time-varying forgetting factor between $\rho = 0.95$ and $\rho = 1$, where~~ covariance is applied (Pham et al., 1998). Thereby, the ensemble covariance matrix is amplified by a factor of $1/\rho$ before entering the updating step. This so-called forgetting factor downweighs that past observations have reduced the model
245 inflation and smaller values mean larger inflation. Here, we use a time-varying forgetting factor between $\rho = 0.95$ and $\rho = 1$. The strongest inflation ($\rho = 0.95$) is applied during the first two weeks of the DA process. During the following 75 days ρ is increased to 0.99~~and from thereon stays between~~. From month 17 onwards, the forgetting factor is set to either 0.99 and/or 1.0 depending on a temperature threshold for the the ensemble standard deviation of ~~the ensemble spread~~.

2.3.3 Assimilated observations

250 ~~We assimilate sea surface temperature (SST), sea surface salinity (SSS) and profiles of temperature (T) and salinity (S). The assimilated SST observations stem from the Operational Sea Surface Temperature and Ice Analysis (OSTIA) data set (CMEMS, 2023; Good et al., 2020; Donlon et al., 2012; Stark et al., 2007). OSTIA provides daily gap-free maps of SST at a horizontal resolution of $0.05^\circ \times 0.05^\circ$, compiled from in-situ and satellite data from infrared and microwave radiometers. The OSTIA observations were averaged to the FESOM2.1 model grid because their spatial resolution is higher than the~~
255 nominal resolution of the model grid. We prescribe an observation error temperature. The ensemble standard deviation of the local instantaneous air-sea CO_2 fluxes that results from the perturbation of physical fields is larger than that of the global

CO₂ flux, with a mean standard deviation of 0.8°C for the DA (Nerger et al., 2020). Observations are excluded in the DA process, if the difference between the model and observation exceeds 2.4°C and at grid points with sea ice in the model, as in Tang et al. (2020) and Mu et al. (2022). This keeps the model stable despite large differences between model and observations at these sites, as water temperature and salinity develop differently under sea ice than under the influence of the atmosphere (Tang et al., 2020).

The assimilated SSS data is taken from the European Space Agency (ESA) Sea Surface Salinity Climate Change Initiative (CCI) (Boutin et al., 2021) v03.21 data set. ESA-CCI contains daily sampled SSS data at a spatial resolution of 50 km and a time resolution of 1 week. The ESA-CCI observations are averaged to the FESOM2.1 model grid. We prescribe a constant observation error 0.32 mmol m⁻² day⁻¹ for monthly means of local fluxes compared to a standard deviation of 0.5 psu (Nerger et al., 2024). Like for the SST data, SSS observations are excluded at locations where sea ice is present in the model.

The assimilated temperature and salinity profiles are taken from the EN.4.2.2 data set (Good et al., 2013). The EN4 dataset contains quality-controlled profiles from various in-situ ocean profiling instruments. To assimilate the profile observations, the model values are computed as the average of the grid points of the triangle enclosing the observation because the number of observations is fewer than model grid points. The observation error 0.0068 mmol m⁻² day⁻¹ (0.01 Pg C yr⁻¹) for the annual global flux in FREE in the year 2020. The largest ensemble standard deviation is set to 0.8°C for temperature and to 0.5 psu for salinity, as in Tang et al. (2020).

2.4 Simulation set-up

The model setup for both simulations closely follows (Gürses et al., 2023). The model mesh is irregular and has a nominal resolution of 1 degree, with enhanced resolution in the equatorial belt and north of 50°N. It has 47 vertical layers with thickness ranging from 5 m at the surface to 250 m in the deep ocean, as described by Scholz et al. (2019). The model time step is 45 minutes. For atmospheric forcing, we use JRA55-do v.1.5.0, reanalysis product tailored for driving ocean-sea ice models (Tsuji no et al., 2018). The atmospheric CO₂ mixing ratio (xCO₂) values were taken from the Global Carbon Budget (Joos and Spahni, 2008; Ballantyne et al., 2012; Friedlingstein et al., 2023). We use model restart fields from Gürses et al. (2023) where the model was spun-up by repeating the year-1961 JRA forcing for 189 years with preindustrial atmospheric CO₂ conditions, followed by a period from 1800 to 1957 with increasing atmospheric CO₂ generated in the Southern Ocean, the North Atlantic and the North Pacific (map in Fig. A1a), which corresponds to regions of high uncertainty in existing CO₂ flux estimates (Pérez et al., 2024; Hauck et al., 2023a; Mayot et al., 2024). However, the modelled standard deviation should not be understood as the true uncertainty of the model, but as a value dependent on tuning (Evensen, 2003). Subsequently, simulations were continued with historical JRA forcing from 1958 to 2009. During the assimilation window (2010-2020), we conduct two ensemble simulations to study the impact of data assimilation (DA) covering the period of the years 2010 to 2020: one without DA (referred to as FREE) and another identical setup applying DA (referred to as ASML).

2.4 Data analysis

~~To assess the model results we focus on the ensemble mean.~~ We present CO₂ flux estimates for the period 2010-2020, that are compared to the 'Regional Carbon Cycle Assessment and Processes 2' (RECCAP2) global air-sea CO₂ flux estimates (DeVries et al., 2023). ~~For the comparison of the global air-sea CO₂ flux in our simulations with the~~ The RECCAP2 CO₂ flux estimates, ~~the pCO₂ products account for oceanic outgassing of river carbon into the atmosphere. To make them comparable with our estimate stemming from a model without river carbon input, we apply a~~ river flux adjustment (Friedlingstein et al., 2023; Regnier et al., 2022) ~~is applied to the~~ to the RECCAP2 pCO₂ products. Thus, we quantify the anthropogenic perturbation of the ocean carbon sink ~~without rivers~~ (as S_{OCEAN} in the Global Carbon Budget Friedlingstein et al., 2023; Hauck et al., 2020), and not the contemporary net air-sea CO₂ flux with outgassing of river carbon (as in the original RECCAP2 pCO₂ products).

To study the effect of DA on the CO₂ flux, we define regions where the effect is pronounced and where different mechanisms are active. ~~In the Southern Ocean, we use,~~ based on the biomes defined by Fay and McKinley (2014). These are, ~~from North to South~~ going polewards from the subtropics in each hemisphere, the Subtropical Seasonally Stratified Biome (STSS), the Subpolar Seasonally Stratified Biome (SPSS) and the Sea-Ice Biome (ICE) ~~(see Fig. 5).~~ Within the STSS, In the Southern Ocean (SO), within the STSS_{SO}, we differentiate between the area where the assimilation leads to a more positive air-sea CO₂ flux (positive: out of the ocean), referred to as STSS_{SO+} and the area where the assimilation leads to a more negative air-sea flux, the STSS-STSS_{SO-} (Fig. 5a and b). In the North Atlantic (NA), we consider four coherent regions within the STSS_{NA} and SPSS_{NA}, defined by the time-mean difference of the air-sea CO₂ fluxes in ASML and FREE (ΔF_{CO_2} , Fig. 7a and b). The Central STSS_{NA-} and Western STSS_{NA+} are located in the central North Atlantic STSS_{NA} biome and are confined by $\Delta F_{CO_2} < -1 \text{ mmol C day}^{-1} \text{ m}^{-2}$ and $\Delta F_{CO_2} > 1 \text{ mmol C day}^{-1} \text{ m}^{-2}$, respectively (see Fig. 7b). The Newfoundland Basin and East Coast SPSS+ and Coastal SPSS_{NA-} are part of the SPSS_{NA}. The former is located east of Newfoundland and south of Greenland, and is confined by $\Delta F_{CO_2} > 3 \text{ mmol C day}^{-1} \text{ m}^{-2}$; and the latter is located off the North American coast and confined by $\Delta F_{CO_2} < -1 \text{ mmol C day}^{-1} \text{ m}^{-2}$. The Central STSS_{NA-} and Western STSS_{NA+} lie on the warm side of the NAC North Atlantic Current (NAC), and the Newfoundland Basin and West Coast SPSS+ and Coastal SPSS_{NA-} lie on the cold side of the NAC, which is evident from the modeled surface velocity field (Fig. A2a).

Within these regions, we identify the time of the year when the DA affects air-sea CO₂ flux and calculate the difference of ASML and FREE for ~~SST, SSS, surface velocities and transports, density, boundary layer depth, surface pCO₂, DIC, alkalinity and surface chlorophyll~~ physical and biogeochemical fields. In order to assess the ~~drivers of~~ dynamic DA effects on surface pCO₂, it is useful to distinguish between different variables that constitute the change in pCO₂. Oceanic pCO₂ varies mainly with temperature, DIC and alkalinity. Thus, we decompose changes in pCO₂ ~~are decomposed after the simulation~~ into their contributions from changes in SST (SST), surface DIC (DIC) ~~and~~ and surface alkalinity (Alk) ~~following the linear~~. For that, we apply the following approximations of Sarmiento and Gruber (2006) and Takahashi et al. (1993):

$$\Delta pCO_{2,DIC} = \frac{pCO_2}{DIC} * \gamma_{DIC} * \Delta DIC \quad (3)$$

320

$$\Delta pCO_{2,Alk} = \frac{pCO_2}{Alk} * \gamma_{Alk} * \Delta Alk \quad (4)$$

$$\Delta p\text{CO}_2, \text{SST} = p\text{CO}_2 * \exp(0.0423 * \Delta \text{SST}) \quad (5)$$

325 ~~with~~ Here, differences between ASML and FREE are denoted by Δ ; else, the average of ASML and FREE is used for the computation. The sensitivities γ_{DIC} and γ_{Alk} describe how $p\text{CO}_2$ varies with changes in one variable while keeping all other variables constant. For the sensitivities, we use an approximation derived from seawater carbonate chemistry following Sarmiento and Gruber (2006):

$$\gamma_{\text{DIC}} = \frac{3 * \text{Alk} * \text{DIC} - 2 * \text{DIC}^2}{(2 * \text{DIC} - \text{Alk})(\text{Alk} - \text{DIC})} \quad (6)$$

$$330 \quad \gamma_{\text{Alk}} = \frac{-\text{Alk}^2}{(2 * \text{DIC} - \text{Alk})(\text{Alk} - \text{DIC})} \quad (7)$$

Values Based on the range of valid values for γ_{DIC} and γ_{Alk} according to the explicit formulation by Egleston et al. (2010), values are excluded above 18 and below -19, respectively. This affects parts of the Southern Ocean SPSS and ICE_{SO} and ICE_{SO} biome (see white areas in Fig. 6b and c). Finally, the effect on the air-sea CO_2 flux relates directly to the $p\text{CO}_2$ -difference at each grid point, as detailed in Orr et al. (2017, equations 6-15):

$$335 \quad \Delta F_{\text{CO}_2} = \alpha \cdot k_w \cdot \Delta p\text{CO}_2 \quad (8)$$

where α is the solubility of CO_2 in seawater and k_w is the gas-transfer velocity.

To evaluate the impact of ~~the DA on the modeled~~ DA on ocean physics, we compare the simulated SST and SSS to the assimilated observations (Section 2.3.1). For temperature and salinity at depth, we use the EN4-OA product (Good et al., 2013, updated to v EN4-OA is an objective analysis ingesting the assimilated EN4 profile data, interpolated to global coverage on 42 depth levels. 340 Furthermore, we compare the sea-ice concentration with remote sensing observations from OSI-SAF 2010-2020 (EUMETSAT, 2022), the mixed-layer depth in the year 2020 with the profile-observation based climatology of de Boyer Montégut et al. (2004, updated version) and the horizontal near-surface velocities 2010-2020 with the drifter-based climatology of Laurindo et al. (2017).

To evaluate the impact of the DA on biogeochemistry, we compare model outputs with ~~independent~~ observational datasets of surface $p\text{CO}_2$, DIC, alkalinity and surface chlorophyll. ~~For each observation type (OBS), we define the improvement as:~~

$$345 \quad \text{improvement}_{\text{OBS}} = |\text{FREE} - \text{OBS}| - |\text{ASML} - \text{OBS}|$$

To evaluate surface $p\text{CO}_2$, we use observations from the Surface Ocean CO_2 Atlas (SOCAT Version 2023, Bakker et al., 2023, 2016), which are provided as a monthly gridded and quality-controlled compilation.

To assess DIC and alkalinity, we compare the modeled surface fields to the GLODAPv2.2023 bottle data (Lauvset et al., 2024b). At depth, we compare the model output to the GLODAPv2 DIC and alkalinity climatology (Lauvset et al., 2016), 350 which is based on observations from the period 1972-2013 and normalized to 2002.

To evaluate global surface chlorophyll, we use observations from ESA-CCI, which is a multi-sensor satellite ocean-color chlorophyll-a dataset with monthly global coverage (Sathyendranath et al., 2021). In addition, for the Southern Ocean, we use the mean of three satellite products (Johnson et al., 2013) that were processed with more suitable algorithms for southern high latitudes. For each observation type (OBS), we define the improvement as:

$$355 \quad \text{improvement}_{\text{OBS}} = |\text{FREE} - \text{OBS}| - |\text{ASML} - \text{OBS}| \quad (9)$$

3 ~~Effect of DA on ocean physics~~ Results

3.1 Effect of DA on ocean physics

Before we investigate the CO₂ flux, we first evaluate the effect of DA on the modeled physics. In particular, we compare the model output of both simulations with the assimilated observations to verify that the assimilation brings them into better agreement with the observations. ~~Additionally, we compare the temperature and salinity with the partly-independent EN4-OA product (Good et al., 2013, updated to version 4.2.2). EN4-OA is an objective analysis ingesting the assimilated EN4 profile data, interpolated to global coverage on 42 depth levels. Furthermore, we compare the sea-ice concentration with remote sensing observations from OSI-SAF (EUMETSAT, 2022).~~

The assimilation improves the agreement with the assimilated SST observations. On a global average, the SST in FREE is 0.14°C colder than the observations, which is estimated to lead to a solubility-driven global air-sea flux difference of -0.06 PgC yr⁻¹ (Eqs. (5) and (8)). FREE exhibits an extensive cold bias of SST in the tropics and subtropics in all ocean basins and a warm bias in the Southern Ocean south of 40°S, visible in Fig. 1a; mean state of SST in Fig. A3a). Additionally, FREE shows regional SST biases in ~~particularly~~ particular near strong currents or in eddy-rich regions, such as the ~~North Atlantic Current (NAC)~~ NAC, Kuroshio, and the Southern Subtropical Front. The assimilation reduces the SST south of 40°S and in the North Pacific, and increases the SST in the tropics and subtropics (see Fig. 1b). The effect of DA is an absolute change by 0.30°C on global average and is particularly strong in the Southern Ocean and in the North Atlantic. Through the assimilation, the model state becomes more similar to the observations globally, which is evident from the positive improvement in Fig. 1c. In total, the global mean absolute difference ~~in SST of SST to the observations~~ is reduced from 0.59°C to 0.32°C. The assimilation-induced change in SST is estimated to drive a direct solubility-driven effect on the global-air sea CO₂ flux of -0.14 PgC yr⁻¹ (Eqs. (5) and (8)). Yet, this global attribution is subject to high uncertainty due to the non-linear dependency of pCO₂ on temperature, and because regionally large effects with opposite signs lead to uncertainty in the global mean.

The assimilation also improves the agreement with the assimilated SSS observations. Additional experiments with and without salinity restoring towards climatology show that the best agreement with the SSS-CCI observations is achieved by simultaneously using assimilation and restoring. A benefit of the additional use of restoring is the global coverage of the SSS climatology. FREE shows a global SSS bias (0.49 psu, Fig. 1d). The assimilation leads to a global surface freshening (Fig. 1e). There are only a few regions where SSS in FREE is fresher than the observations and where the DA consequently increases

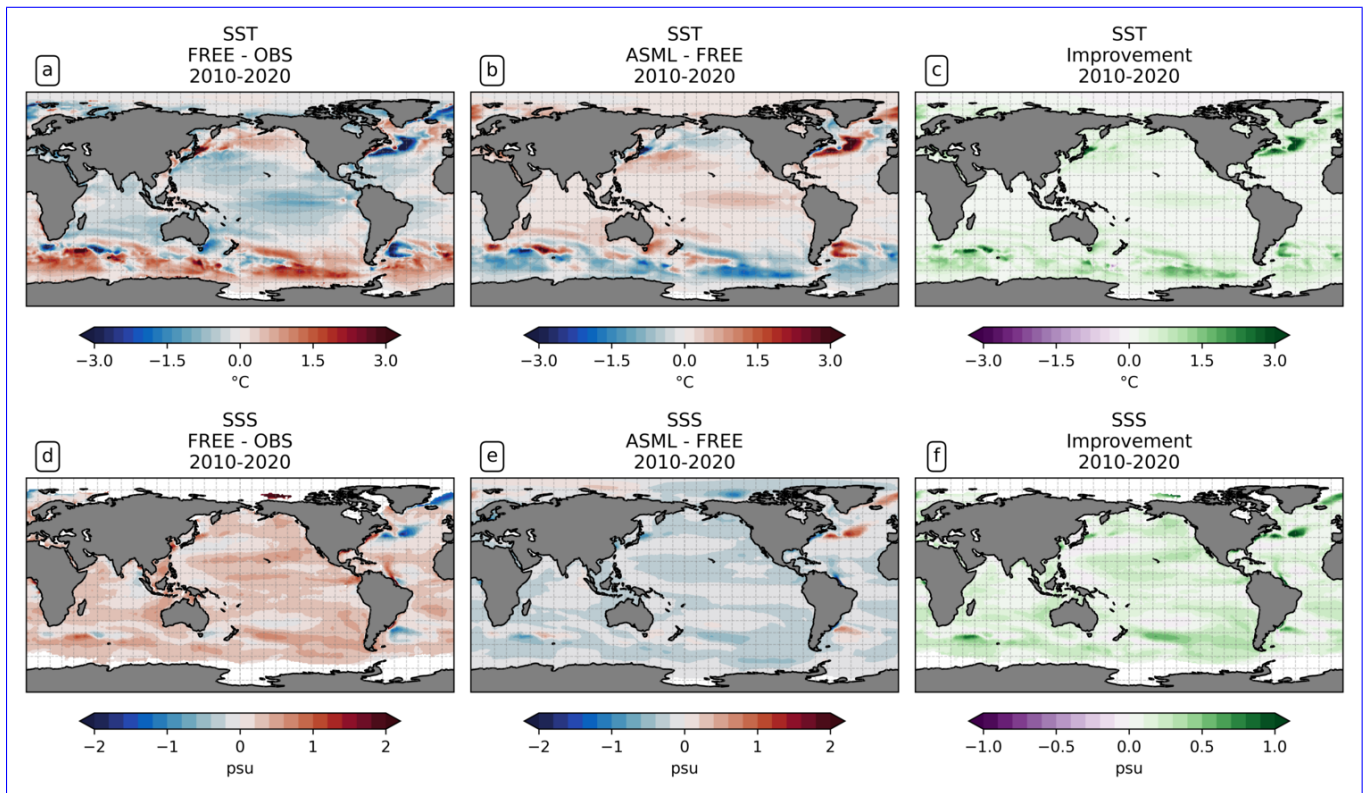


Figure 1. Effect of data assimilation on sea surface temperature (SST) and sea surface salinity (SSS). All panels show the mean over the period 2010-2020. (a) The model-observation difference in SST (FREE - OSTIA). (b) The difference ASML - FREE. (c) The improvement of monthly averaged model SST relative to OSTIA, where positive denotes that the assimilation brings the model closer to observations (Eq. (9)). (e-d - f) The same for SSS, computed with SSS from ESA-CCI.

the salinity. ~~One of these regions lies in~~, as for example in parts of the North Atlantic. The assimilation improves the model-observation agreement in 91% of the observed ocean area, particularly ~~much~~ in the North Atlantic Central STSS_{NA} and in the Southern Ocean STSS_{SO} (Fig. 1f). ~~Albeit negative side-effects~~ Tests with the assimilation of temperature alone show negative side-effects of temperature assimilation on SSS in some locations (not shown). In the final set-up with combined assimilation, negative effects on SSS are found in 9% of the observed area, ~~the global~~. Globally, the mean absolute difference is reduced from 0.32 to 0.17 psu relative to the SSS observations. The direct solubility-driven effect of salinity differences on the global air-sea CO₂ flux is estimated to be negligible.

The assimilation leads to a better agreement with subsurface temperature and salinity data from the ~~non-assimilated~~ EN4-OA product in the upper 1000 m. In the upper 100-200 m of the ocean, the model-observation difference in temperature follows the surface signal (compare Fig. 1a and Fig. 2a), and the difference is reduced by the assimilation (Fig. 2b and c). At intermediate depth (roughly 200-500 m), a subsurface warm bias exists in FREE in the southern hemisphere at mid-latitudes (Fig. 2; mean state in Fig. A4a). This bias affects the South Pacific, South Atlantic and southern Indian Ocean (not shown). ~~It~~ The bias

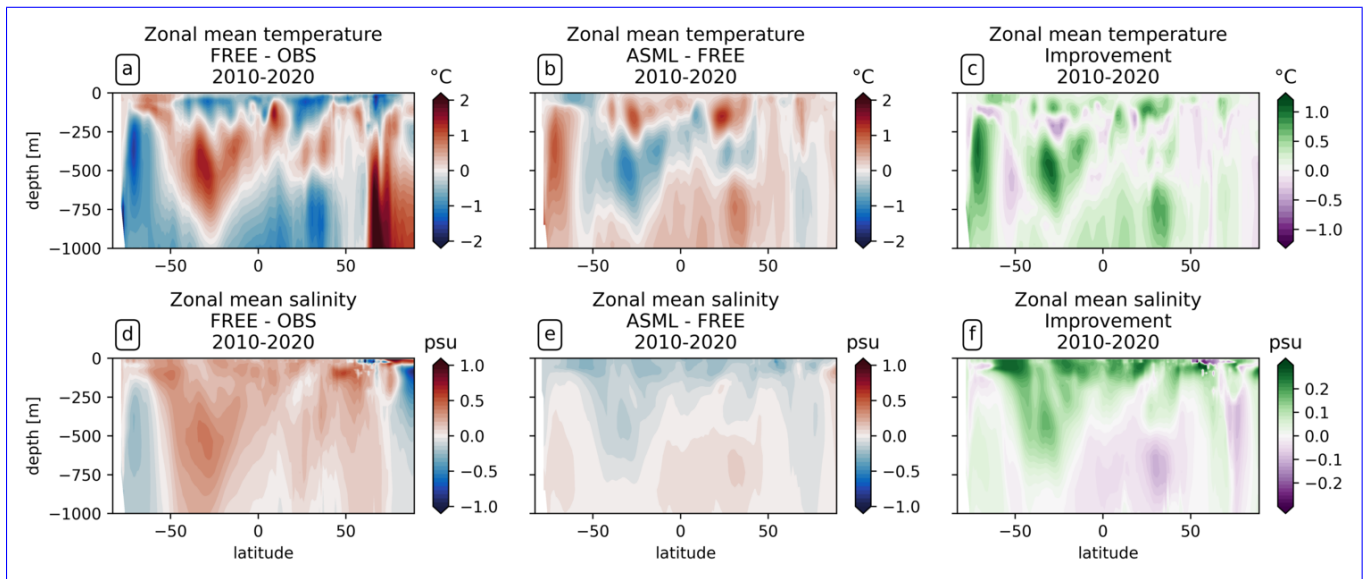


Figure 2. Effect of data assimilation on zonally averaged temperature and salinity in the upper 1000 m. All panels show the mean over the period 2010-2020. (a) The model-observation difference in temperature (FREE - EN4-OA). (b) The difference ASML - FREE. (c) The improvement of monthly averaged temperature relative to EN4-OA. (d - f) The same for salinity.

might be connected to the model's surface warm bias in the formation region of Antarctic intermediate water (Fig. 1a). Further
 395 model-observation differences exist at greater depth than 500 m, where the model's subsurface temperature is colder than the
 observations at almost all latitudes, but warmer than the observations north of 60°N. At most latitudes and depths, the effect
 of the assimilation is to reduce the model observation-differences. ~~This can be seen from the difference of ASML and FREE,~~
~~which has a reversed sign (compare Fig. 2a and Fig. 2b).~~ ~~Thereby, the improvement through DA is mostly positive (Fig. 2~~
~~(Fig. 2c).~~

400 ~~For the salinity, the~~ The model is more saline than the observations from the surface down to a depth of about 1000 m for
 most latitudes (Fig. 2d). This shows that the model-observation difference in this depth range follows the surface signal. The
 exceptions to this are at high latitudes below 200 m, where FREE is fresher than the observations. At all other latitudes, the
 assimilation acts towards a freshening, with the strongest effect near the surface (Fig. 2e). This improves the agreement with
 observations particularly near the surface (Fig. 2d). However, the improvement is smaller at depth and becomes even negative
 405 for some latitudes in greater depth. This might be due to the limited amount of assimilated in situ in situ salinity profiles.

The effect of the assimilation on temperature and salinity is most pronounced in the upper 1000 m and, below that, mostly
 decreases with depth (not shown). After the second year of assimilation, the mean absolute difference between ASML and
 FREE stabilizes in the range 0.35 – 0.36 °C for SST and 0.20 – 0.25 psu for SSS, while the difference of effect of DA on the
 3D fields keeps increasing throughout the years 2010-2020.

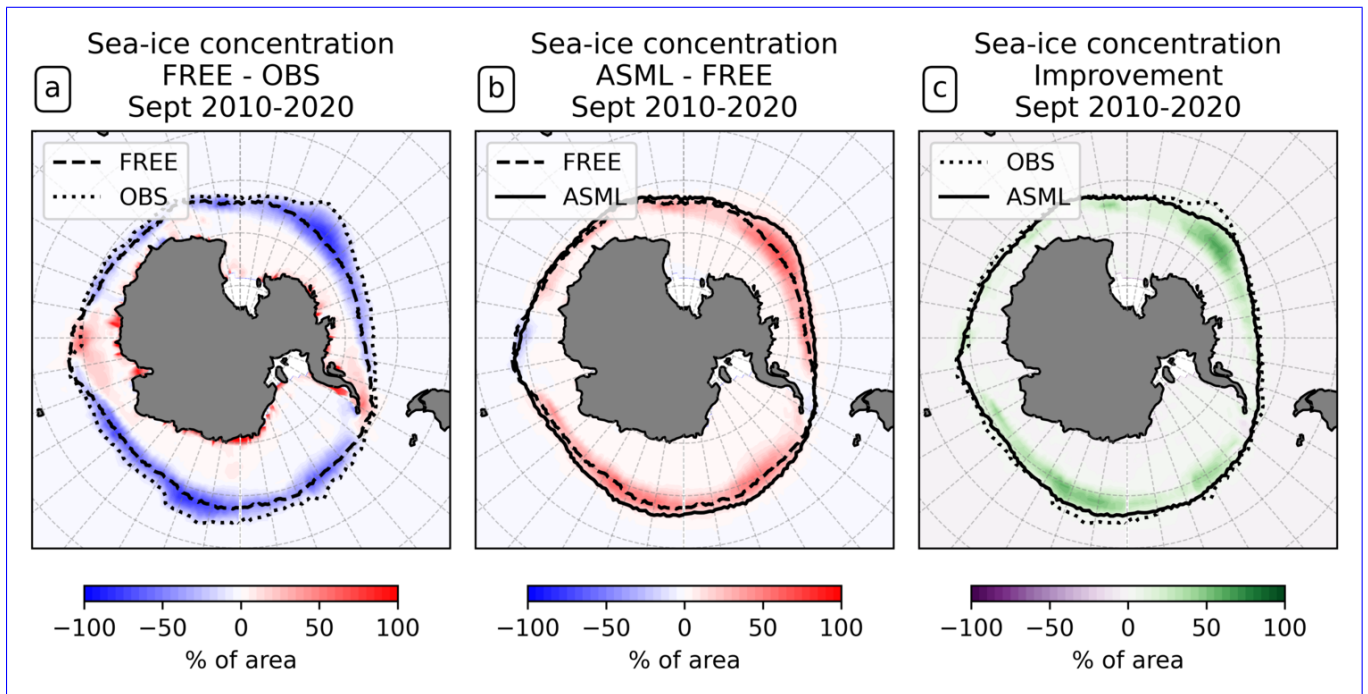


Figure 3. Effect of data assimilation on Antarctic sea-ice concentration in September. All panels show differences in the sea-ice concentration averaged for the month September over the period 2010-2020. The 15%-line for FREE, ASML and OSI-SAF observations is shown as a dashed, continuous or dotted line in panels a or b, respectively. (a) The difference between FREE and OSI-SAF observations. (b) The difference between ASML and FREE. (c) The improvement of September mean sea-ice concentration.

410 Sea ice reacts dynamically to the changed ocean physical state. In the Southern Ocean, FREE is characterized by a lower sea-ice concentration compared to OSI-SAF observations. The ~~maximum extent of sea-ice extent, here defined as the area where~~ the sea-ice in September concentration is more than 15%, reaches a maximum in September. The maximum extent is smaller in FREE than OSI-SAF, which is demonstrated by the ~~15%-lines-line surrounding that area~~ 15%-lines-line surrounding that area for FREE and OSI-SAF (Fig. 3a; mean state of sea-ice concentration in Fig. A5), and by the sea-ice concentration difference for the month September (Fig. 3b).

415 Through DA, a higher Antarctic sea-ice concentration is obtained (see Fig. 3b). This improves the agreement with OSI-SAF (Fig. 3c). During all other seasons, the assimilation leads to a higher sea-ice concentration in the Antarctic, a larger sea-ice extent and a better agreement with OSI-SAF as well (only September is shown). In the Arctic, the differences between FREE, ASML and OSI-SAF are regionally different (not shown).

~~A common issue in data assimilation in GOBMs is erroneous equatorial upwelling, leading to unrealistically high biological~~ productivity in the tropics (Park et al., 2018). In FESOM-REcoM, the ~~The boundary-layer depth and mixed-layer depth are~~ mostly reduced through DA. In particular, deep water formation events characterised by a mixed-layer depth of more than ~~1000 m or 500 m occur less frequently in ASML (not shown). This improves the agreement with the profile-observation~~ based mixed-layer climatology of de Boyer Montégut et al. (2004), reducing the mean absolute difference to the climatology

420

425 from 27 m to 19 m (comparison of mixer-layer depth in Fig. A6). In addition, the absolute difference of near-surface horizontal velocities to the drifter-observation based climatology of Laurindo et al. (2017) is reduced by about 10% through DA (comparison of surface velocities in Fig. A7). The biological productivity near the equator is stable in ASML and FREE, indicating that FESOM-REcoM does not suffer from the erroneous upwelling known from previous DA studies (Park et al., 2018). The meridional overturning, however, shows spurious structures, which may point to hidden assimilation artifacts on vertical velocities (see Appendix Text A1 for further discussion). The. Throughout the assimilation period, spurious, spatially limited and often deep overturning structures emerge, evolve through several months or years, and disappear in the tropical Indian, Pacific and Atlantic basin (not shown). Thereby, the surface overturning cell sometimes breaks apart where it should extend over the equator, exposing the bottom cell to the surface (Fig. A8b). Transport in the North Atlantic at 26.5°N, an indicator for the strength of the Atlantic Meridional Overturning Circulation, is between 8-9 Sv in FREE. In ASML, during the first two years of assimilation, transport at 26.5°N decreases to below 3 Sv and, during the following years, recovers to 7-8 Sv (2016-2020). One possible cause is the effect of data assimilation on the eddy parameterisation (Gent and McWilliams, 1990). The parameterised eddy activity is relevant for the dynamics in the deep ocean, and corrupting it may have a negative impact on the large-scale oceanic circulation, as described in Sidorenko (2004, Chapter 5.5 onwards) for a previous version of the ocean model FESOM.

440 In summary, the ASML temperature and salinity fields at and near the surface in ASML from the surface to several hundred meters below, and mixed-layer depth are in good agreement with the observations. Thus, it can be assumed that the velocities observations, and the agreement of horizontal near-surface velocities with observations is improved. This can be interpreted as an indication that the velocity field in the upper part of the ocean are is also well represented. Therefore Although the spurious effects on deep ocean circulation should be further addressed in future work, we are confident that the DA provides an improved physical state in the upper ocean, which serves as an improved basis to estimate the air-sea CO₂ flux, although the spurious effects on deep ocean circulation should be further addressed in future work.

4 Results

3.1 Global Effect of DA on global CO₂ flux

The ocean absorbs $2.78 \text{ Pg C dec}^{-1}$ $2.78 \text{ Pg C yr}^{-1}$ in ASML and $2.83 \text{ Pg C dec}^{-1}$ $2.83 \text{ Pg C yr}^{-1}$ in FREE during 2010-2020 (Fig. 4b), thus the assimilation decreases the global mean oceanic CO₂ uptake by $0.05 \text{ Pg C dec}^{-1}$ $0.05 \text{ Pg C yr}^{-1}$. The temporal evolution of the annual global CO₂ flux is similar in ASML and FREE (Fig. 4a). The first assimilation year, 2010, stands out because it is one of the very few years during which the assimilation increases the oceanic CO₂ uptake. This slightly reduces the trend in CO₂ uptake 2010-2020 ($-0.40 \pm 0.09 \text{ Pg C dec}^{-1}$ versus $-0.38 \pm 0.11 \text{ Pg C dec}^{-1}$ from $-0.40 \pm 0.09 \text{ Pg C yr}^{-1} \text{ dec}^{-1}$ in FREE to $-0.38 \pm 0.11 \text{ Pg C yr}^{-1} \text{ dec}^{-1}$ in ASML (negative: into the ocean). The trend, thereby, remains within its confidence interval. Furthermore, the assimilation reduces the interannual variability of the global mean oceanic uptake slightly, demonstrated by a standard deviation of detrended annual means of $0.11 \text{ Pg C dec}^{-1}$ $0.11 \text{ Pg C yr}^{-1}$ in FREE and $0.08 \text{ Pg C dec}^{-1}$ $0.08 \text{ Pg C yr}^{-1}$ in ASML (not significantly different according to F-test). Through DA, the

ensemble standard deviation of the global CO₂ flux is reduced from $1.0 \times 10^{-2} \text{Pg C yr}^{-1}$ in FREE to $0.7 \times 10^{-2} \text{Pg C yr}^{-1}$ in ASML in the year 2020.

The strongest time-mean air-sea CO₂ flux (~~negative: into the ocean~~) is found at mid and high latitudes (Fig. 4c). The large-
460 scale pattern of the CO₂ flux is generally very similar in FREE and in ASML (FREE not shown). ~~However, the effect of the assimilation on the CO₂ flux varies from region to region (Fig. 4d).~~ The largest local changes through DA, both towards stronger or weaker CO₂ fluxes, occur in the North Atlantic in the area of the NAC and in the coastal North Pacific (Fig. 4d). The most prominent large-scale effect though, is in the Southern Ocean (Fig. 4e and f). South of 50°S, the area-integrated CO₂ uptake increases by ~~$0.18 \text{Pg C dec}^{-1}$~~ 0.18Pg C yr^{-1} through the assimilation (Fig. 4e and f). In contrast, the uptake decreases
465 by ~~$0.07 \text{Pg C dec}^{-1}$~~ 0.07Pg C yr^{-1} between 40-50°S. With the exception of the Southern Ocean, CO₂ uptake decreases in all world oceans by a small amount (Fig. 4d and e).

3.2 Regional Effect of DA on regional CO₂ fluxes and their drivers

~~The impact of the DA on the CO₂ flux is particularly large-~~

3.2.1 Southern Ocean

470 In the Southern Ocean, the ocean takes up CO₂ in the annual average (Fig. 5a), with regionally heterogeneous effects of DA (Fig. 5b). While the effect of DA on surface pCO₂ and the air-sea CO₂ flux can almost entirely be explained by the combined variation of DIC and alkalinity at most latitudes north of 40°S, the thermal effect also needs to be considered in the Southern Ocean, where we now inspect individual regions. (global zonal mean pCO₂-effects in Fig. A9a). In the following, we examine how the assimilation influences the air-sea CO₂ flux across individual regions in the Southern Ocean.

475 STSS_{SO} In the northernmost biome of the Southern Ocean, the subtropical seasonally stratified biome (STSS; ~~outlined in Fig. 5a_{SO}~~), the mean oceanic CO₂ uptake is comparably high (Fig. 5a). ~~Here, the The~~ uptake is largest in austral winter and spring (June to November, Fig. 5c and d). ~~In the more northern The~~ part of the STSS, ~~which we call the STSS+, the CO₂ uptake is reduced through the assimilation, demonstrated~~ SO characterized by a positive CO₂ flux difference between ASML and FREE in this area (Fig. 5b). ~~The reduction is greatest in winter and spring, which is shown through a positive flux difference between ASML and FREE from July to October (Fig. 5g). In contrast, in the more southern part of the STSS, (positive difference: reduced uptake through assimilation), which we call the STSS-, the assimilation increases the oceanic CO₂ uptake (Fig. 5)~~ STSS_{SO+}, roughly forms an outer northerly ring around the STSS_{SO} biome (hatched area in Fig. 5a and b). The increase reduction of CO₂ uptake through DA is largest in summer and autumn (November to April, Fig. 5h in the STSS_{SO+} is greatest in winter and spring from July to October (Fig. 5g).

485 ~~Further south, in the subpolar seasonally stratified biome (SPSS), the ocean absorbs CO₂ all~~ The increase in pCO₂ in the STSS_{SO+} is partly driven by lowered alkalinity and partly by increased surface DIC (Fig. 6b and c). These, as well as the colder SST and fresher SSS in the STSS_{SO+} (Fig. 1b and e) are indications for a year-round (Fig. 5a). The oceanic uptake is increased through the assimilation, shown by a negative difference of ASML and FREE in Fig. 5b. The largest difference between ASML and FREE is seen in spring from September to October (Fig. 5i). Due to the seasonal effect of DA, stronger

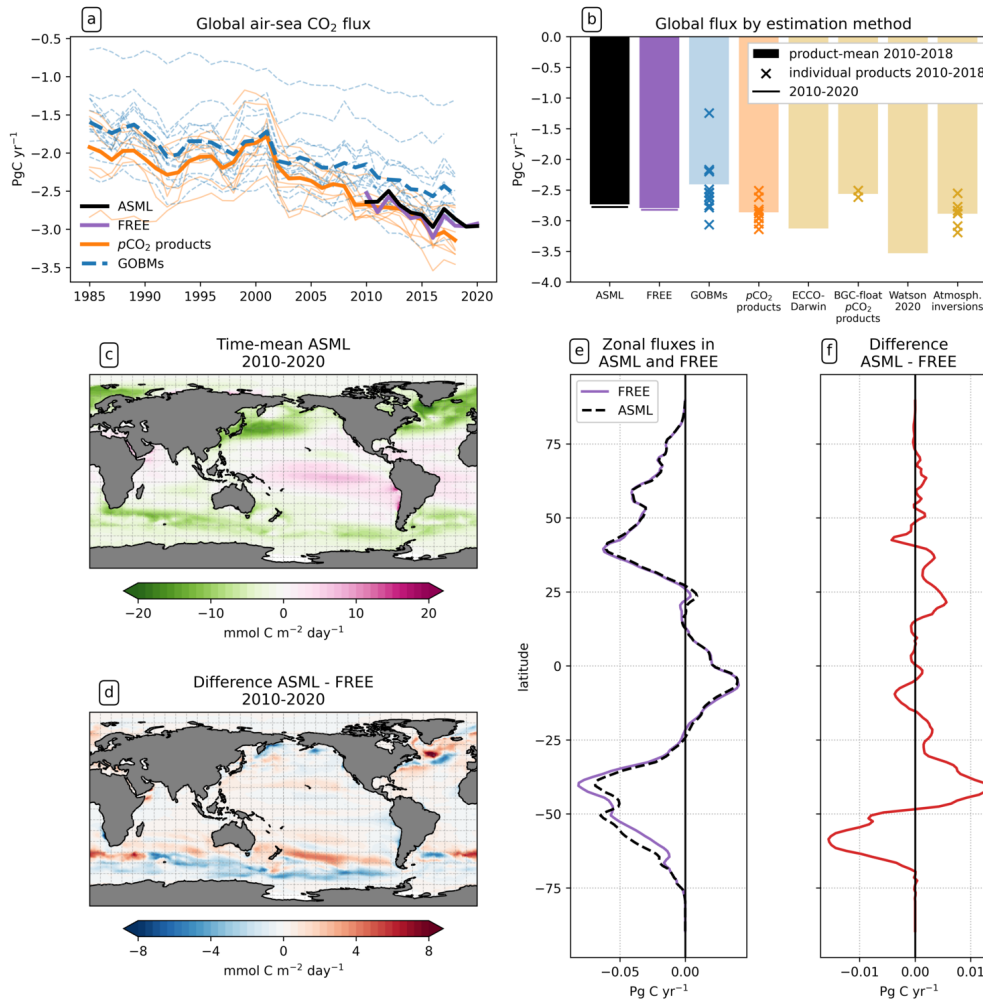


Figure 4. Effect of data assimilation on the air-sea CO₂ flux (negative: into the ocean). (a) Annual time-series of global flux in Pg C dec^{-1} Pg C yr^{-1} in FESOM-RECoM-PDAF with ASML (black) and FREE (violet); and RECCAP-RECCAP2 estimates (DeVries et al., 2023) with pCO₂-products (orange) and GOBMs (blue) and their respective ensemble-means (bold lines). Here, the river flux adjustment ($-0.65 \text{Pg C dec}^{-1}$ $-0.65 \text{Pg C yr}^{-1}$) was applied to the pCO₂ products. (b) Time-mean global flux 2010-2018 in ASML (black), FREE (violet); and RECCAP estimates grouped by method (DeVries et al., 2023). Crosses represent individual estimates (e.g. individual GOBMs) and bars represent the ensemble-method mean (e.g. mean of twelve GOBMs). Here, the river flux term was applied to all estimates except the models following the Global Carbon Budget methodology (Friedlingstein et al., 2023). For FESOM-RECoM-PDAF, additionally the time-mean 2010-2020 is shown (horizontal lines). (c) Spatial distribution of CO₂ flux averaged over the period 2010-2020 in ASML. (d) Spatial distribution of CO₂ flux difference between ASML and FREE averaged over the period 2010-2020 (e) Zonal averages of CO₂ flux 2010-2020 in ASML and FREE, and their difference in (f).

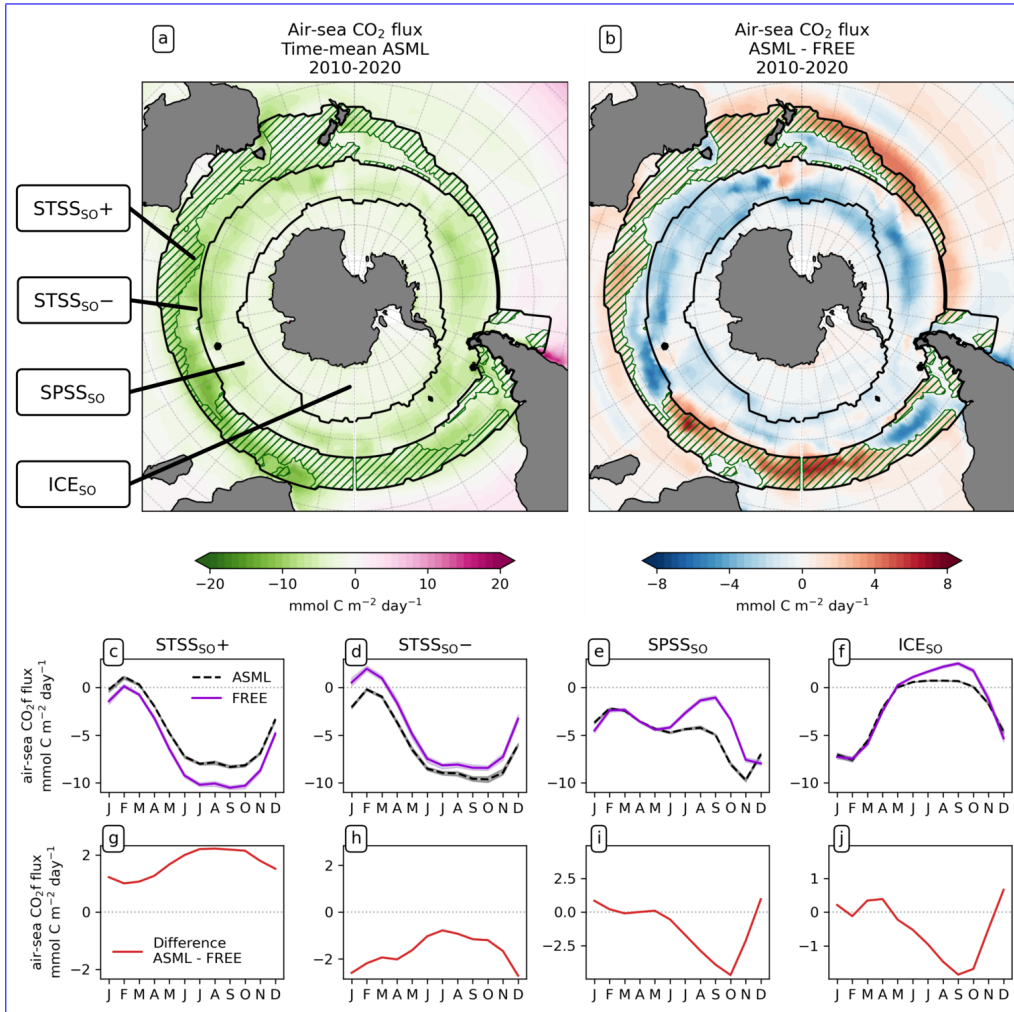


Figure 5. Effect of data assimilation on Southern Ocean CO₂ flux and its seasonality averaged over the period 2010-2020. Negative numbers indicate a flux into the ocean. Additionally, lines in a and b denote the regions, and the green hatching denotes the STSS_{S0+}. (a) Map of mean CO₂ flux in ASML. (b) Map of difference between CO₂ flux in ASML and FREE. (c - f) Seasonal cycle of air-sea CO₂ flux by region. Shading indicates the range of ensemble members in the year 2020. (g - j) Seasonal difference in air-sea CO₂ flux between ASML and FREE by region. Note the different scales.

490 influence of subantarctic waters. This is evident from typical water properties in the subantarctic and subtropical Southern Ocean. In the seasonal cycle of the CO₂ flux in the SPSS is altered. In ASML, the CO₂ uptake is weakest in February, gets stronger in autumn (MAM), stalls growing in winter (JJA) and resumes to get stronger in spring (SON), reaching peak uptake in November (Fig. 5e). In FREE, the CO₂ uptake is weakening in winter, is weakest in September and gets stronger afterwards, reaching peak uptake in December.

495 In the seasonally ice-covered biome (ICE) surrounding the Antarctic continent, the time-mean CO₂ flux is smaller than in the other biomes (Fig. 5a). In this region, the ocean absorbs CO₂ during summer and there is a smaller outgassing during winter (Fig. 5f), as the region is mostly ice-covered in winter (see sea-ice concentration in September in Fig. 3subantarctic, surface DIC is higher, surface alkalinity is lower, temperature is colder and salinity is lower (maps of mean SST, SSS, DIC and alkalinity in Fig. A10). In the northern part of the ICE biome, close to the SPSS, the effect of the assimilation is similar
500 to the effect within the SPSS itself (Fig. 5b). Here, the assimilation acts to increase ocean CO₂ uptake or to weaken CO₂ outgassing during winter and spring (Fig. 5i and j). Thereby, interestingly, the assimilation hinders outgassing of CO₂ from May to November in ASML in the ICE biome (Fig. 5f; comparison of winter outgassing with other estimates in Fig. A14). In the southern part of the ICE biome, near the Antarctic continent, the effect of the fragmented area of the STSS_{SO+}, different factors contribute to regional changes of the surface DIC and alkalinity budget in ASML (sources minus sinks of DIC and
505 alkalinity in Fig. A11). Depending on location, an increased upward transport of DIC through mixing, an increase of DIC through a reduced biological sink of DIC in spring, or a decrease of alkalinity through changes in horizontal and vertical advection dominates. The seasonality of the effect of DA on the CO₂ flux is small.

Effect of data assimilation on Southern Ocean CO₂ flux and its seasonality averaged over the period 2010-2020. Negative numbers indicate a flux into the ocean. (a) Map of mean CO₂ flux in ASML. (b) Map of difference between CO₂ flux in ASML and FREE. (c-f) Seasonal cycle of air-sea CO₂ flux by region. (g-j) Seasonal difference in air-sea CO₂ flux between ASML and FREE by region. Note the different scales.

510

In the North Atlantic, the assimilation has noticeable effects on the CO₂ flux in the area of the NAC. In this region, the ocean absorbs CO₂ in the annual average (Fig. 7a). However, the ocean releases some CO₂ during summer, while the sea surface warms (Fig. 7e-f). In the Central STSS, the effect of the DA is to prevent outgassing during summer (Fig. 7air-sea CO₂ flux in
515 the STSS_{SO+} (Fig. 5c and g). In the Western STSS and in the Newfoundland Basin, the ocean CO₂ uptake is decreased during winter (Fig. 7d, e, h and j). In the East Coast SPSS, the ocean CO₂ uptake is increased (Fig. 7f and j). The regionally different dynamics of is determined by seasonal temperature differences between ASML and FREE (Fig. 6d and f). During summer, SST is slightly reduced (Fig. 6f), which lowers pCO₂ (Fig. 6a). This counteracts the effects of the assimilation that drive these differences in the air-sea CO₂ flux in the North Atlantic and Southern Ocean, will be investigated next.

520 Effect of data assimilation on North Atlantic CO₂ flux and its seasonality averaged over the period 2010-2020. Negative numbers indicate a flux into the ocean. (a) Map of mean CO₂ flux in ASML. (b) Map of difference between CO₂ flux in ASML and FREE. (c-f) Seasonal cycle of air-sea CO₂ flux by region. (g-j) Seasonal difference in air-sea CO₂ flux between ASML and FREE by region. Note different scales.

525 In the Southern Ocean, the reduced CO_2 uptake and increased pCO_2 in the STSS+ region is driven by increased surface DIC and lowered alkalinity (Fig. 6b and c, hatched area). These, as well as the colder SST and fresher SSS in the $\text{STSS}_{\text{SO}-}$ and thus dampens the overall DA-effect on the air-sea CO_2 flux during summer.

530 The part of the STSS+ region (Fig. 1b and e) are indications for a year-round stronger influence of subantarctic waters. This is evident as in the subantarctic, surface DIC is higher and surface alkalinity is lower than in the subtropical Southern Ocean (Fig. A10e and d), and, furthermore, the subantarctic is characterized by cold temperatures and low salinity (Fig. A10- SO characterized by a negative CO_2 flux difference between ASML and FREE, which we call the $\text{STSS}_{\text{SO}-}$, is a fragmented region and roughly consists of segments of an inner southerly ring (non-hatched area in Fig. 5a and b). In addition, reduced net primary production (NPP) in spring contributes to higher DIC in the STSS+ region in ASML (not shown). In contrast, the increased CO_2 uptake and reduced pCO_2 in the STSS- Here, the increase of CO_2 uptake through DA is largest in summer and autumn (November to April, Fig. 5h). The reduction of pCO_2 is driven by increased alkalinity, and partly also by lower surface DIC and by increased alkalinity (Fig. 6b and c, non-hatched area). These, together with higher SST in ASML than FREE in the $\text{STSS}-\text{STSS}_{\text{SO}-}$ regions (Fig. 1b), indicate a higher presence of subtropical waters (see characteristics of subtropical waters in Fig. A10). Moreover, higher NPP contributes to Where there is lower DIC in the $\text{STSS}-\text{region}-\text{STSS}_{\text{SO}-}$ in ASML (not shown). The seasonality of the effect of DA on the air-sea CO_2 flux (Fig. 5c-d,g-h) is determined by seasonal temperature differences between ASML and FREE (Fig. 6d-g). In the STSS+ region, SST is slightly reduced during summer (Fig. 6f). 540 This lowers pCO_2 in the STSS+ region (Fig. 6a), counteracts the effects of DIC and alkalinity on pCO_2 and thus dampens the overall effect on the air-sea CO_2 flux during summer. In contrast, in the STSS- region, the Fig. 6b), this can mostly be explained by an increased biological sink of DIC, with the addition of sharply defined local changes in horizontal advection of DIC and alkalinity (Fig. A11). Additionally, seasonal temperature effects occur. During winter, SST is higher in ASML than FREE during winter in FREE (Fig. 6e and g). This increases pCO_2 in the $\text{STSS}-\text{region}-\text{STSS}_{\text{SO}-}$ (Fig. 6a), counteracting the 545 effects of lower DIC and higher alkalinity on pCO_2 and dampening the overall effect-DA-effect during winter. In summary, the

The contrasting effects in the STSS are probably generated by a horizontal redistribution- SO indicate a horizontal shift of water masses within the STSS_{SO} biome. In the center of the STSS_{SO} , the Subantarctic Front is located, which is associated with the Antarctic Circumpolar Current (ACC) and characterized by a strong gradient in SST, SSS and various other tracers 550 (Chapman et al., 2020). Because SST and SSS are directly influenced and improved by the assimilation, the position of this front is also expected to change as a result of the assimilation, leading to a horizontal relocation of waters separated by the front. In addition, differences in the horizontal transport With the relocation of the front, dynamic shifts in regional characteristics occur, such as the amount of DIC and alkalinity by the ACC (transport not shown), and differences in the velocities transported vertically through mixing, and biological sources and sinks of DIC and alkalinity.

555 SPSS_{SO} Further south, in the subpolar seasonally stratified biome (SPSS_{SO}), the ocean absorbs CO_2 all year-round (Fig. 5 a). The oceanic uptake is increased through the assimilation, shown by a negative difference of ASML and FREE in Fig. 5 b. The largest difference between ASML and FREE (Fig. A18), indicate a horizontal redistribution with zonal and meridional components- is seen in spring from September to October (Fig. 5i). Due to the seasonally varying effect of DA, the seasonal

560 cycle of the CO₂ flux in the SPSS_{SQ} is altered. In ASML, the CO₂ uptake is weakest in February, gets stronger in autumn (MAM), stagnates in winter (JJA) and resumes to grow in spring (SON), reaching peak uptake in November (Fig. 5e). In FREE, the CO₂ uptake weakens in winter, is weakest in September and gets stronger afterwards, reaching peak uptake in December.

In the SPSS_{SQ}, the increased CO₂ uptake and lower surface pCO₂ during winter and spring is driven by a combination of ~~lower DIC and colder temperatures~~ colder temperatures and lower DIC (Fig. 6a and b), which ~~outweigh~~ outweighs the opposite effect of a decrease in alkalinity on pCO₂ (Fig. 6c, relative importance of thermal effect in Fig. A12a). Surface DIC is generally high due to upwelling-upward transport of carbon-rich deep water (Hauck et al., 2023a) (e.g. Hauck et al., 2023a). The reason for lower surface DIC in ASML is likely that the upward transport ~~of DIC is reduced through mixing is reduced~~ (Fig. A11) through a more stable stratification, which is ~~shown by~~ also evident from a reduced density in the upper 300 m and an increased density below that (Fig. 6h). Thereby, the densities in the SPSS_{SQ} agree better with densities calculated from EN4-OA. ~~The more stable stratification reduces the depth of the boundary layer~~ Boundary layer and mixed layer in winter and spring (~~not shown~~ are shallower and thereby in better agreement with the observation-based climatology (Fig. A6)). Vertical mixing within the boundary layer affects the vertical ~~profile of DIC~~ profiles of DIC and alkalinity, towards lower DIC in ASML above 100 m and higher DIC below (Fig. 6i). The vertical profile of DIC in ASML is closer to GLODAP DIC observations, albeit some differences to GLODAP still exist. Besides the fact that the differences in stratification and ~~boundary layer~~ boundary-layer depth affect the vertical DIC profile, they also imply less available surface nutrients in ASML. Probably due to ~~that, in the SPSS,~~ a combination of lower nutrient availability and colder surface temperature, ASML features lower NPP, lower chlorophyll concentrations and a lower phytoplankton biomass in the SPSS_{SQ} (not shown). Thereby, the modeled biogeochemical cycle adjusts to the lower transport of nutrients to the surface by transferring less organic material to depth, ultimately acting to compensate about 60% of the difference in physical transport of DIC (Fig. A13a) and adding to the reduction in surface alkalinity (Fig. A13b). Within the SPSS_{SQ} (roughly south of 50°S), differences between FREE and ASML in terms of the temperature effect on pCO₂, vertical transport of DIC and alkalinity and biological sources and sinks are larger than at any other latitude (Fig. A13).

~~In the Northern ICE~~ ICE_{SQ} In the seasonally ice-covered biome (ICE_{SQ}) surrounding the Antarctic continent, the time-mean CO₂ flux is smaller than in other biomes (Fig. 5a). In this region, the ocean absorbs CO₂ during summer and there is a smaller outgassing during winter (Fig. 5f), as the region is mostly ice-covered in winter (see sea-ice concentration in September in Fig. 3). In the northern part of the ICE ~~biome near the SPSS,~~ the SQ biome, close to the SPSS_{SQ}, the effect of the assimilation is similar to the effect within the SPSS_{SQ} itself (Fig. 5b). Here, the assimilation acts to increase ocean CO₂ uptake or to weaken CO₂ outgassing during winter and spring (Fig. 5i and j). Thereby, interestingly, the assimilation hinders outgassing of CO₂ from May to November in ASML in the ICE_{SQ} biome (Fig. 5f; comparison of winter outgassing with other estimates in Fig. A14). The reduced outgassing and decreased pCO₂ during winter and spring is driven by similar processes as within the SPSS_{SQ}. Again, lower surface DIC and colder temperatures (Fig. 6a and b) outweigh the opposite effect of a decrease in alkalinity on pCO₂ (Fig. 6c). As in the SPSS_{SQ}, the reason for the decrease in pCO₂, is ~~, firstly, a more stable stratification through surface freshening, which reduces DIC above~~ reduced surface DIC and increased DIC below 100 m ~~depth and increases DIC below~~

(not shown). Secondly as a result of less upward transport of DIC through mixing (Fig. A11) in a more stable stratification due to surface freshening (Fig. 1e). In addition, as the surface temperature is lower in ASML (Fig. 1b), the winter sea-ice concentration is higher (Fig. 3b), which prevents winter outgassing of CO₂. In the southern part of the ICE_{SO} biome, near the Antarctic continent, the effect of the DA on the CO₂ flux is small.

In summary, in the Southern Ocean, the main effects of the DA on the CO₂ flux are, firstly, an increase of the uptake in the SPSS caused by SO caused by surface cooling and by a more stable stratification and thus less upward transport of naturally carbon-rich water through mixing and secondly, an overall decrease of, and secondly an overall lower CO₂ uptake in the STSS_{SO} as a consequence from a horizontal redistribution of water masses within the STSS spatial redistribution of fluxes near the Subantarctic Front.

3.2.2 North Atlantic

In the North Atlantic, the effects of the DA on the CO₂ flux are locally large, but there are differences to the Southern Ocean. assimilation has noticeable effects on the CO₂ flux in the area of the North Atlantic Current, where the ocean absorbs CO₂ in the annual average (Fig. 7a). During summer however, the ocean releases CO₂ while the sea surface warms (Fig. 7c-f). In the Central STSS_{NA-}, the effect of the DA is to prevent outgassing during summer (Fig. 7c and g). In the Western STSS_{NA+} and in the Newfoundland Basin+, the ocean CO₂ uptake is decreased during winter (Fig. 7d, e, h and j). The regionally different dynamics of the effects of the assimilation that drive these differences in the air-sea CO₂ flux in the North Atlantic are investigated next.

Central STSS_{NA-} In the Central STSS_{NA-}, the effect of the DA is towards increased uptake of CO₂ during boreal summer and autumn in ASML overall towards a more negative flux of CO₂ from May to November (Fig. 7g). This prevents summer outgassing, which occurs from June to October in FREE. Thus, spring and autumn CO₂ uptake are increased and summer outgassing is prevented in ASML (Fig. 7c). The reason for the higher uptake and decreased surface pCO₂ is higher alkalinity in ASML (Fig. 8bc). In this region, the alkalinity effect, which reduces pCO₂, outweighs the opposing effects of DIC and SST on pCO₂ (Fig. 8a and eb). A higher alkalinity could point to the presence of waters of subtropical origin (Fig. A15d), transported northward with the NAC (Völker et al., 2002). Other fingerprints of waters advected transported by the NAC are a warm SST particularly in winter, a higher salinity and higher DIC than that of North Atlantic subpolar waters (Fig. A15a-c, Völker et al., 2002) (maps of mean SST, SSS, DIC, alkalinity in Fig. A15; Völker et al., 2002). The assimilation causes a change in these properties, towards a higher SST, higher salinity and higher DIC in the Central STSS (Fig. A15)_{NA-}. Simultaneously, ASML represents higher NPP, biological carbon export at 200 a deeper boundary layer in this region (Fig. 8 d). While changes in the North Atlantic mixed-layer depth overall result in a spatial pattern in ASML that more closely aligns with the pattern in the observation-based mixed-layer climatology, the modelled mixed layer in the simulations is still overall deeper than in the climatology, leading to less agreement in the Central STSS_{NA-} (Fig. A6). Likely facilitated by higher SST and more available nutrients through deeper mixing in winter and spring, ASML features a higher biological sink of DIC above 190 m (Fig. A16d), more biological carbon export through sinking of detritus at 190 m, surface chlorophyll and more column integrated phytoplankton biomass and surface chlorophyll in spring, which is shown illustrated by the example of

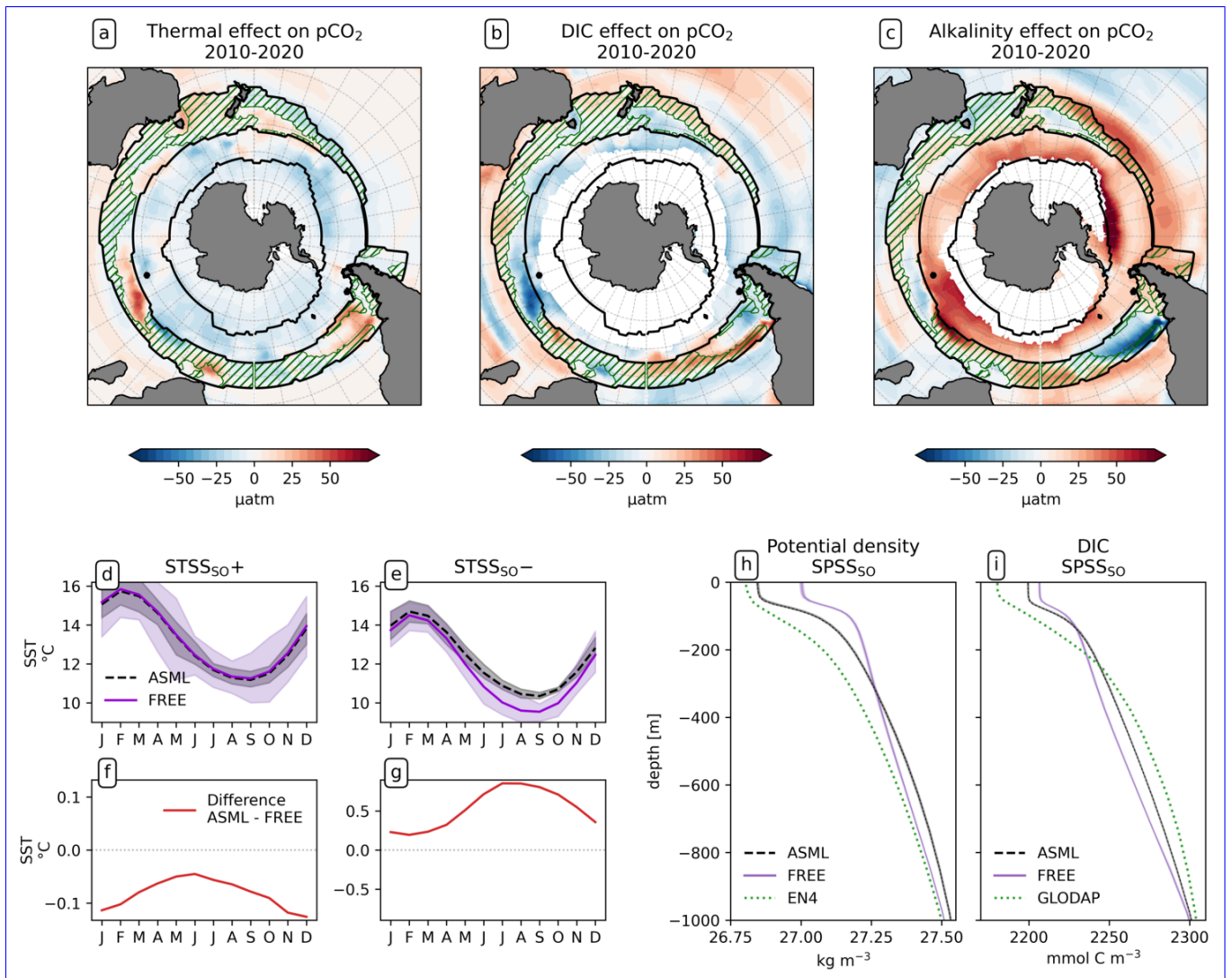


Figure 6. Drivers of the effects of data assimilation on air-sea CO_2 fluxes in the Southern Ocean. Panels a, b and c show the effects of SST, DIC and alkalinity differences between the ASML and FREE simulations on surface pCO_2 , where positive denotes an increase in pCO_2 . Hatching inside the STSS_{SO} indicates where net pCO_2 is increased through the assimilation ($\text{STSS}_{\text{SO}+}$). (d and e) Seasonal cycle of SST averaged over the regions $\text{STSS}_{\text{SO}+}$ and $\text{STSS}_{\text{SO}-}$ for the ASML and the FREE $\text{STSS}_{\text{SO}-}$, and (f and g) the difference between ASML and FREE for each region. (h) Potential density profiles for the SPSS in the Southern Ocean SO , with FREE (violet line) and ASML (dashed black line) based on daily T and S, and with EN4-OA (dotted green line) based on monthly T and S. (i) DIC profiles for the SPSS in the Southern Ocean SO , showing FREE (violet line), ASML (dashed black line) from 2010-2020 and climatological DIC from GLODAP. Shading in d, e, h and i indicates the range of ensemble members in the year 2020.

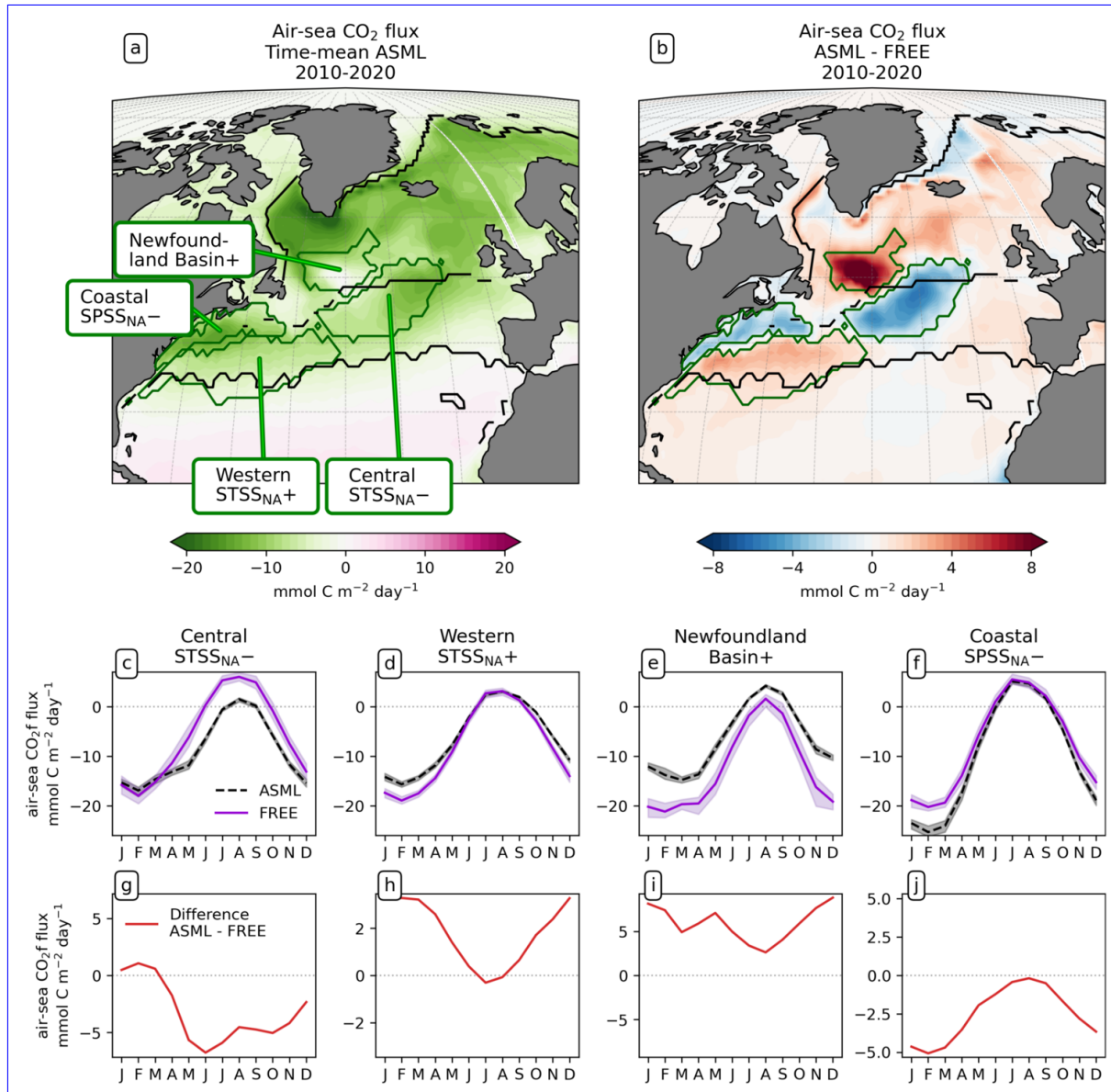


Figure 7. Effect of data assimilation on North Atlantic CO₂ flux and its seasonality averaged over the period 2010-2020. Negative numbers indicate a flux into the ocean. (a) Map of mean CO₂ flux in ASML. (b) Map of difference between CO₂ flux in ASML and FREE. (c - f) Seasonal cycle of air-sea CO₂ flux by region. Shading indicates the range of ensemble members in the year 2020. (g - j) Seasonal difference in air-sea CO₂ flux between ASML and FREE by region. Note different scales.

surface chlorophyll difference between ASML and FREE in Fig. 8e. ~~This is facilitated by more available nutrients through winter mixing in the surface boundary layer, which is deeper in ASML (Fig. 8d).~~ In combination, the higher ~~biological export of carbon alkalinity associated with NAC transport~~ and the higher ~~alkalinity in ASML biological sink of DIC~~ result in lowered surface $p\text{CO}_2$ and higher oceanic uptake.

Western STSS_{NA+} In the Western STSS_{NA+}, the DA reduces the CO_2 uptake and increases $p\text{CO}_2$ mainly during winter, as a direct effect of increased SST (Fig. 8a). ~~In this region, the thermal effect of DA, which increases $p\text{CO}_2$, The direct thermal effect~~ is dominant over the combined effect of DIC and alkalinity ~~(relative importance of thermal effect in Fig. A12b)~~. The latter have effects comparable in magnitude to SST, but mostly cancel each other out (Fig. 8b-c). The effect of DA on surface properties (SST, SSS, DIC and alkalinity) in the Western STSS_{NA+} is similar to the effect in the Central STSS_{NA-}, which indicates a higher influence of subtropical waters in both regions.

Newfoundland Basin+ In the Newfoundland Basin+, the dominant effect of DA is a reduction of the CO_2 uptake and an increase of $p\text{CO}_2$ mainly during winter, as a direct effect of increased SST (Fig. 8a). In addition, ASML also features ~~shallower winter mixing inside the boundary layer (Fig. 8d) and~~ a more stable stratification due to lower density at the surface than FREE (Fig. 8f). ~~Consequently, DIC and alkalinity in the upper 100 m are slightly reduced. Nevertheless, some differences to GLODAP-DIC observations remain (DIC in, which mostly affects DIC at 50-400 m depth through reduced subduction of DIC (Fig. 8g). However, the thermal effect of DA, which increases $p\text{CO}_2$, is dominant over the combined effect of DIC and alkalinity on $p\text{CO}_2$ (Fig. 8b and e), as the latter cancel each other out. Furthermore, surface nutrients, NPP, export production, biomass and surface chlorophyll are reduced (surface chlorophyll in Fig. 8e) Furthermore, ASML represents less surface chlorophyll in the Newfoundland Basin+ (Fig. 8e) as a result of a redistribution of biomass from the surface to 50-400 m depth due to spring mixing (not shown). The downward mixing of biomass results in an increase of the biological sink of DIC above 50 m likely due to more primary production near the surface, probably due to shallower mixing. In the Western Boundary STSS, the increased CO_2 uptake and reduced $p\text{CO}_2$ and a decrease of the biological sink at 50-400 m likely due to more remineralization at this depth. However, the differences in the biological sink of DIC are compensated by mixing of DIC (profiles not shown). Overall, differences of the regional DIC profile to the observational GLODAP climatology slightly increase (Fig. 8g).~~

Coastal SPSS_{NA-} In the Coastal SPSS_{NA-}, $p\text{CO}_2$ is reduced and the ocean CO_2 uptake is increased in ASML during winter and spring (Fig. 7f and j). ~~The reduction of $p\text{CO}_2$~~ is facilitated by colder SST (Fig. 8a). This might be due to subpolar water masses penetrating further south along the coast in ASML because the location where the current separates from the coast is further south in ASML ~~(velocities in Fig. A2)~~.

In summary, DA affects the CO_2 flux in the North Atlantic mainly through ~~horizontal and vertical redistribution changes in SST, combined with changes in horizontal advection of DIC and alkalinity near the NAC. Changes in the vertical mixing of DIC and alkalinity, and through changes in SST. However, which are largely compensated by feedbacks in biogeochemical cycles. Which~~ of these effects is dominant, ~~however~~, varies from region to region.

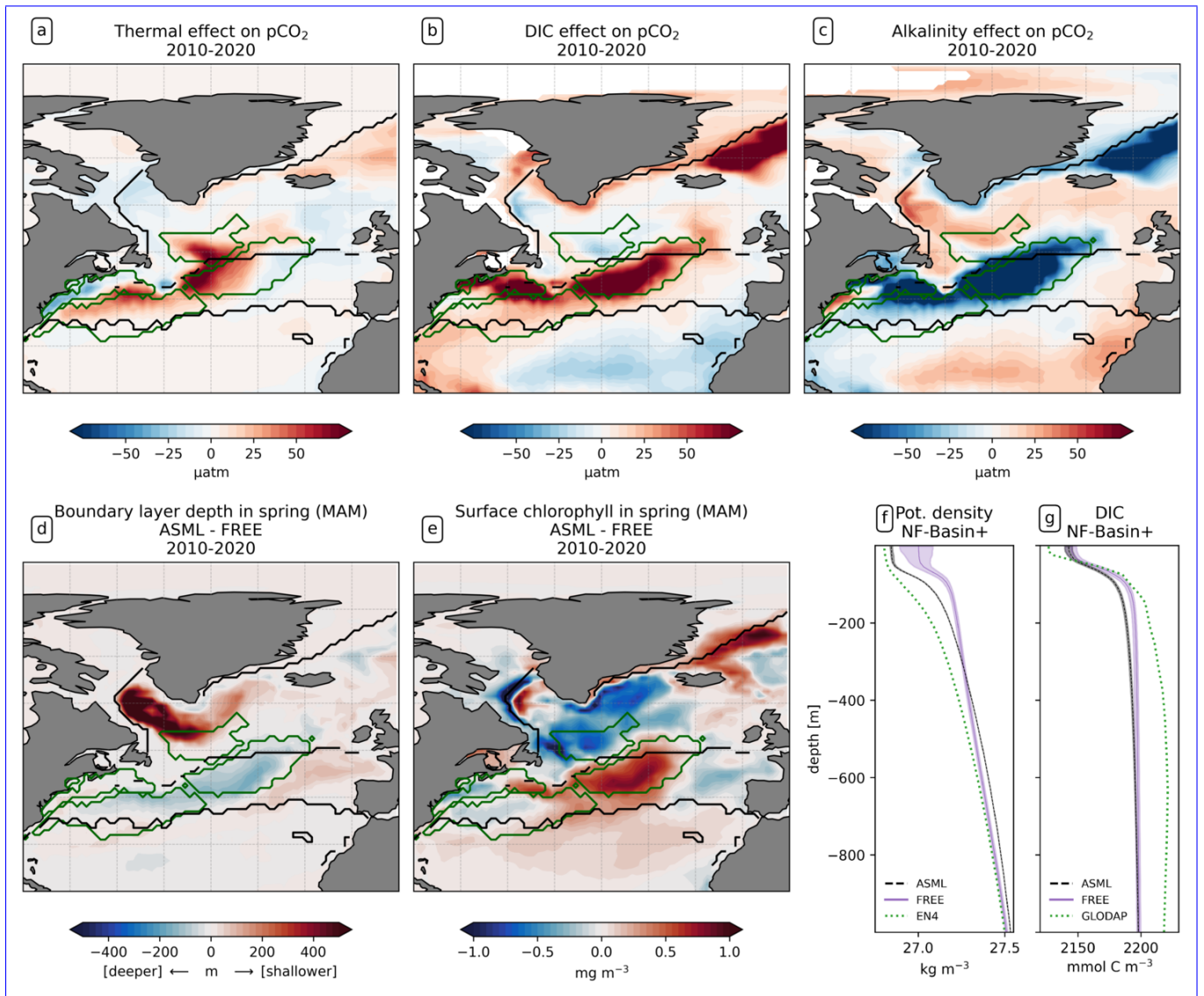


Figure 8. Drivers of the effects of data assimilation on air-sea CO₂ flux in the North Atlantic. Panels a, b and c show the effects of SST, surface DIC and alkalinity differences between ASML and FREE on surface pCO₂. (d) Difference of boundary layer depth (ASML - FREE) for spring (MAM) 2010-2020, where positive denotes a shallower boundary layer in the ASML. (e) Difference of surface chlorophyll (ASML-FREE) for spring (MAM) 2010-2020. (f) Potential density profiles for the Newfoundland Basin⁺ region, with FREE (violet line) and ASML (dashed black line) based on daily T and S, and with EN4-OA (dotted green line) based on monthly T and S. (g) DIC profiles for the Newfoundland Basin⁺ region, showing FREE (violet line), ASML (dashed black line) from 2010-2020 and climatological DIC from GLODAP. [Shading in f and g indicates the range of ensemble members in the year 2020.](#)

660 3.3 Comparison with biogeochemical observations

3.3.1 pCO₂ (SOCAT)

To evaluate the modeled air-sea CO₂ flux based on observations, surface pCO₂ is the most informative variable, as it is closely related to the air-sea CO₂ flux. Effects of the DA on the modeled ecosystem and associated carbon fluxes, as well as thermal and dynamical effects that affect the CO₂ flux, are all included in pCO₂. The global mean of absolute monthly model-observation differences to the available SOCAT pCO₂ observations is ~~27.26 μatm~~ 27.26 μatm for FREE. For ASML, the difference is slightly larger with ~~27.60 μatm~~ 27.60 μatm. On global average, pCO₂ is higher than in SOCAT by ~~3.70 μatm~~ 3.70 μatm in FREE and ~~4.59 μatm~~ 4.59 μatm in ASML, as regions with positive and negative differences to SOCAT compensate (Fig. 9a). ~~The assimilation changes pCO₂ by a mean absolute value of 8.08 μatm~~ As an illustration of the regional changes through DA, the absolute differences in pCO₂ amount to 8.08 μatm (absolute difference ASML-FREE calculated at every grid point then averaged globally), which is ±27% of the mean absolute model-observation difference. A linear offline estimation demonstrates that this change in pCO₂ would lead to an absolute change in the air-sea CO₂ flux by 1.06 mmol C m⁻² day⁻¹ on average (Eq. (8)).

Overall, FREE and ASML show very similar regional pCO₂ differences compared to SOCAT (difference of FREE and SOCAT in ~~(Fig. 9a)~~ Fig. 9a; difference of ASML and SOCAT not shown). In the subtropical and tropical Atlantic and the subtropical Pacific, FREE and ASML have higher pCO₂ than SOCAT, while in the equatorial Pacific, ~~the~~ pCO₂ is lower. At high latitudes, FREE and ASML represent mostly lower pCO₂ than SOCAT.

In the Southern Ocean, the simulations represent lower pCO₂ than SOCAT in the SPSS ~~and ICE_{SO} and ICE_{SO}~~ biomes in the annual mean (Fig. 9c), which is dominated by summer differences to SOCAT (not shown) when most observations are available. Through the assimilation, pCO₂ is slightly increased in summer and mostly reduced in winter (not shown), leading to an overall better agreement with SOCAT (Fig. 9e). In contrast, in the STSS, FREE and ASML represent higher pCO₂ than SOCAT, and through the assimilation, the agreement with SOCAT decreases.

In the North Atlantic, the simulations and SOCAT show a similar large-scale pattern, namely that pCO₂ is higher in the subtropics (ASML: around ~~400 μatm~~ 400 μatm) than in the subpolar regions (ASML: around ~~280 μatm~~ 280 μatm). Yet, this latitudinal difference of pCO₂ is stronger in the simulations compared to SOCAT, meaning that in the subtropics, pCO₂ in the simulations is higher than in SOCAT (Fig. 9d), while it is lower in the subpolar regions. Furthermore, in both simulations there is a pronounced pCO₂ surface gradient in the NAC and North Atlantic Subpolar Gyre region, whose position is changed by the assimilation, and which appears to be further northward in SOCAT. Thereby, the assimilation overall leads to a better agreement with SOCAT, in particular through a decrease of pCO₂ in the Central STSS ~~NA⁻~~, where the average difference is reduced from ~~26 μatm~~ 26 μatm (FREE - SOCAT) to ~~1 μatm~~ 1 μatm (ASML - SOCAT). However, in the Newfoundland ~~basin~~ Basin⁺, the average difference is ~~turned from -17 μatm~~ reversed from -17 μatm (FREE - SOCAT) into ~~13 μatm~~ 13 μatm (ASML - SOCAT), which is associated with a larger absolute discrepancy of ASML and SOCAT.

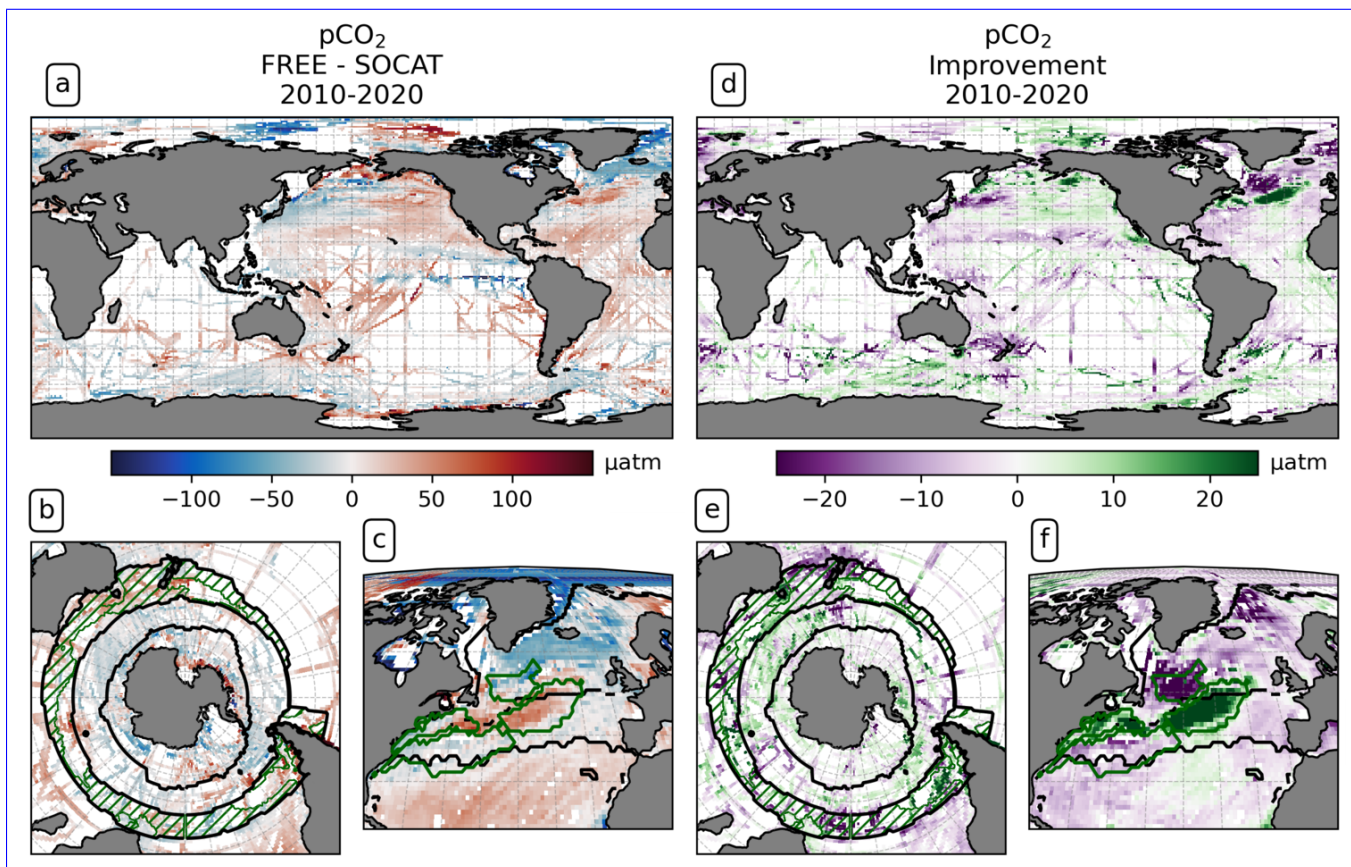


Figure 9. Partial pressure of CO₂ (pCO₂) at the surface averaged over the years 2010-2020. Panels (a-c) show the difference between FREE and SOCAT observations in (a) the global ocean, (b) Southern Ocean and (c) North Atlantic; panels (d-f) show the impact of the assimilation as 'improvement' relative to SOCAT observations computed from monthly mean pCO₂ in the same regions. Positive values (green color) denote a reduced difference to SOCAT.

3.3.2 DIC and alkalinity (GLODAP)

DIC and alkalinity are two of the most important variables from which pCO₂ is derived (Section 3.2). Comparing them with observations provides more insights into the strengths and weaknesses of the modeled carbonate system than a comparison with pCO₂ observations alone. The FESOM-REcoM simulations represent higher surface DIC than GLODAP bottle observations (Lauvset et al., 2024a, gridded monthly-means) on average (Fig. 10a), with a global mean surface difference FREE-GLODAP of 6.46 mmol C m⁻³ for DIC. Although fewer DIC observations are available than pCO₂ observations, similarities between the respective model-observations differences for DIC and pCO₂ can be recognized. For example, DIC in the model is lower in the tropical and subtropical Atlantic than GLODAP, and higher in the polar Atlantic. This is consistent with SOCAT pCO₂ observations in the same areas. The model-observation differences to GLODAP DIC and SOCAT pCO₂ are also consistent with each

other in the north Pacific. The assimilation induces absolute changes in surface DIC of $6.33 \text{ mmol C m}^{-3}$ on global average, with regional differences in sign. These changes slightly reduce the mean absolute difference to the surface observations from $32.78 \text{ mmol C m}^{-3}$ to $32.15 \text{ mmol C m}^{-3}$, and yield a mixed picture of the improvement (Fig. 10b).

705 While the trend in surface DIC due to anthropogenic input makes it necessary to compare the model with contemporaneous observations at the ocean surface, a comparison with climatological data is meaningful below a depth of approximately 200 m. In fact, the modeled global distribution of DIC at depth is overall similar to that in the GLODAP climatology ~~(for both simulations (zonal mean DIC surface to 1000 m depth in~~ Fig. A17). For example, the model results and GLODAP data sets show that DIC is lowest in the isopycnals of the subtropical gyres ($2050 - 2150 \text{ mmol C m}^{-3}$; Fig. A17a) and that DIC mostly increases with depth and is higher in the Pacific ($2420 \text{ mmol C m}^{-3}$ at 1000 m in the North Pacific) than in the Atlantic 710 ($2320 \text{ mmol C m}^{-3}$ below 3000 m in the South Atlantic). Yet, depending on the ocean basin and depth, there can be both negative and positive differences between the simulations and the GLODAP climatology, which are in the order of 20 mmol C m^{-3} (Fig. A17c). On a global average, the assimilation leads to an increase in DIC between 200-600 m depth and a reduction of DIC between the surface and 200m, with the largest effect in the upper 400 m (Fig. A17b). This leads to an improved agreement with the GLODAP climatology, with the largest global mean improvement at a depth of 400 m ($2.5 \text{ mmol C m}^{-3}$; (Fig. A17d). 715 Below 1000 m depth, the global mean absolute difference FREE-ASML of DIC and alkalinity is only $1 - 2 \text{ mmol m}^{-3}$ and is therefore substantially smaller than at the surface.

The comparison with GLODAP bottle alkalinity at the surface shows a similar spatial patterns as for DIC (see Fig. 10a and c). The magnitude of the bias is also comparable ($14 \text{ mmol Alk m}^{-3}$). The global mean of the absolute difference ASML-FREE of surface alkalinity is $7.72 \text{ mmol Alk m}^{-3}$. The assimilation leads to a reduction of the absolute difference of the 720 model alkalinity to GLODAP from $34.34 \text{ mmol Alk m}^{-3}$ to $32.60 \text{ mmol Alk m}^{-3}$. Since the effects of physics assimilation on alkalinity and DIC are regionally consistent, regions of improved or deteriorated agreement with GLODAP often coincide for both variables (compare Fig. 10b and d). ~~Since Because~~ changes of DIC and alkalinity have an opposing effect on the CO_2 flux, it is likely that their correlation results in compensating effects. A linear estimate shows that the joint effect of DIC and alkalinity changes is responsible for a change in the CO_2 flux in the order of $1.22 \text{ mmol C m}^{-2} \text{ day}^{-1}$ on average, and, globally 725 integrated, the assimilation-induced changes in DIC and alkalinity lead to an estimated net increase of the air-sea CO_2 flux ~~by in the order of~~ $0.50 \text{ Pg C yr}^{-1}$ (Eqs. (3), (4) and (8)). However, this linear offline estimate is subject to a large uncertainty ~~because regionally large effects with opposite sign lead to uncertainty in the global mean.~~

3.3.3 Surface chlorophyll (OC-CCI)

The representation of chlorophyll by the model is of interest as a ~~p CO_2 -independent~~ proxy for primary production. Surface chlorophyll reflects the phytoplankton state and biomass, and therefore, effects of the DA on the biological model state can be seen in the total surface chlorophyll concentration. A comparison of the modeled surface chlorophyll with remotely-sensed chlorophyll from OC-CCI reveals that ~~the simulations capture the global distribution of chlorophyll well (Fig. 11). The simulations show the seasonal maxima in each hemisphere around one month earlier in the year (not shown). FREE features~~ both simulations feature a higher surface chlorophyll concentration than OC-CCI ~~by (FREE-OBS in Fig. 11a and c). In FREE,~~

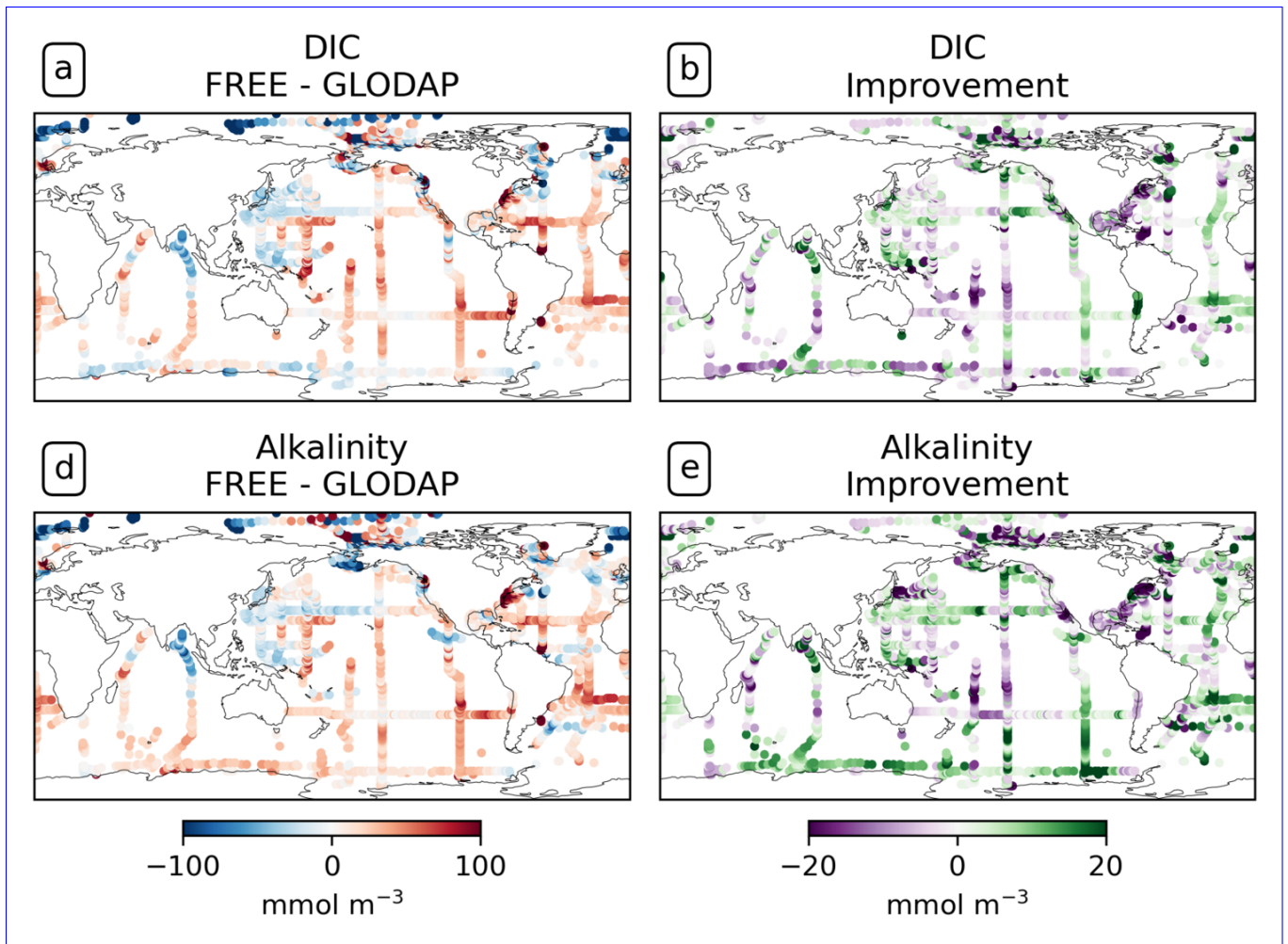


Figure 10. Comparison of the model result with surface DIC and alkalinity bottle observations from GLODAP over the years 2010 to 2020. (a) Difference of DIC between FREE and GLODAP. (b) Improvement of monthly surface DIC relative to GLODAP. (c and d) For alkalinity.

735 the difference to OC-CCI is 0.02 mg m^{-3} on global average, with low deviations in the tropics and an enhanced difference
north of 30°N (0.12 mg m^{-3}) and south of 30°S (0.24 mg m^{-3}) (Fig. 11a. Apart from this, both simulations capture the global
distribution of chlorophyll well. The simulations show the seasonal maxima in each hemisphere around one month earlier in
the year (not shown). South of 30°S , FREE is in better agreement with chlorophyll-a from Johnson et al.'s (2013) Southern
Ocean specific chlorophyll product (Fig. 11ab) than with OC-CCI data (Fig. 11a).

740 On global average, the assimilation slightly reduces the differences between model and OC-CCI data, from a global mean
absolute difference of 0.31 mg m^{-3} to 0.29 mg m^{-3} . The assimilation changes the chlorophyll concentration by an absolute
value of 0.05 mg m^{-3} on average, which is 15% of the global mean absolute difference to OC-CCI. There are regions in which
assimilation leads to a reduction in chlorophyll and thus to better agreement with the satellite products, for example in the
North Atlantic Subpolar Gyre and the Southern Ocean SPSS (Fig. 11b and e_{SO} (Fig. 11e and f). In contrast, the model reacts
745 to the DA with an increase in chlorophyll in the North Atlantic Central STSS_{NA-} and the Argentine Basin (Fig. 11b and f),
which leads to poorer agreement.

4 Discussion

~~The assimilation of physics has different effects on BGC surface variables, though the major effects-~~

The improvement in temperature and salinity overall leads to a heterogeneous picture in biogeochemistry. While near-surface
temperature and salinity fields are improved through DA almost everywhere, the global mean absolute difference of modeled
750 surface pCO_2 to SOCAT remains similar in ASML compared to FREE, and this also applies to the model-observation differences
for surface chlorophyll, DIC and alkalinity (Section 3.3). Where improvements in one BGC variable occur, these do not
necessarily lead to consistent improvement in all BGC variables. For example, the representation of pCO_2 improves while
that of chlorophyll deteriorates in the North Atlantic Central STSS_{NA-} (Fig. 11f and Fig. 9f). In the Southern Ocean SPSS_{SO-},
755 the reduction of modeled surface chlorophyll in spring and the increase of pCO_2 in summer lead to a better agreement
with pCO_2 observations, yet the available observations of DIC and alkalinity do not resolve the regional scales to evaluate
the corresponding changes in these variables (Fig. 9, Fig. 10 and Fig. 11f). The uncertainty represented by the ensemble is
reduced by the DA, which has the most obvious effect on the directly assimilated fields (SST in Fig. 6d and e and density in
Fig. 8f). The ensemble standard deviation of the CO_2 flux, where it is large in FREE, is constrained by the DA to globally
760 more uniform and smaller values (Fig. 5c-f, Fig. 7c-f and Fig. A1). Only in the North Pacific, the standard deviation of
 CO_2 fluxes is equally high in ASML and FREE, precisely in a region that also presents a challenge for pCO_2 products
(compare Fig. A1 and Mayot et al., 2024, Figure 5a). In the rest of the ocean, the reduced uncertainty represented by the ensemble
does not necessarily coincide with improved agreement with BGC observations. One possible reason for improvement of
model-data mismatch in one variable with worsening in another may lie in inconsistencies between the observational datasets.
765 Another reason may be missing processes in the model and the use of constant BGC model parameters. Those parameters
are responsible for linking changes between ecosystem variables and in reality, they vary across space and time depending on
species composition in the ecosystem (Mammun et al., 2023, Chapter 3). Overly simplified links between ecosystem variables

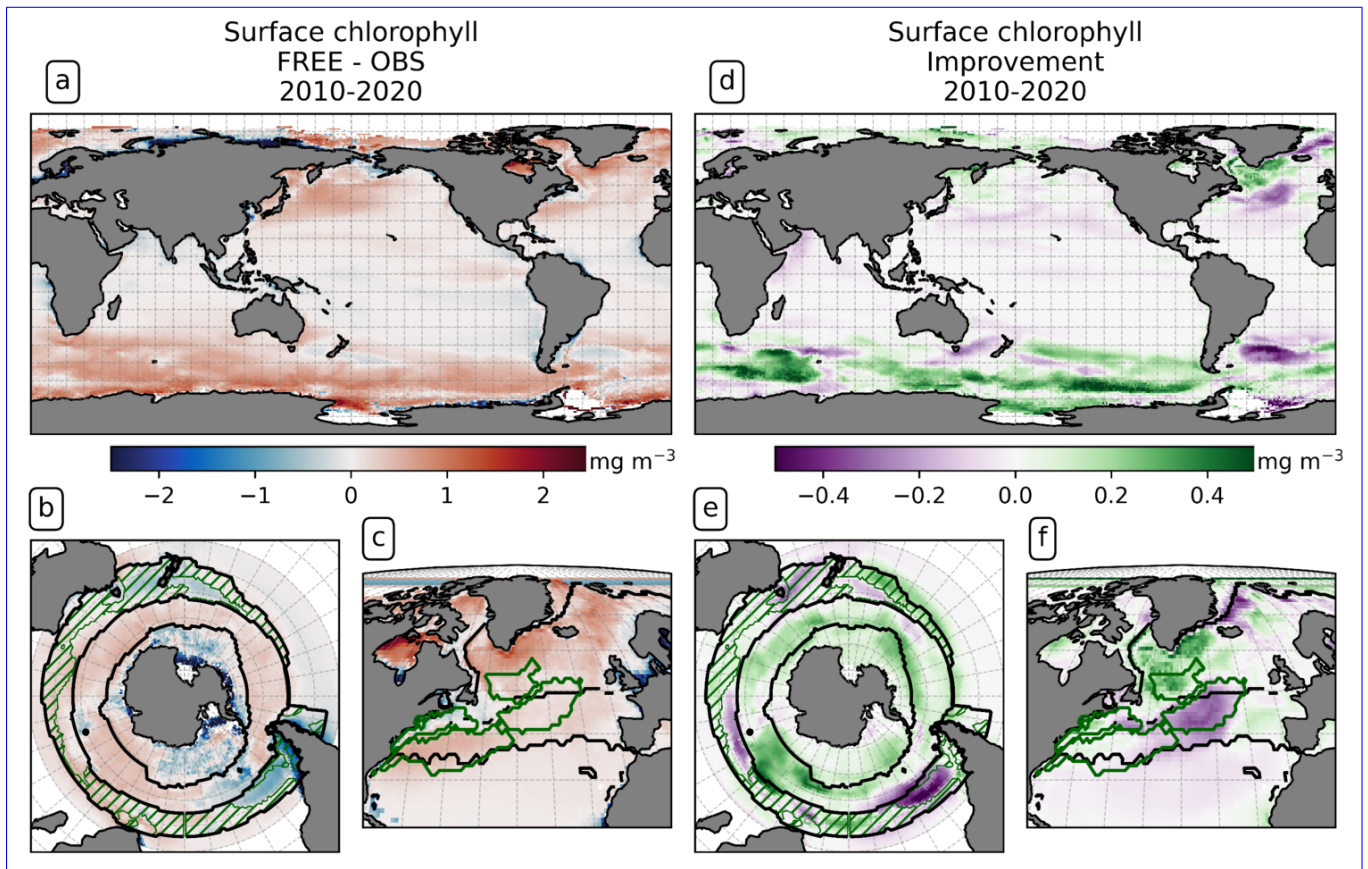


Figure 11. Surface chlorophyll averaged over the years 2010-2020: (a-c) difference between FREE and SOCAT observations in (a) the global ocean, (b) the Southern Ocean and (c) the North Atlantic; (d-f) impact of the assimilation as 'improvement' relative to the observations in the same regions. Panels (a, c, d) and (f) compare to monthly OC-CCI observations, panels (b) and (e) refer to the climatology for 1998-2019 by Johnson et al. (2013).

can lead to cancelling errors, which means that the state of one variable may worsen as a result of improving the other through DA (as in Ford and Barciela, 2017).

770 The major effects of physics DA on BGC variables seem to be related to changes of SST and are largely uniform over the full period of DA (Section 3.3). Surface chlorophyll changes follow SST changes (Fig. 11 and Fig. 1), as the Figs. 1 and 11. The modeled phytoplankton growth is temperature-dependent (Gürses et al., 2023). Furthermore, indirect temperature effects on plankton dynamics due to stratification and mixing changes contribute, albeit those can have heterogeneous effects and the correlation of chlorophyll and boundary-layer depth is less clear (not shown). The changes of surface DIC and alkalinity
 775 show similar spatial patterns with regional heterogeneity (Section 3.2), again with the major changes being coherent with the changes in SST (Fig. 1). Furthermore, the effects of the assimilation on DIC and on temperature in the upper 1000 m correlate regionally. Cooling: Cooling through DA at intermediate depth (Fig. 2b) is usually accompanied by higher DIC

(Fig. A17 in ASML (Fig. A17b), while warming through DA near the surface occurs together with reduced DIC in ASML. An overall more stable ocean stratification in the upper hundreds of meters explains why, on global average, the assimilation leads to lower DIC above 200 m and higher DIC between 200-600 m depth. In regions of substantial DA effects on vertical transport of DIC, as for example in the Central STSS_{NA} or in the SPSS_{SO} (Section 3.2), the modelled biogeochemical cycles adjust dynamically to the altered vertical transport. The resulting changes in biological sources and sinks of DIC compensate for 20-70% of the changes in vertical transport of DIC (Fig. A13a). In addition to changes in stability and mixing, the assimilation affects the distribution of DIC and alkalinity through changes in horizontal and vertical advection, with changes in the horizontal advection being about an order of magnitude larger than in the vertical. The horizontal local changes in near-surface horizontal transport. As the horizontal distribution of surface DIC, alkalinity and SST is governed by latitudinal gradients and common pathways of advective transport, so that transport (Figs. A10 and A15), all of them undergo similar changes as the SST field is modified. The An exception to this is the Southern Ocean STSS, where changes in the horizontal transport in the STSS_{SO}, where regional shifts along contrasting surface gradients of DIC, alkalinity and temperature along contrasting surface gradients affect the respective variables differently (Section 3.2, Fig. A10, Fig. A18). The physics assimilation affects pCO₂ directly through the thermal effect, but also indirectly through changes of DIC and alkalinity, among other factors. Globally, changes in). These shifts change the spatial pattern of air-sea CO₂ fluxes. With the exception of the Southern Ocean, zonally averaged changes in surface pCO₂ are dominated by changes in DIC and alkalinity, but regionally, also the thermal effect can be the combined effects of surface alkalinity and DIC on pCO₂ (Fig. A9a). Because alkalinity and DIC are usually modified according to the same pattern through mechanisms acting on both, their effects on pCO₂ are anticorrelated (Fig. A9b). The direct thermal effect on pCO₂ can still be the largest locally, for example in the North Atlantic Newfoundland Basin (Fig. A12+ (Fig. A12b). While the DA dynamically induces changes in surface pCO₂ globally everywhere, the strongest effects on the air-sea CO₂ flux are at high latitudes, where the pCO₂ changes are amplified by high wind velocities.

The improvement in ocean physics overall leads to a more heterogeneous picture in biogeochemistry. While near-surface temperature and salinity fields are improved through DA almost everywhere, the global net effect of DA on the global air-sea CO₂ flux varies from year to year between $-0.12 \text{ PgC yr}^{-1}$ and 0.15 PgC yr^{-1} , which is small compared to the changes in regional CO₂ fluxes. The global net effect of lateral redistribution of alkalinity and DIC at the ocean surface is a result of compensation between regions where alkalinity and DIC are added and removed. Similarly, regional SST effects on surface pCO₂ mostly balance out globally, because DA primarily induces a correction of regional SST biases, reducing the mean absolute difference of modeled surface pCO₂ to SOCAT remains similar in ASML compared to FREE, and this also applies to the model-observation differences for surface chlorophyll, DIC and alkalinity (Section 3.3). Where improvements in one BGC variable occur, these do not necessarily lead to consistent improvement in all BGC variables. For example, the representation of pCO₂ improves while that of chlorophyll deteriorates in the North Atlantic Central STSS (Fig. 11f and Fig. 9f). In the Southern SPSS, the reduction of modeled surface chlorophyll and the summer increase of pCO₂ in the Southern Ocean SPSS lead to a better agreement with observations, yet the available observations of DIC and alkalinity do not resolve the regional scales to evaluate the corresponding changes in these variables (Fig. 9, Fig. 10 and Fig. 11). One possible reason for improvement of model-data mismatch in one variable with worsening in another may lie in inconsistencies between the observational datasets.

Another reason may be missing processes in the model or the use of constant BGC model parameters. Those parameters are responsible for linking changes between ecosystem variables and in reality, they vary across space and time depending on species composition in the ecosystem (Mamnun et al., 2023, Chapter 3) the observations from 0.59°C to 0.32°C , rather than changing the global mean SST, which differs by only 0.02°C between FREE and ASML. DA-induced differences in vertical transport of DIC are comparably large south of 50°S , but approximately 95% of them are balanced globally by opposing changes in vertical transport further north (vertical transport of DIC in Fig. A13a). In particular, the effect of DA on subduction of DIC through vertical advection into the ocean's deeper layers (not shown), which is the rate-limiting step on oceanic uptake of anthropogenic CO_2 emissions (DeVries, 2022), appears small, which may be due to an insufficient amount of deep observations. Besides, experiments on longer time scales might be necessary to generate a visible effect of deep circulation changes on the ocean's carbon cycle (Cao et al., 2009), which could however lead to imbalances in the CO_2 flux (Lebehot et al., 2019; Kriest et al., 2020; Primeau and Deleersnijder, 2009). Another possible reason why the DA effect on the global CO_2 flux in our simulation is small, is the variable stoichiometry in REcoM. The dynamic biological functioning reduces the sensitivity of critical fields, like DIC, to physical changes (Buchanan et al., 2018). Furthermore, negative feedback effects between surface alkalinity, DIC, atmospheric pCO_2 and air-sea fluxes might reduce the overall response (Bunsen et al., 2024).

The ~~global~~ overall impact of the DA on the air-sea CO_2 flux on a global scale is modest (0.05Pg C yr^{-1}) compared to the differences between other estimates (e.g., a standard deviation of 0.45Pg C yr^{-1} of GOBMs in DeVries et al., 2023). The global air-sea CO_2 flux estimates of FREE and ASML fall in the range of previous model estimates and in the range of previous pCO_2 products (Fig. 4a and b) for the period 2010-2018, during which comparable estimates are available (DeVries et al., 2023). Thus, the overall impact of the DA on the air-sea CO_2 flux on a global scale is modest ($0.05 \text{Pg C dec}^{-1}$) compared to the differences between other estimates (e.g., a standard deviation of $0.20 \text{Pg C dec}^{-1}$ in DeVries et al., 2023). However, regionally, the effects of DA are more pronounced.

There are ~~We compare here to~~ two other data assimilating BGC model approaches, namely ECCO-Darwin (global; Carroll et al., 2020) and B-SOSE, which is restricted to the Southern Ocean (Verdy and Mazloff, 2017). Both approaches use Linearized Least Squares Optimization data assimilation methods (4D-var/adjoint and Green's function, Wunsch, 1996; Menemenlis et al., 2005). However, the largest difference to our study is probably that they assimilate BGC observations in addition to physical data. Thus, as expected, the effect on pCO_2 in our study is smaller (3%) than in ECCO-Darwin and B-SOSE where a reduction in pCO_2 ~~model data model data~~ misfit of 6% and 64% was reported, respectively (here given as quadratic misfit).

The global CO_2 flux (2010-2018) is smaller in FESOM2.1-REcoM3-PDAF ($-2.73 \text{Pg C dec}^{-1}$ ~~$-2.73 \text{Pg C yr}^{-1}$ in FREE and $-2.78 \text{Pg C yr}^{-1}$ in ASML~~) than in ECCO-Darwin ($-3.13 \text{Pg C dec}^{-1}$) (2010-2018). The global CO_2 flux in ASML is similar to FREE and does not drive the estimate closer towards the higher estimates of the ECCO-Darwin or the observation-based pCO_2 products ($-2.87 \text{Pg C dec}^{-1}$). Similarly, the trend and interannual variability of the CO_2 flux is hardly changed by the assimilation, suggesting that a flawed representation of ocean physics as an argument for the models underestimating the CO_2 flux trend is unlikely.

~~$-3.13 \text{Pg C yr}^{-1}$~~ The discrepancy between the CO_2 flux estimates based on models and pCO_2 -products is an area of active research and is not fully resolved (Friedlingstein et al., 2023; DeVries et al., 2023). On the one hand, model biases in the

~~AMOC~~Atlantic Meridional Overturning Circulation, in Southern Ocean ventilation and possibly biases in the surface ocean carbonate chemistry were suggested as reasons why models might underestimate the global mean CO₂ uptake in recent decades (Friedlingstein et al., 2023; Terhaar et al., 2024, 2022). On the other hand, the sparsity of observations is a concern for the pCO₂ products. According to one testbed simulation, the pCO₂ products reflect the global mean and the seasonal cycle relatively well, while the decadal variability may be overestimated (Gloege et al., 2021). An overestimation of the decadal trend, as suggested by Hauck et al. (2023b), could explain the high estimates of the pCO₂ products for the present-day global mean CO₂ flux. In contrast, for the North Atlantic, it was argued that pCO₂ is comparatively well constrained by observations in the last decade but not in the 1980s, which has an erroneous influence on the long-term trend (Pérez et al., 2024).

The effects of data assimilation on the CO₂ flux are most pronounced in the Southern Ocean ~~STSS~~and SPSS_{SO} and SPSS_{SO} in winter. Verdy and Mazloff (2017) also found the largest effects of assimilation on the CO₂ flux in this region. Although the region is of crucial importance for the global ocean carbon sink, it also has the greatest uncertainty due to the lack of ship-based winter observations (Friedlingstein et al., 2023; Hauck et al., 2020). In the last decade, the number of winter observations has increased due to the introduction of biogeochemical Argo floats (Johnson et al., 2017; Williams et al., 2017), although the float-based pCO₂ derived from pH measurements and estimated alkalinity is subject to higher uncertainty compared to direct pCO₂ measurements (Williams et al., 2017; Bakker et al., 2016). Machine learning approaches incorporating BGC Argo float observations suggest a stronger winter outgassing around Antarctica, particularly south of 50°S in the ~~SPSS~~and ICE_{SO} and ICE_{SO} biomes, for 2015-2017 (Bushinsky et al., 2019; Gray et al., 2018). This results in a lower estimate of annual Southern Ocean CO₂ uptake in the float products. One suggestion in the literature ~~was~~is that model inadequacies in the representation of mixing and upwelling in the Southern Ocean ~~could~~might cause the discrepancy between float products and models (Gray et al., 2018). However, improvements in the modeled ocean physics and changes in mixing through data assimilation do not lead to ~~not lead to~~ closer agreement between the FESOM-REcoM estimate and the float products (comparison of FESOM-REcoM, float products and B-SOSE in Fig. A14). In contrast, ASML shows even weaker winter outgassing and stronger summer uptake south of 50°S than FREE, which brings the FESOM-REcoM estimate further away from the float products. However, ASML is brought close to B-SOSE in terms of winter outgassing in the Antarctic polar ocean (~~south of 60°S~~) and winter uptake in the STSS(at_{SO} around 40°S). Additionally, airborne CO₂ flux estimates and direct pCO₂ measurements stemming from a sail drone have questioned the estimates of winter outgassing based on the BGC floats, either attributing the high pCO₂ values to possible biases in the floats' measuring devices or to anomalously high pCO₂ in the years 2015-2016 (Long et al., 2021; Sutton et al., 2021). ~~Based on the assumption of preindustrial steady state conditions, a larger natural CO₂ outgassing in the Southern Ocean needs to be compensated by other ocean regions (Gray et al., 2018). The regional differences caused by the data assimilation in the Southern Ocean and elsewhere largely balance out globally and appear to be shifts in the areas where outgassing occurs. These regional shifts follow shifts in sea surface temperature and the distribution of dissolved inorganic carbon (DIC) and alkalinity.~~

~~The comparably small effect of physics DA on the air-sea CO₂ flux suggests that the physical processes are already well-represented in FREE when compared to the uncertainties arising from the biogeochemistry model. The response of REcoM to changes in model physics might be small due to its variable stoichiometry, as the study by (Buchanan et al., 2018)~~

indicated that dynamic-biological functioning reduces the sensitivity of critical fields, like carbon, to physical changes. Furthermore, negative feedback effects between alkalinity, DIC, atmospheric pCO₂, and air-sea fluxes might reduce the overall response (Bunsen et al., 2024). While surface physics are well constrained in the ASML run, questions remain about the dynamics of the mixed-layer and deep-ocean. Experiments on decadal or longer time scales might be necessary to represent the adjustment of the ocean's carbon cycle to changes in the circulation (Cao et al., 2009). In ASML though, the effect on the CO₂ flux is already as strong in the first two years as at the end of the period, and it appears to be governed by interannual variability rather than showing a continuous adjustment. Despite the higher resolution in dynamic regions of the North Atlantic and the Arctic, strong currents and their exact locations, such as the North Atlantic Current and Antarctic Circumpolar Current, are challenging for the model to resolve. These are improved through the assimilation, which is the basis for realistically modeling biogeochemistry in these regions as well.

5 Conclusion

We apply data assimilation of temperature and salinity into a global ocean-biogeochemical model to improve the physical state for the years 2010-2020. The simulation is then assessed with regard to the effects on the biogeochemical variables. The experiments show that the effect of data assimilation (DA) on biogeochemical variables is mostly related to temperature changes. While the air-sea CO₂ flux and pCO₂ are directly affected by sea surface temperature, the DA also induced indirect changes to pCO₂ through dissolved inorganic carbon (DIC) and alkalinity. Globally integrated, these are more relevant for pCO₂ than the direct temperature effect. Yet, which of these factors has a dominant effect on pCO₂ varies locally. The assimilation leads to changes in the horizontal advection of DIC and alkalinity, thereby regionally shifting regional shifts in areas of CO₂ outgassing and uptake. Local effects on the air-sea CO₂ flux are particularly large in dynamic regions such as the North Atlantic Current and near the Subantarctic Front, whose pathways are challenging for the model to resolve without DA. The largest effect on the air-sea CO₂ flux occurs in the Southern Ocean during winter. In the simulation with assimilation, the uptake south of 50°S is increased due to shallower mixing and surface cooling, and the uptake northward of that (40-50°S) is weakened. In this part-area of the ocean, the uncertainty in current estimates of CO₂ fluxes is particularly high. Furthermore, the assimilation has locally strong effects in the area of the North Atlantic current. Overall, the uncertainty inherent to the biogeochemical model appears to be larger than the uncertainties induced through physical biases in the free running model. Locally, the changes in surface pCO₂, chlorophyll, alkalinity, and DIC caused by the assimilation are of the magnitude of 15-30% range between about 15 and 30% of the mean absolute model-observation difference. Yet, local improvements in one variable do not necessarily come along with improvements across other observed biogeochemical variables. Therefore, globally, physics DA does not generally improve the difference between the model and observations. In total, the effect of physics DA on the global ocean carbon uptake is small with 0.05 Pg C yr⁻¹ small compared to the spread between previous estimates of models, pCO₂ products and other DA estimates. While the assimilation of temperature and salinity improves the physical state, representation of these two and also of mixed-layer depth, sea-ice concentration and horizontal near-surface velocities, possible errors in the mixed-layer depth vertical velocities and overturning circulation are not fully eliminated. Further biogeochemical variables are

only indirectly affected. To this end, the additional assimilation of biogeochemical observations is an obvious next step to reduce the uncertainty stemming from the ecosystem model and to improve the ~~model-observation~~ model-observation differences for biogeochemical variables.

Code and data availability. The code used to perform the free simulation and the data assimilation is available at [10.5281/zenodo.11495274](https://zenodo.org/record/11495274).

920 This code archive additionally contains a notebook to produce the manuscript figures from the model output. The processed model output data underlying the figures of this manuscript are available at [10.5281/zenodo.11495081](https://zenodo.org/record/11495081).

Appendix A

Table A1. List of tracers in REcoM3

Tracers in REcoM3
Dissolved inorganic nitrogen and carbon (DIN, DIC)
Dissolved organic nitrogen and carbon (DON, DOC)
Alkalinity
Oxygen
Iron
Silicate
Intracellular concentrations of nitrogen, carbon, chlorophyll, and calcium in small phytoplankton (PhyN, PhyC, PhyChl, PhyCalc)
Intracellular concentrations of nitrogen, carbon, chlorophyll, and silicate in diatoms (DiaN, DiaC, DiaChl, DiaSi)
Intracellular concentrations of nitrogen and carbon in each of two zooplankton groups (HetN, HetC, Zoo2N, Zoo2C)
Two size classes of detritus for nitrogen, carbon, silicate, and calcium (DetN, DetC, DetSi, DetCalc; and DetZ2N, DetZ2C, DetZ2Si, DetZ2Calc)

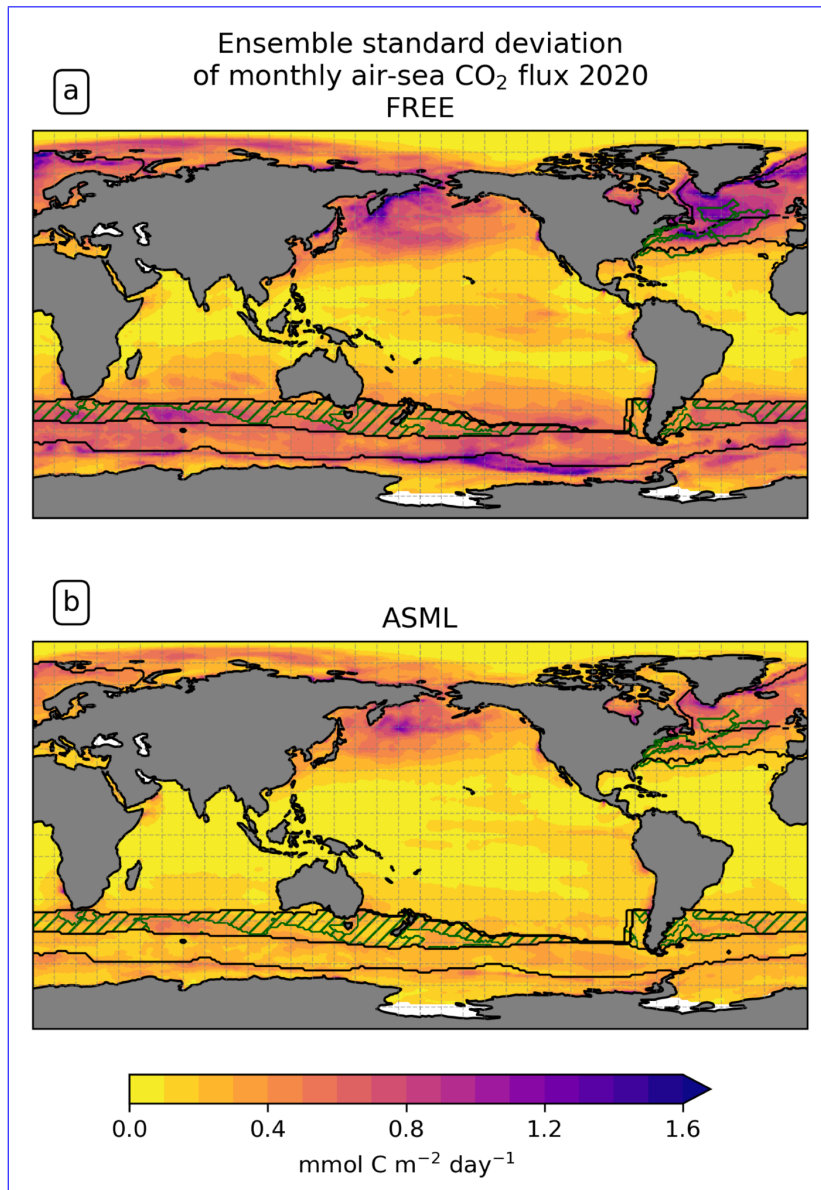


Figure A1. Ensemble standard deviation of monthly air-sea CO₂ flux in the year 2020 in (a) FREE and (b) ASML.

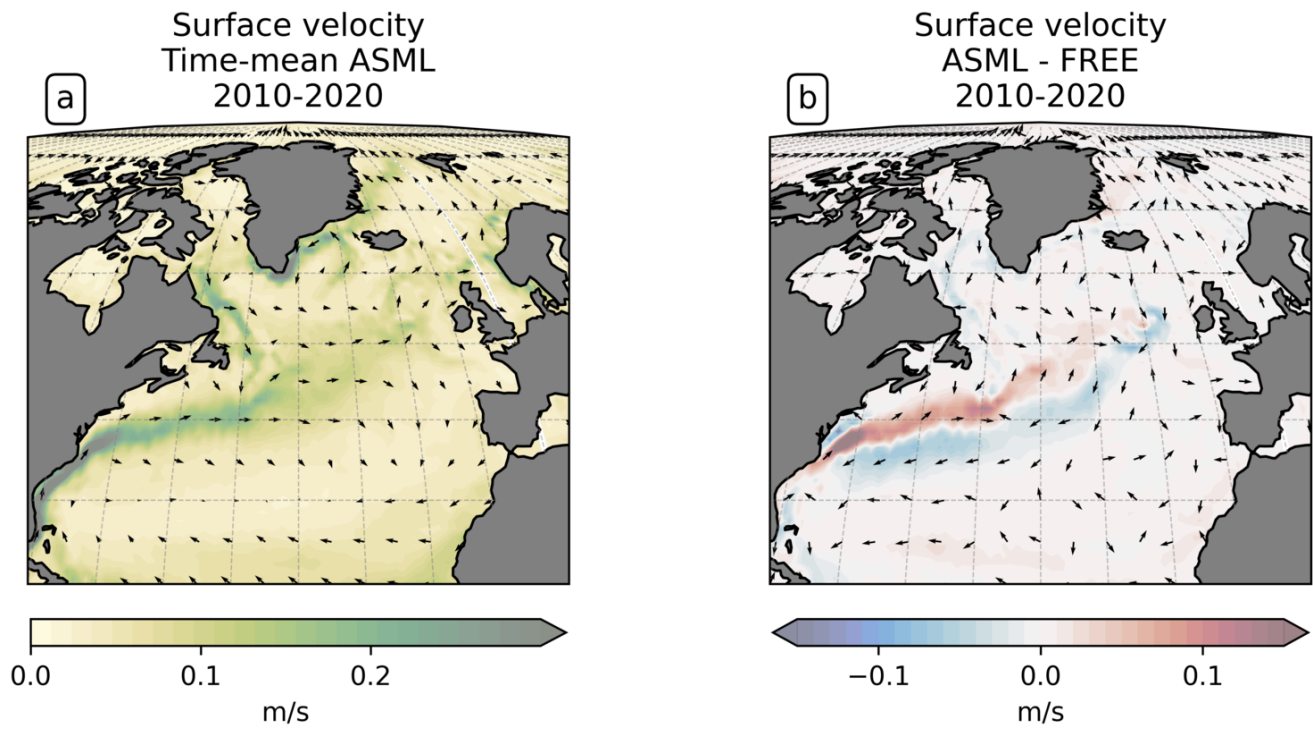


Figure A2. [North Atlantic surface velocities, \(a\) time-mean in ASML and \(b\) difference ASML-FREE.](#)

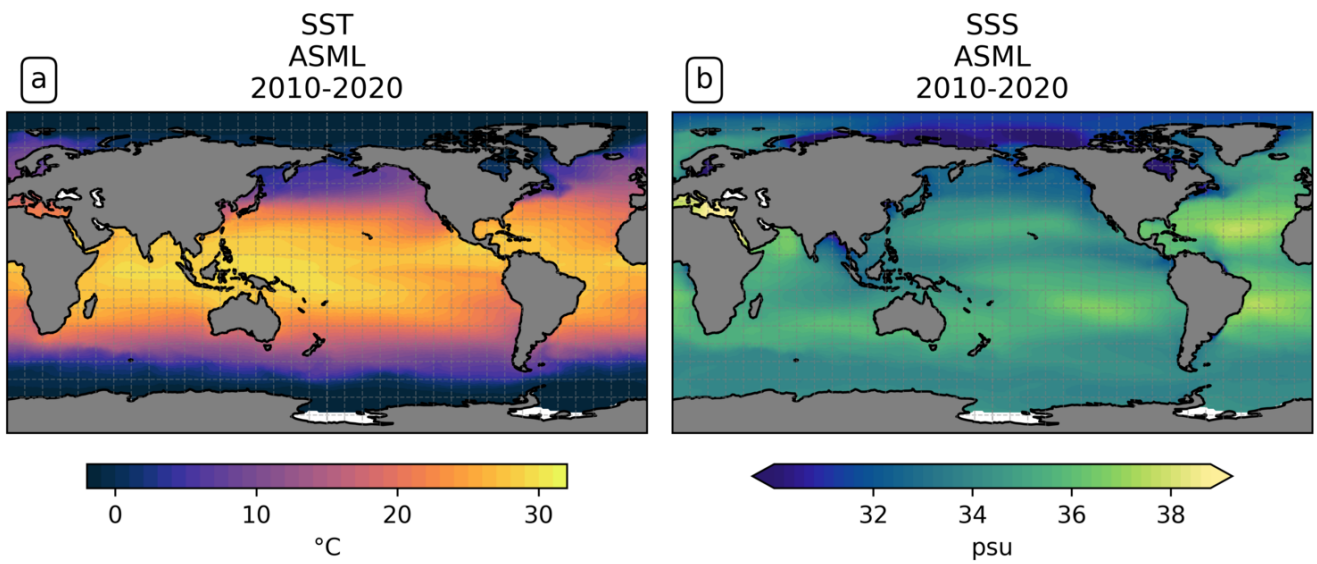


Figure A3. Time-mean sea surface (a) temperature and (b) salinity in ASML.

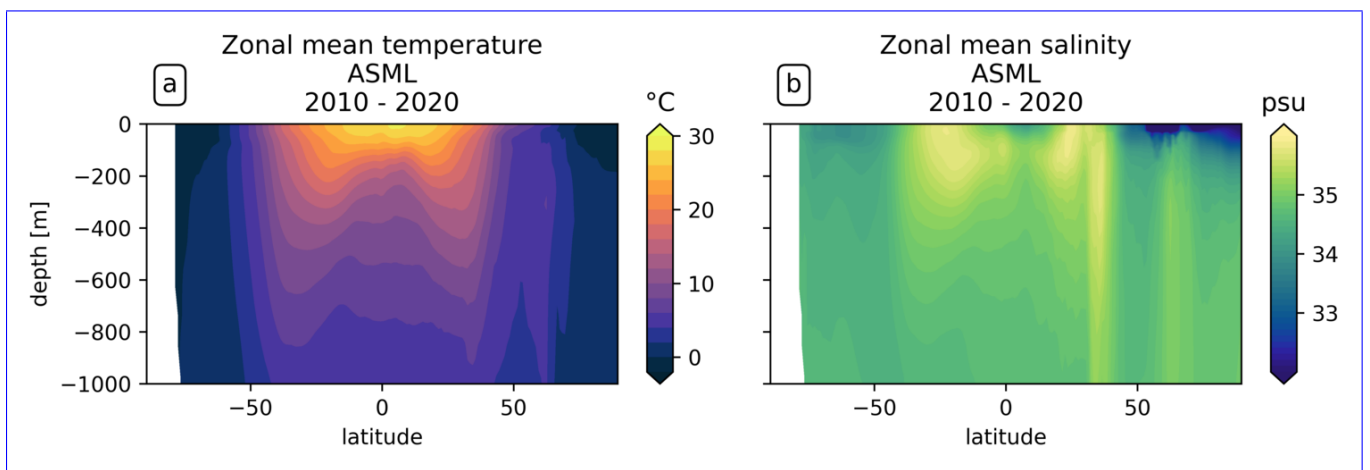


Figure A4. Zonally averaged time-mean (a) temperature and (b) salinity in ASML.

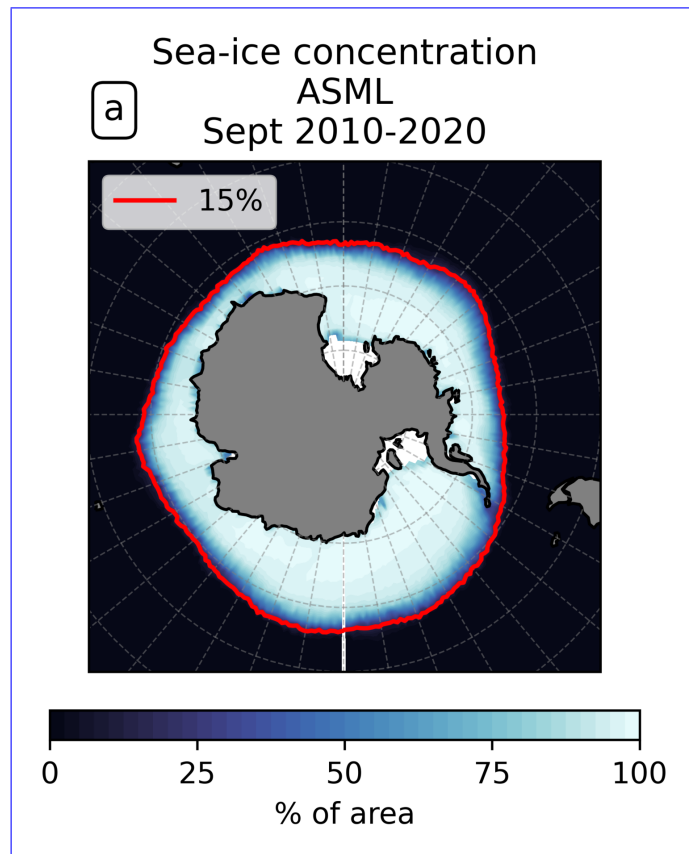


Figure A5. September mean ~~antaretic~~ Antarctic sea-ice concentration in ASML.

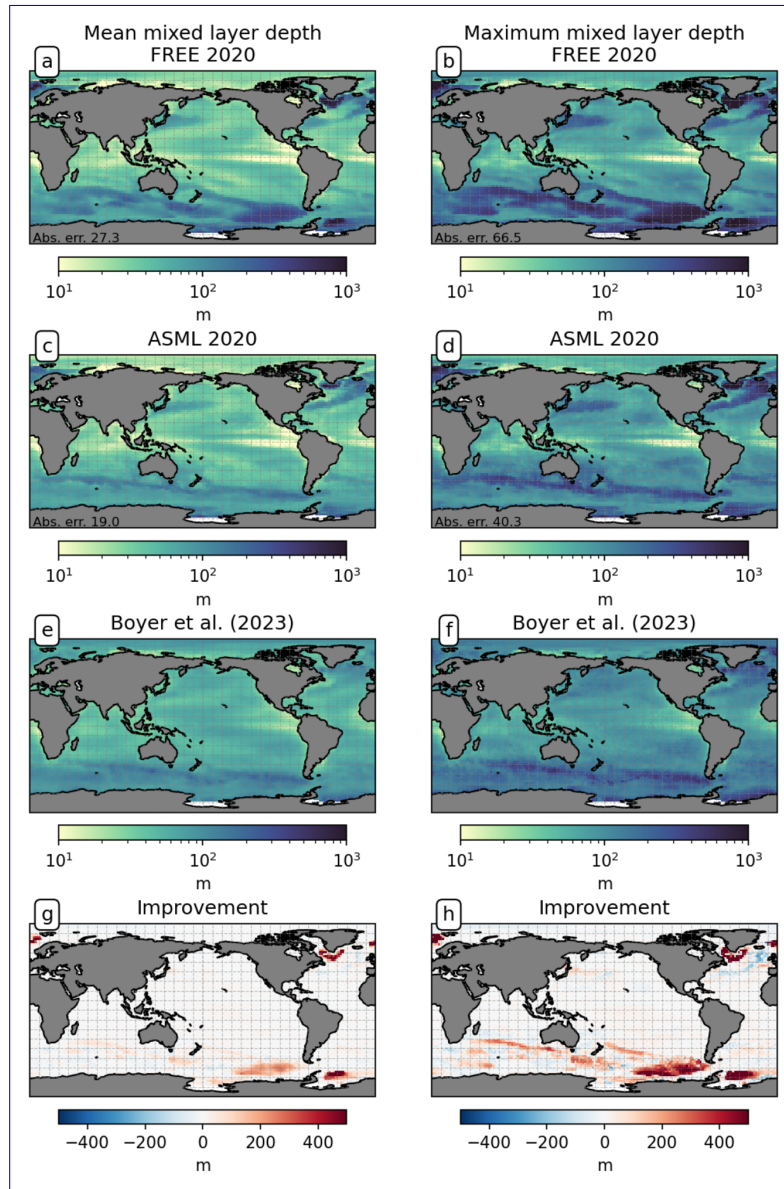


Figure A6. Zonally-averaged winter Mixed-layer depth (JJA) air-sea CO₂ flux in FREE and (c,d) ASML in the year 2020, (e,f) de Boyer Montégut et al.'s (2004) profile-based climatology v2023 and previous estimates (DeVries et al., 2023; Verdy and Mazloff, 2017) (g,h) the improvement through DA relative to the climatology. On the left: time-mean mixed layer, on the right: maximum of monthly-mean mixed layer. For FREE and ASML (a,b,c,d), the mean absolute difference to the climatology is given in the bottom-left corner.

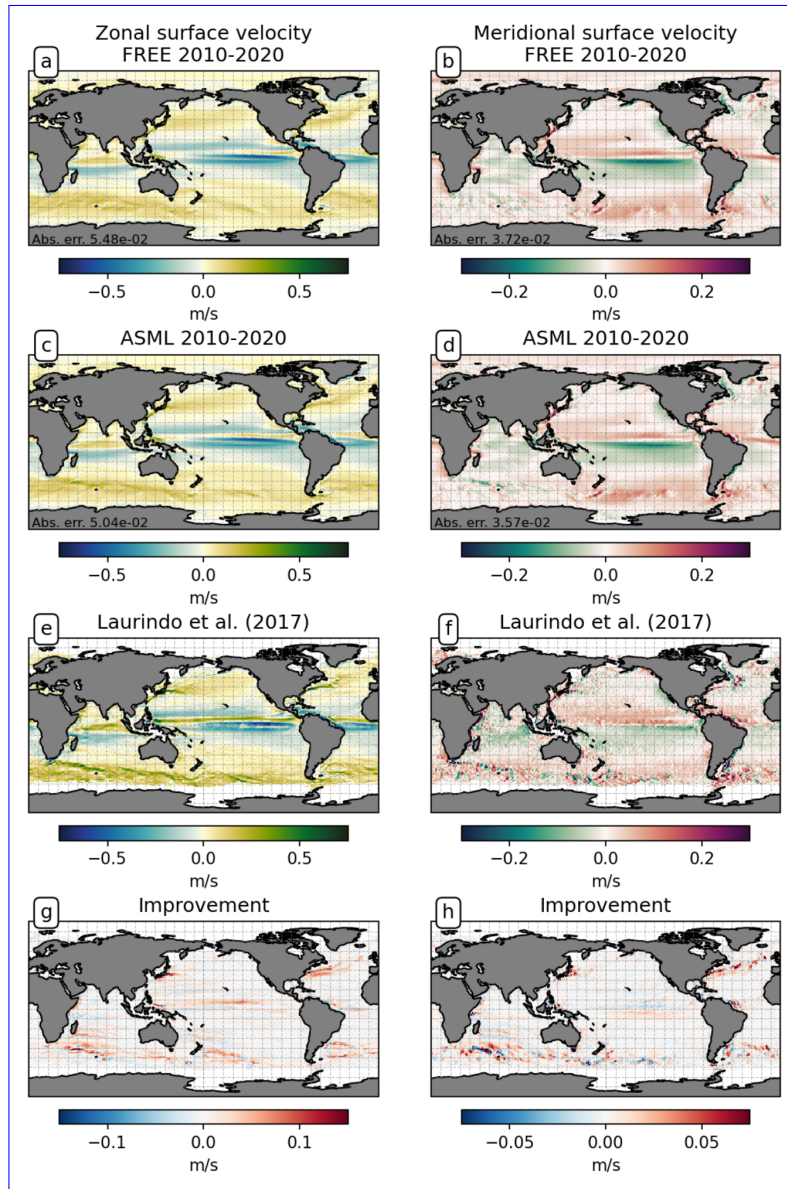


Figure A7. Southern Ocean time-mean sea surface in ASML, Near-surface velocities (a) temperature, (b) salinity, in FREE and (c, d) dissolved inorganic carbon-ASML for the period 2010-2020, (E) Laurindo et al.'s (2017) climatology from drifter observations and (g, h) the improvement through DA relative to the climatology. On the left: zonal velocities, on the right: meridional velocities. For FREE and ASML (a, b, c, d) alkalinity, the mean absolute difference to the climatology is given in the bottom-left corner.

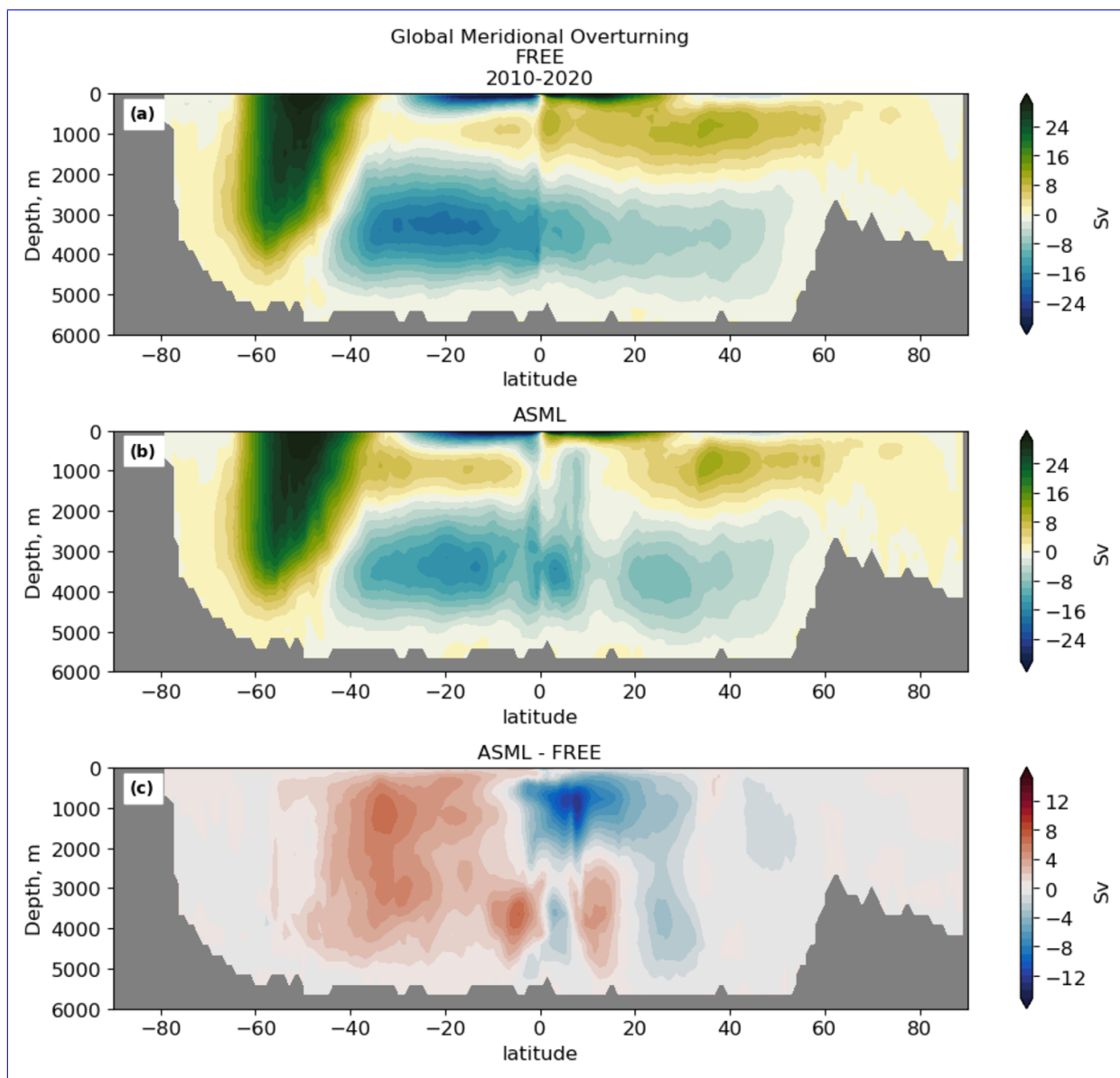


Figure A8. Surface velocities Global meridional overturning in the Southern Ocean, (a) time-mean in FREE, (b) ASML and (c) difference ASML-FREE.

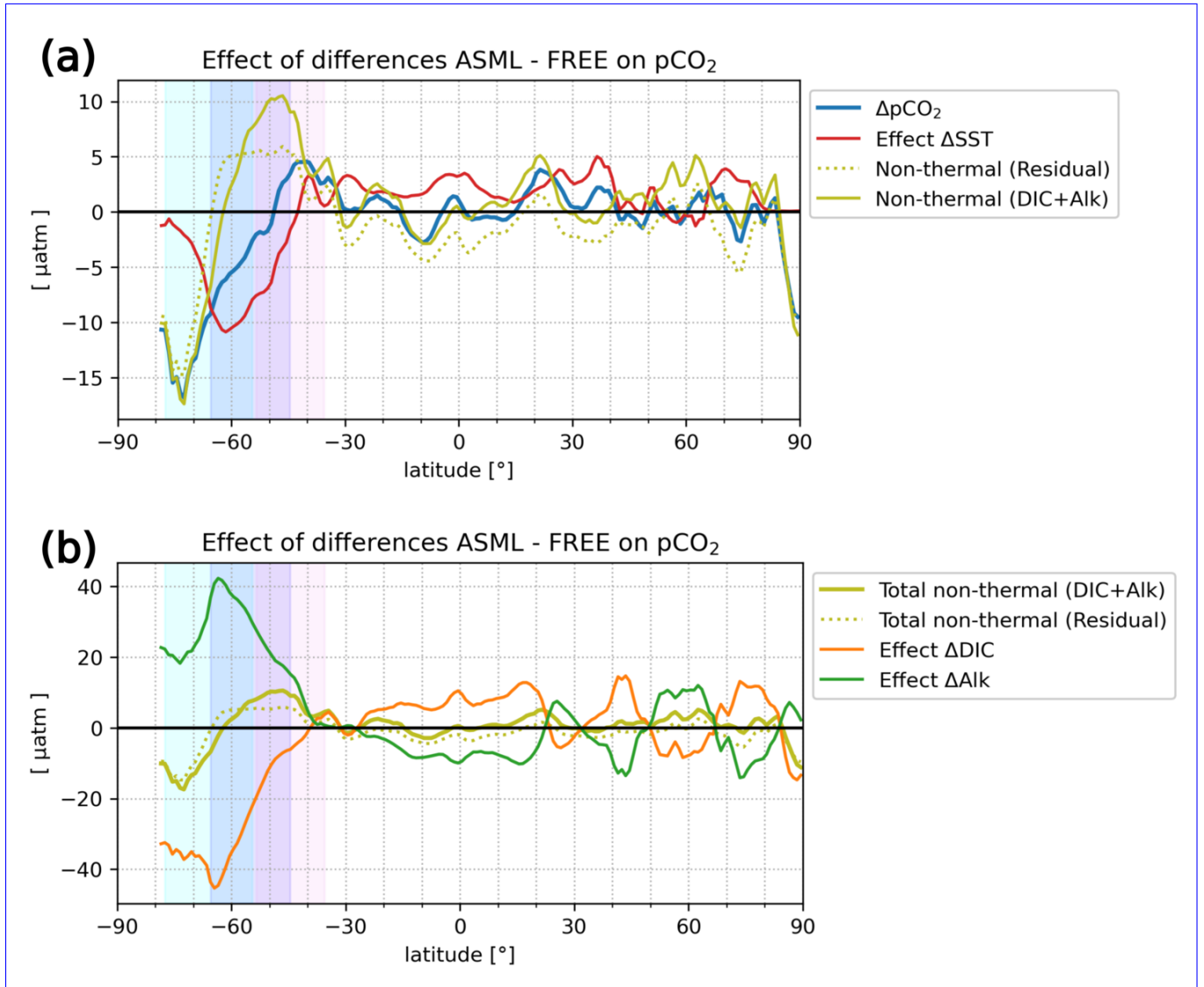


Figure A9. North Atlantic time-mean sea-ice The net difference (ASML-FREE) of surface in-ASML pCO₂ by latitude (panel a, blue line), and the offline-approximated effects causing that pCO₂ difference for the period 2010-2020: Thermal effect (panel a, red line) temperature; non-thermal effect calculated, firstly, as the residual i.e. net-minus-thermal (panels a and b, light-green dotted lines) salinity and, secondly, as the sum of alkalinity and DIC effects (epanels a and b, light-green solid lines) dissolved inorganic carbon (DIC); and effects of alkalinity and DIC individually (dpanel b, orange and dark-green lines) alkalinity. The shaded areas in the background indicate the zonal extent of defined biomes in the Southern Ocean: ICE_{SO} in light-blue, SPSS_{SO} in blue and STSS_{SO} in pink. Colors blend where the regions overlap.

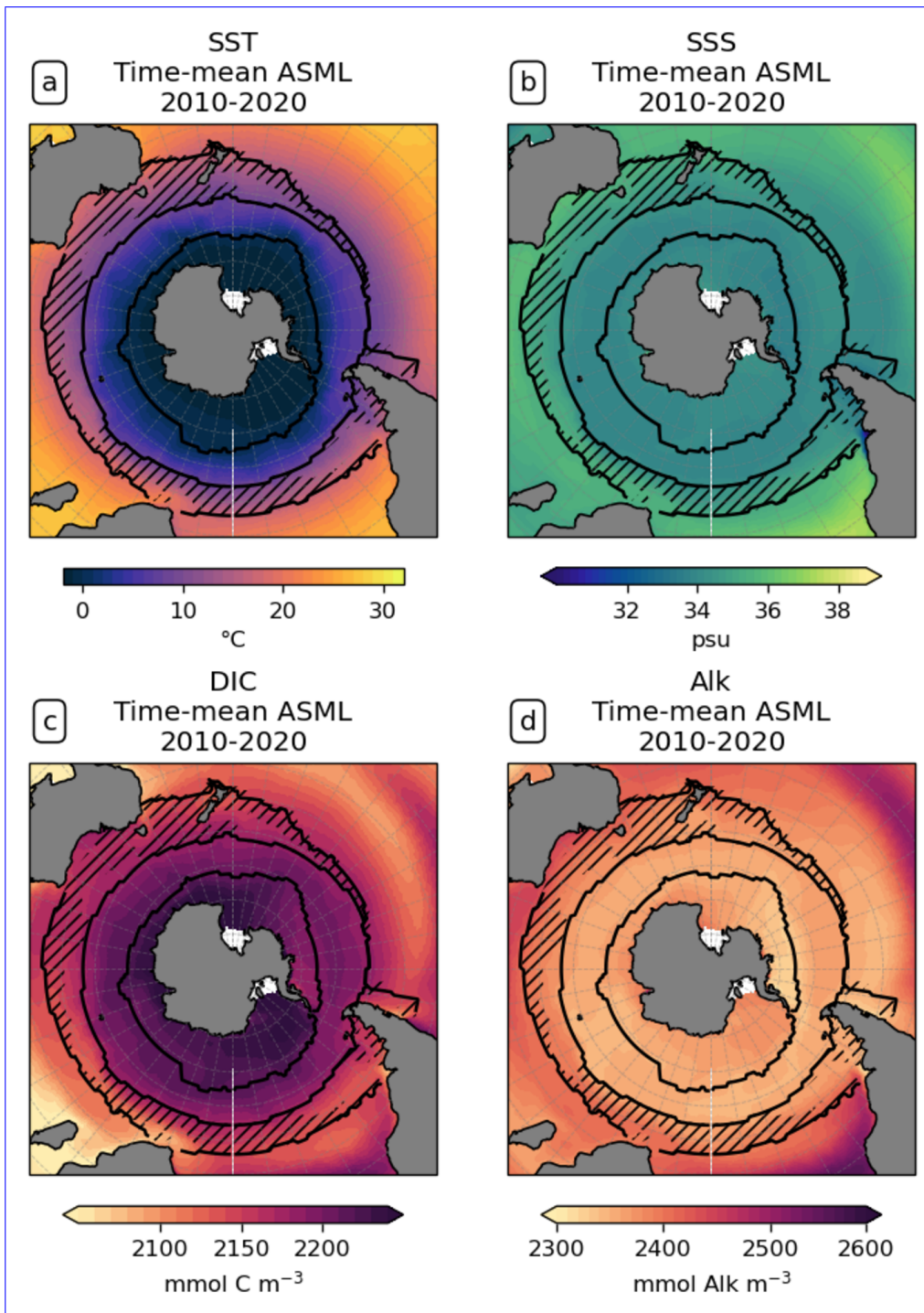


Figure A10. North Atlantic-Southern Ocean time-mean sea surface velocities in ASML, (a) time-mean in ASML and temperature, (b) difference ASML-FREE salinity, (c) DIC and (d) alkalinity.

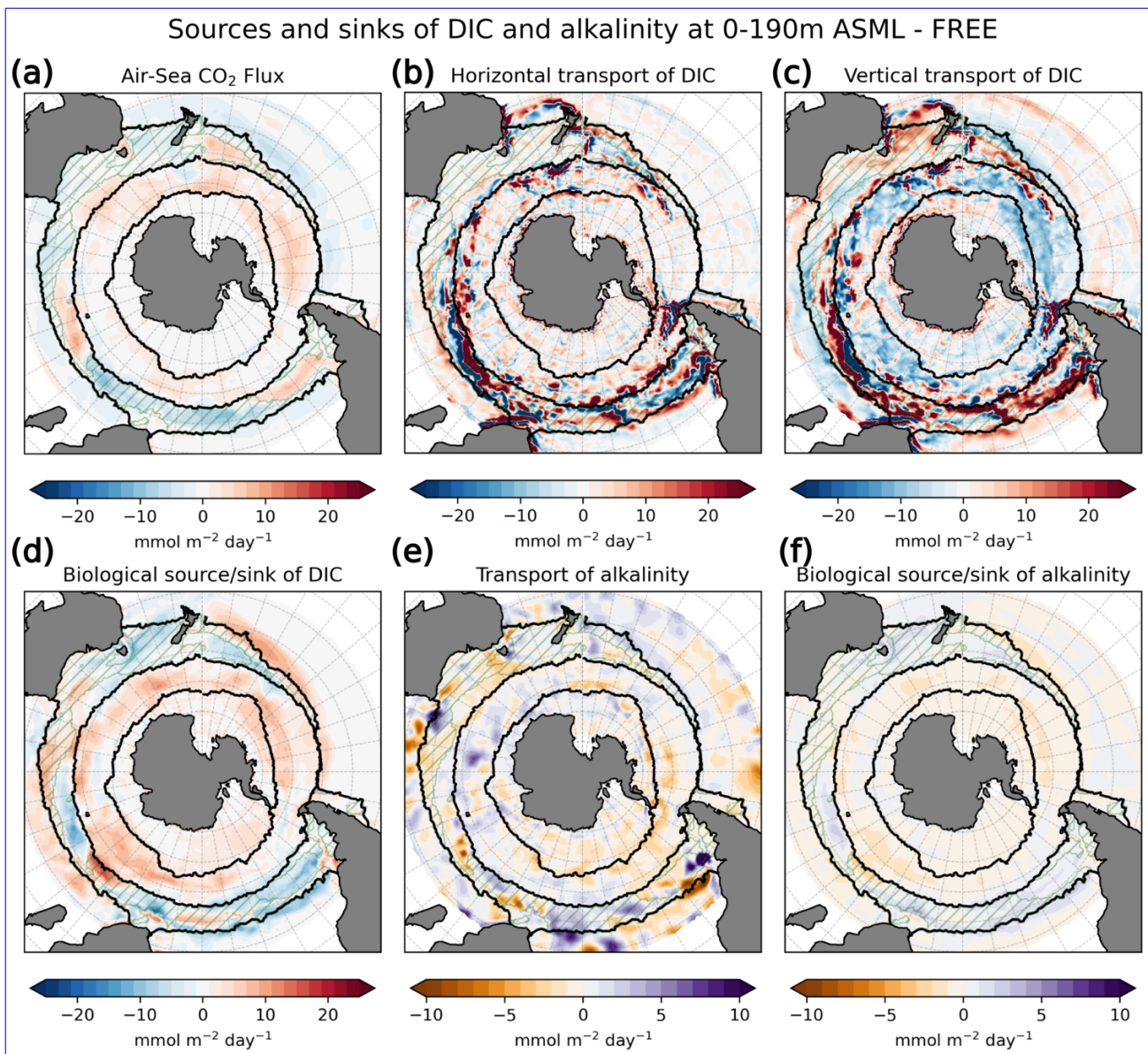


Figure A11. Zonally-averaged dissolved inorganic carbon (DIC), (a) time-mean in ASML, (b) The difference ASML-FREE, (c) ASML-FREE difference FREE-OBS compared to of source and sink terms for the GLODAP climatology ocean's DIC and alkalinity content integrated over 0-190 m in the Southern Ocean in the year 2020. Transport terms include advection and diffusion of DIC and alkalinity. Biological terms for DIC (Lauvset et al., 2016) are the sum of: photosynthesis, respiration, remineralization of dissolved organic carbon, and (d) improvement respective to formation and dissolution of calcite. Biological terms for alkalinity are the GLODAP climatology sum of: nitrogen assimilation and remineralization, and formation and dissolution of calcite.

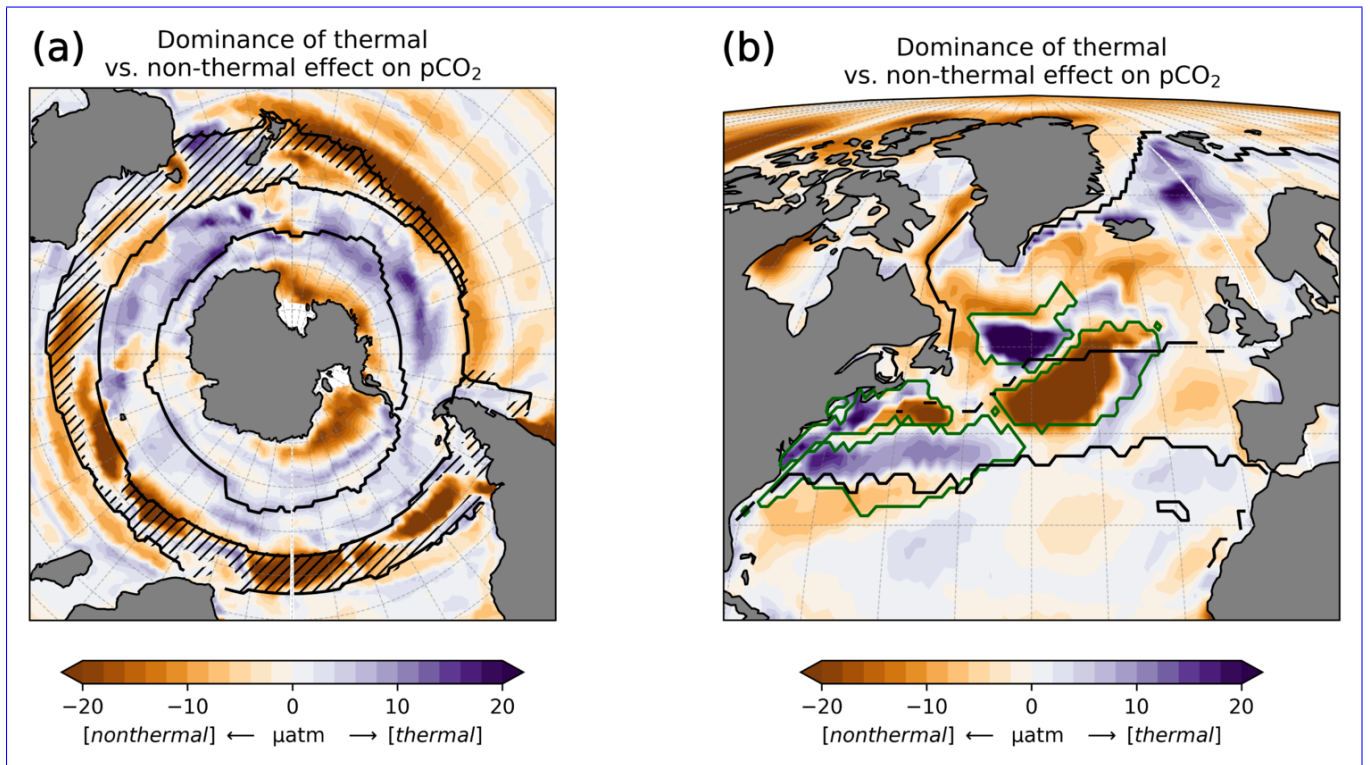


Figure A12. Linear offline estimate of the dominance of thermal versus the non-thermal effect through the assimilation on $p\text{CO}_2$ [in the Southern Ocean and North Atlantic for the period 2010-2020](#).

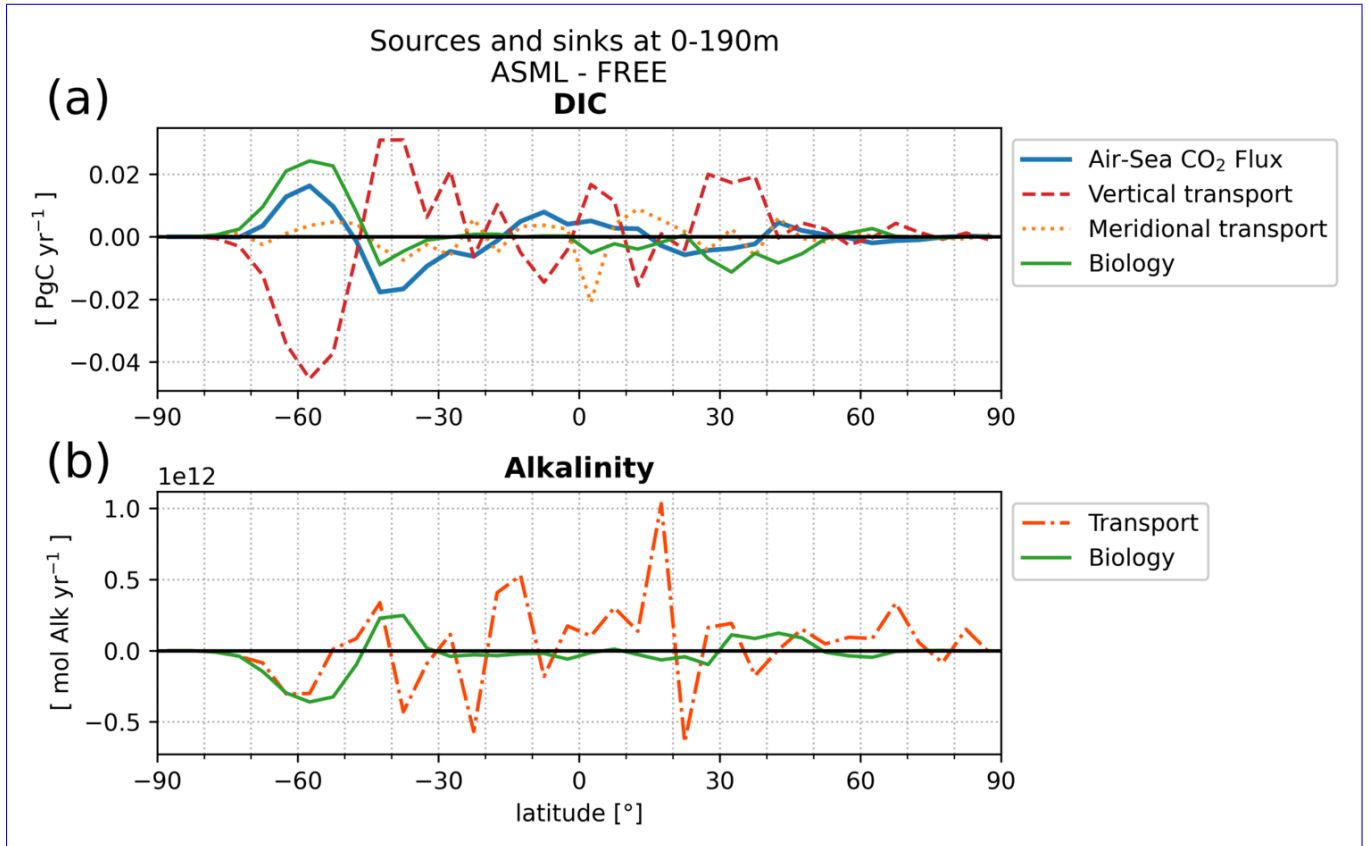


Figure A13. The difference (ASML-FREE) of source and sink terms for the ocean's (a) DIC and (b) alkalinity content integrated over 0-190 m per 1° latitude in the year 2020. Transport terms include advection and diffusion of DIC and alkalinity. Meridional transport is averaged across bins of 5° latitude. In panel b, vertical and horizontal transport are summed up for readability. Biological terms for DIC are the sum of: photosynthesis, respiration, remineralization of dissolved organic carbon, and formation and dissolution of calcite. Biological terms for alkalinity are the sum of: nitrogen assimilation and remineralization, and formation and dissolution of calcite.

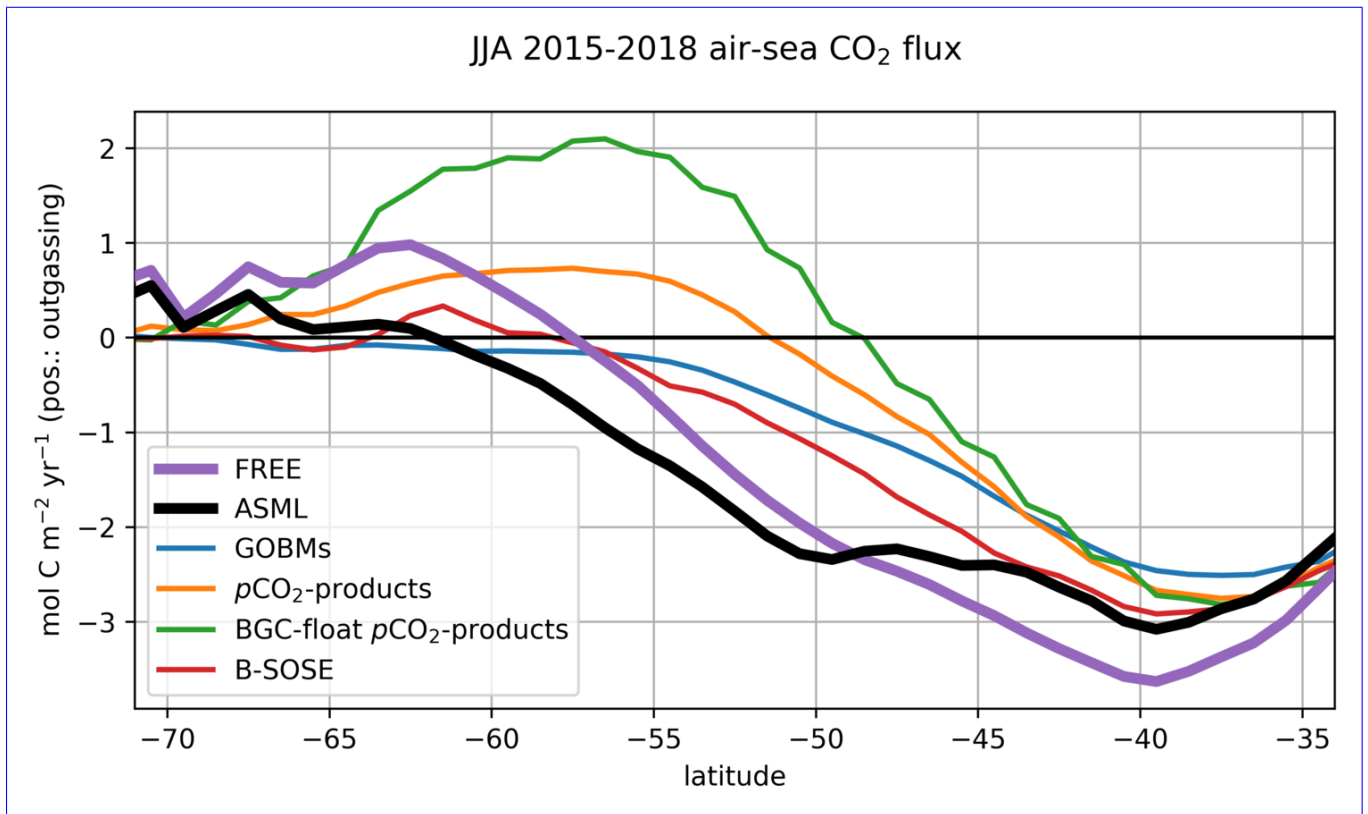


Figure A14. Zonally averaged winter (JJA) air-sea CO₂ flux in FREE, ASML and previous estimates (Hauck et al., 2023a; Verdy and Mazloff, 2017).

925 **Text A1: Velocity field** A problem with deep equatorial vertical velocities is indicated by artifacts of the meridional overturning in ASML. Throughout the assimilation period, spurious, spatially limited and often deep overturning structures emerge, evolve through several months or years, and disappear in the tropical Indian, Pacific and Atlantic basin (not shown). Thereby, the surface overturning cell sometimes breaks apart where it should extend over the equator, exposing the bottom cell to the surface. One possible cause is the effect of data assimilation on the eddy parameterisation (Gent and Mewilliams, 1990). The parameterised eddy activity is relevant for the dynamics in the deep ocean, and corrupting it can have a negative impact on the large-scale oceanic circulation, as described in Sidorenko (2004, Chapter 5.5 onwards) for a previous version of the ocean model FESOM.

930

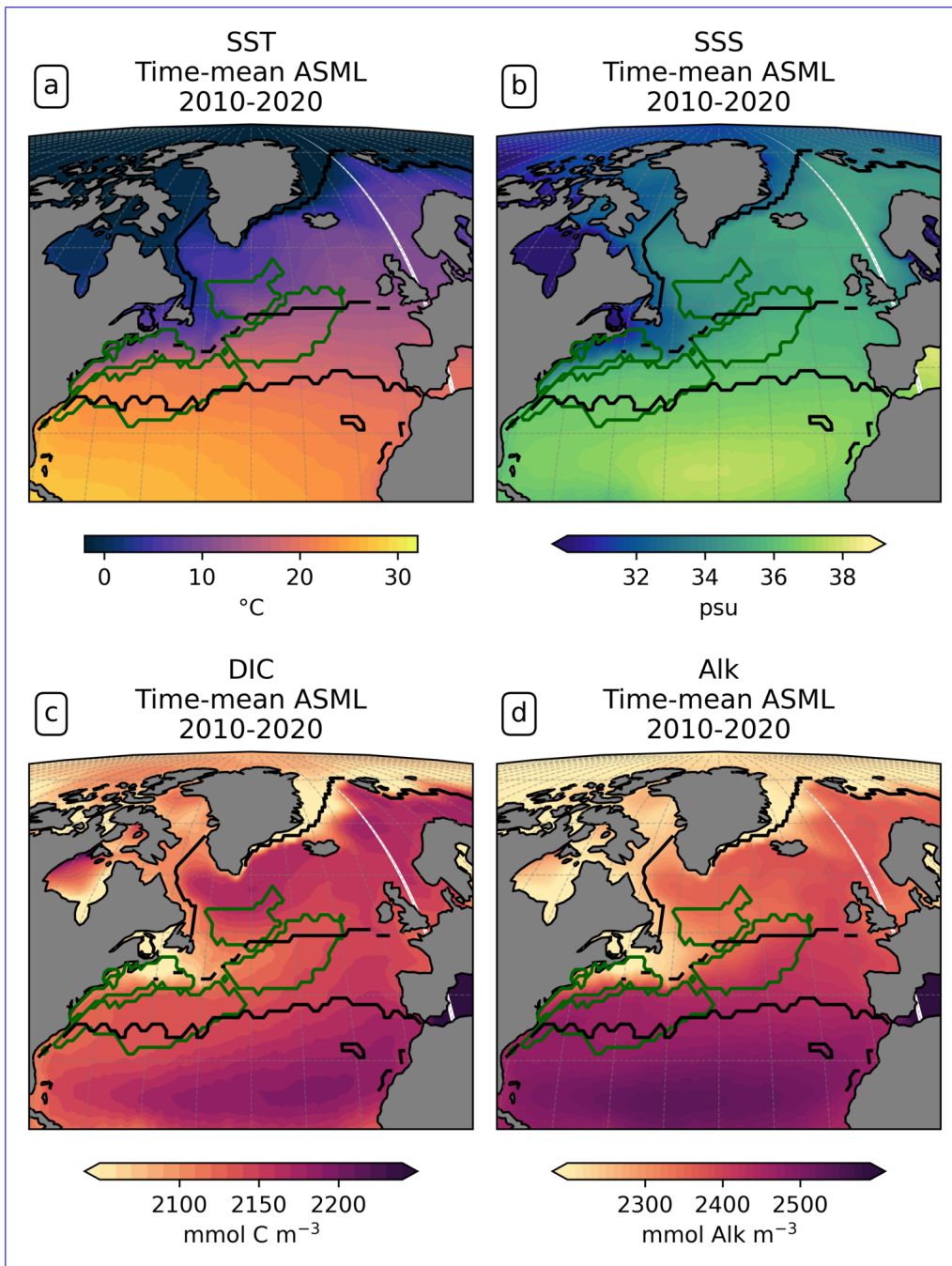


Figure A15. North Atlantic time-mean sea surface in ASML, (a) temperature, (b) salinity, (c) DIC and (d) alkalinity.

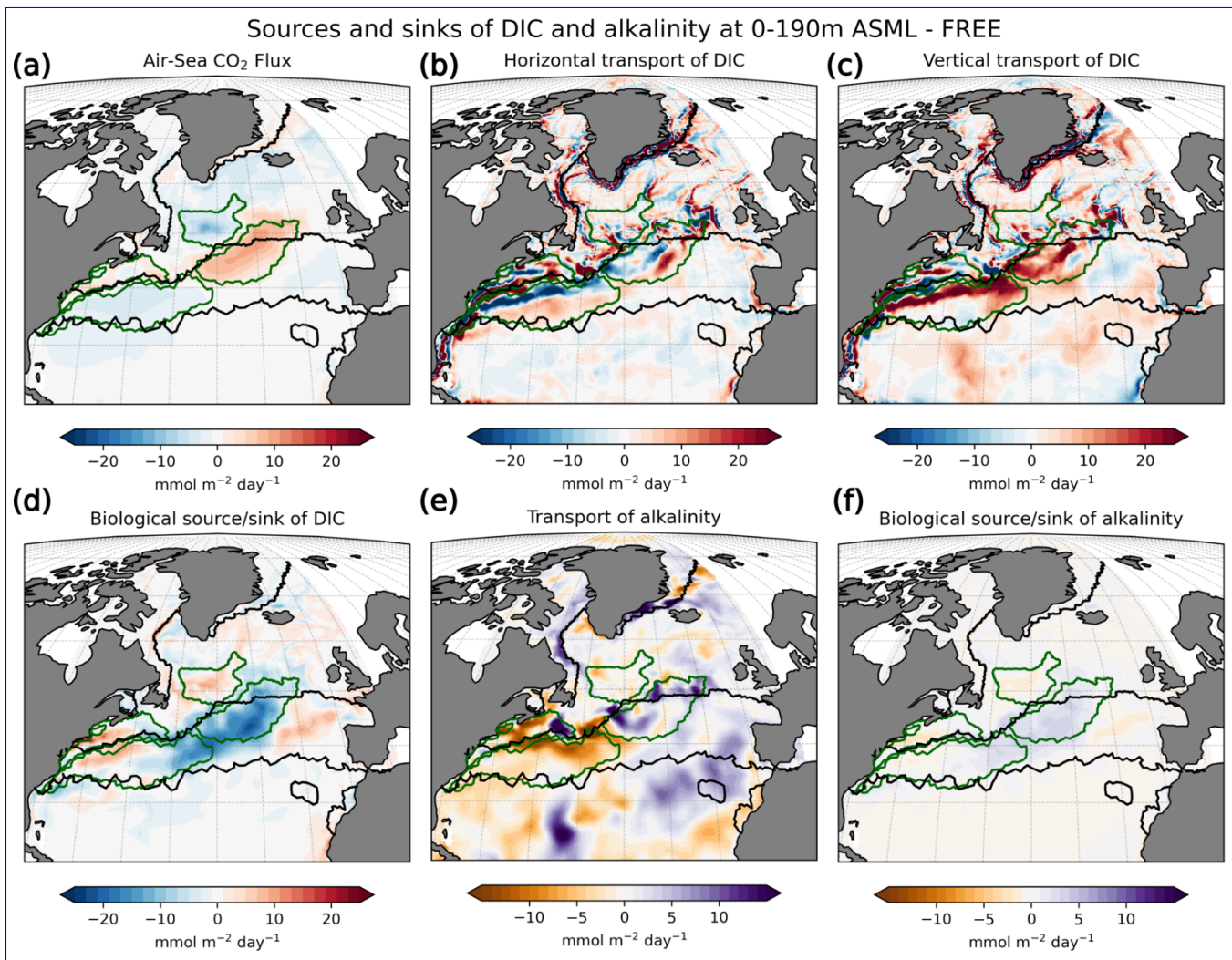


Figure A16. The difference (ASML-FREE) of source and sink terms for the ocean's DIC and alkalinity content integrated over 0-190 m in the North Atlantic in the year 2020. Transport terms include advection and diffusion of DIC and alkalinity. Biological terms for DIC are the sum of: photosynthesis, respiration, remineralization of dissolved organic carbon, and formation and dissolution of calcite. Biological terms for alkalinity are the sum of: nitrogen assimilation and remineralization, and formation and dissolution of calcite.

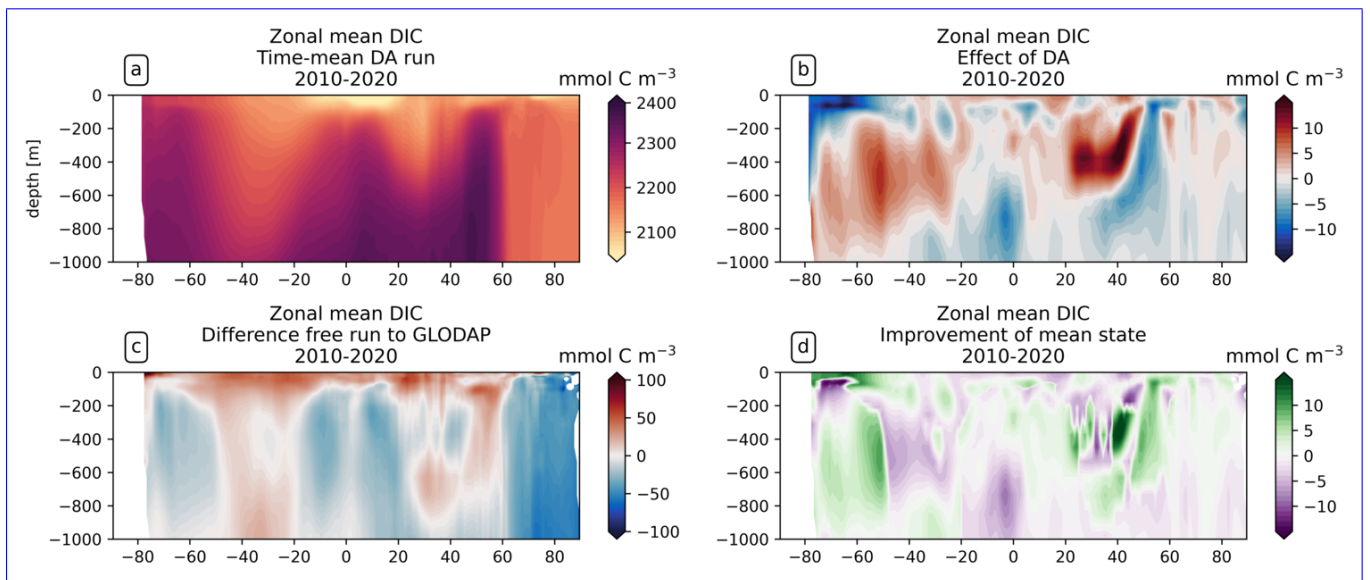


Figure A17. Zonally averaged DIC, (a) time-mean in ASML, (b) difference ASML-FREE, (c) difference FREE-OBS compared to the GLODAP climatology for DIC (Lauvset et al., 2016) and (d) improvement respective to the GLODAP climatology.

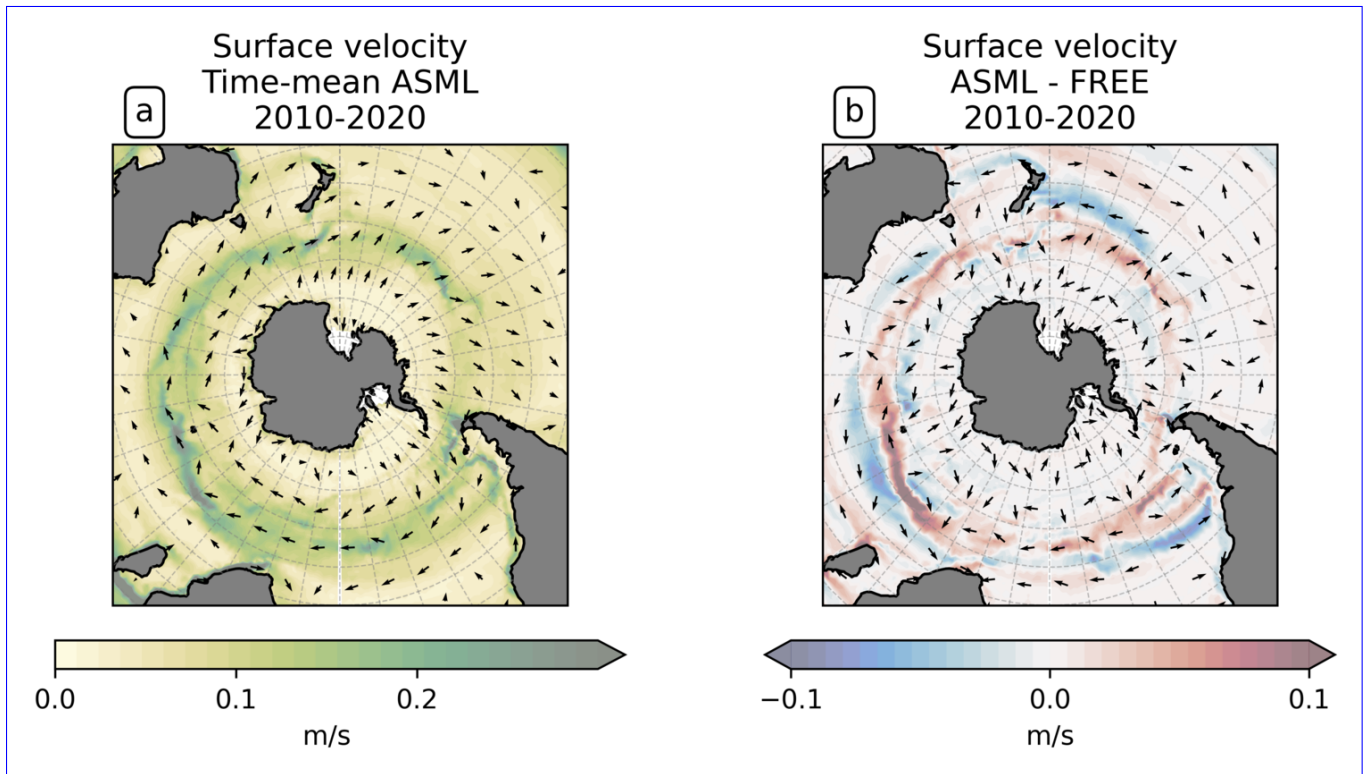


Figure A18. Surface velocities in the Southern Ocean, (a) time-mean in ASML and (b) difference ASML-FREE.

Author contributions. JH and LN conceptualized the research idea and provided supervision of the work. FB worked on the code for the model binding, for which LN provided supervision, and performed formal analysis of the data and figure production. FB prepared the initial paper draft with conceptual inputs from all authors. All authors contributed to the review and editing of the final manuscript.

Competing interests. The authors declare that they have no conflict of interest.

935 *Acknowledgements.* We acknowledge the Global Carbon Project, which is responsible for the Global Carbon Budget and ~~RECCAP~~RECCAP2 and we thank the ocean modeling and fCO₂-mapping groups for producing and making available their model and fCO₂-product output; in particular Cara Nissen for providing the files. Further, we thank Longjiang Mu who provided code for a PDAF-model binding within the FESOM model family in order to modify it for our study. At last, we acknowledge the use of DeepL Free (DeepL SE, <https://www.deepl.com/translator>) for translations and of ChatGPT 3.5 (Open AI, <https://chat.openai.com>) to provide rewording suggestions
940 for the text.

FB has received funding from the AWI INSPIRES programme, and JH from the Helmholtz Young Investigator Group Marine Carbon and Ecosystem Feedbacks in the Earth System (MarESys, Grant VHNG-1301), and from the European Research Council Starting Grant ERC2022-STG OceanPeak (Grant 101077209). The work reflects only the authors' view; the European Commission and their executive agency are not responsible for any use that may be made of the information the work contains.

- Bakker, D. C. E., Pfeil, B., Landa, C. S., Metzl, N., O'Brien, K. M., Olsen, A., Smith, K., Cosca, C., Harasawa, S., Jones, S. D., Nakaoka, S., Nojiri, Y., Schuster, U., Steinhoff, T., Sweeney, C., Takahashi, T., Tilbrook, B., Wada, C., Wanninkhof, R., Alin, S. R., Balestrini, C. F., Barbero, L., Bates, N. R., Bianchi, A. A., Bonou, F., Boutin, J., Bozec, Y., Burger, E. F., Cai, W.-J., Castle, R. D., Chen, L., Chierici, M., Currie, K., Evans, W., Featherstone, C., Feely, R. A., Fransson, A., Goyet, C., Greenwood, N., Gregor, L., Hankin, S., Hardman-Mountford, N. J., Harlay, J., Hauck, J., Hoppema, M., Humphreys, M. P., Hunt, C. W., Huss, B., Ibáñez, J. S. P., Johannessen, T., Keeling, R., Kitidis, V., Körtzinger, A., Kozyr, A., Krasakopoulou, E., Kuwata, A., Landschützer, P., Lauvset, S. K., Lefèvre, N., Lo Monaco, C., Manke, A., Mathis, J. T., Merlivat, L., Millero, F. J., Monteiro, P. M. S., Munro, D. R., Murata, A., Newberger, T., Omar, A. M., Ono, T., Paterson, K., Pearce, D., Pierrot, D., Robbins, L. L., Saito, S., Salisbury, J., Schlitzer, R., Schneider, B., Schweitzer, R., Sieger, R., Skjelvan, I., Sullivan, K. F., Sutherland, S. C., Sutton, A. J., Tadokoro, K., Telszewski, M., Tuma, M., van Heuven, S. M. A. C., Vandemark, D., Ward, B., Watson, A. J., and Xu, S.: A multi-decade record of high-quality $f\text{CO}_2$ data in version 3 of the Surface Ocean CO_2 Atlas (SOCAT), *Earth System Science Data*, 8, 383–413, <https://doi.org/10.5194/essd-8-383-2016>, 2016.
- Bakker, D. C. E., Alin, S. R., Bates, N., Becker, M., Feely, R. A., Gkritzalis, T., Jones, S. D., Kozyr, A., Lauvset, S. K., Metzl, N., Munro, D. R., Nakaoka, S.-i., Nojiri, Y., O'Brien, K. M., Olsen, A., Pierrot, D., Rehder, G., Steinhoff, T., Sutton, A. J., Sweeney, C., Tilbrook, B., Wada, C., Wanninkhof, R., Akl, J., Barbero, L., Beatty, C. M., Berghoff, C. F., Bittig, H. C., Bott, R., Burger, E. F., Cai, W.-J., Castaño Primo, R., Corredor, J. E., Cronin, M., De Carlo, E. H., DeGrandpre, M. D., Dietrich, C., Drennan, W. M., Emerson, S. R., Enochs, I. C., Enyo, K., Epherra, L., Evans, W., Fiedler, B., Fontela, M., Frangoulis, C., Gehrung, M., Giannoudi, L., Glockzin, M., Hales, B., Howden, S. D., Ibáñez, J. S. P., Kamb, L., Körtzinger, A., Lefèvre, N., Lo Monaco, C., Lutz, V. A., Macovei, V. A., Maenner Jones, S., Manalang, D., Manzello, D. P., Metzl, N., Mickett, J., Millero, F. J., Monacci, N. M., Morell, J. M., Musielewicz, S., Neill, C., Newberger, T., Newton, J., Noakes, S., Ólafsdóttir, S. R., Ono, T., Osborne, J., Padín, X. A., Paulsen, M., Perivoliotis, L., Petersen, W., Petihakis, G., Plueddemann, A. J., Rodriguez, C., Rutgersson, A., Sabine, C. L., Salisbury, J. E., Schlitzer, R., Skjelvan, I., Stamatakis, N., Sullivan, K. F., Sutherland, S. C., T'Jampens, M., Tadokoro, K., Tanhua, T., Telszewski, M., Theetaert, H., Tomlinson, M., Vandemark, D., Velo, A., Voynova, Y. G., Weller, R. A., Whitehead, C., and Wimart-Rousseau, C.: Surface Ocean CO_2 Atlas Database Version 2023 (SOCATv2023) (NCEI Accession 0278913), <https://doi.org/10.25921/r7xa-bt92>, 2023.
- Ballantyne, A. P., Alden, C. B., Miller, J. B., Tans, P. P., and White, J. W. C.: Increase in observed net carbon dioxide uptake by land and oceans during the past 50 years, *Nature*, 488, 70–72, <https://doi.org/10.1038/nature11299>, 2012.
- Bernardello, R., Sicardi, V., Lapin, V., Ortega, P., Ruprich-Robert, Y., Tourigny, E., and Ferrer, E.: Ocean biogeochemical reconstructions to estimate historical ocean CO_2 uptake, *Earth System Dynamics*, 15, 1255–1275, <https://doi.org/10.5194/esd-15-1255-2024>, 2024.
- Boutin, J., Vergely, J.-L., Reul, N., Catany, R., Koehler, J., Martin, A., Rouffi, F., Arias, M., Chakroun, M., Corato, G., et al.: ESA Sea Surface Salinity Climate Change Initiative (Sea_Surface_Salinity_cci): Weekly and Monthly Sea Surface Salinity Product, v03.21, from 2010 to 2020, NERC EDS Centre for Environmental Data Analysis, <http://dx.doi.org/10.5285/5920a2c77e3c45339477acd31ce62c3c>, 2021.
- Brix, H., Menemenlis, D., Hill, C., Dutkiewicz, S., Jahn, O., Wang, D., Bowman, K., and Zhang, H.: Using Green's Functions to initialize and adjust a global, eddy ocean biogeochemistry general circulation model, *Ocean Modelling*, 95, 1–14, <https://doi.org/10.1016/j.ocemod.2015.07.008>, 2015.
- Buchanan, P. J., Matear, R. J., Chase, Z., Phipps, S. J., and Bindoff, N. L.: Dynamic Biological Functioning Important for Simulating and Stabilizing Ocean Biogeochemistry, *Global Biogeochemical Cycles*, 32, 565–593, <https://doi.org/10.1002/2017GB005753>, 2018.

- Bunsen, F., Nissen, C., and Hauck, J.: The Impact of Recent Climate Change on the Global Ocean Carbon Sink, *Geophysical Research Letters*, 51, e2023GL107 030, <https://doi.org/10.1029/2023GL107030>, 2024.
- Bushinsky, S. M., Landschützer, P., Rödenbeck, C., Gray, A. R., Baker, D., Mazloff, M. R., Resplandy, L., Johnson, K. S., and Sarmiento, J. L.: Reassessing Southern Ocean Air-Sea CO₂ Flux Estimates With the Addition of Biogeochemical Float Observations, *Global Biogeochemical Cycles*, 33, 1370–1388, <https://doi.org/10.1029/2019GB006176>, 2019.
- 985 Cao, L., Eby, M., Ridgwell, A., Caldeira, K., Archer, D., Ishida, A., Joos, F., Matsumoto, K., Mikolajewicz, U., Mouchet, A., Orr, J. C., Plattner, G.-K., Schlitzer, R., Tokos, K., Totterdell, I., Tschumi, T., Yamanaka, Y., and Yool, A.: The role of ocean transport in the uptake of anthropogenic CO₂, *Biogeosciences*, 6, 375–390, <https://doi.org/10.5194/bg-6-375-2009>, 2009.
- Carroll, D., Menemenlis, D., Adkins, J. F., Bowman, K. W., Brix, H., Dutkiewicz, S., Fenty, I., Gierach, M. M., Hill, C., Jahn, O., Landschützer, P., Lauderdale, J. M., Liu, J., Manizza, M., Naviaux, J. D., Rödenbeck, C., Schimel, D. S., Van der Stocken, T., and Zhang, H.: The ECCO-Darwin Data-Assimilative Global Ocean Biogeochemistry Model: Estimates of Seasonal to Multidecadal Surface Ocean pCO₂ and Air-Sea CO₂ Flux, *Journal of Advances in Modeling Earth Systems*, 12, e2019MS001 888, <https://doi.org/10.1029/2019MS001888>, 2020.
- 990 Chapman, C. C., Lea, M.-A., Meyer, A., Sallée, J.-B., and Hindell, M.: Defining Southern Ocean fronts and their influence on biological and physical processes in a changing climate, *Nature Climate Change*, 10, 209–219, <https://doi.org/10.1038/s41558-020-0705-4>, 2020.
- Ciavatta, S., Kay, S., Saux-Picart, S., Butenschön, M., and Allen, J. I.: Decadal reanalysis of biogeochemical indicators and fluxes in the North West European shelf-sea ecosystem, *Journal of Geophysical Research: Oceans*, 121, 1824–1845, <https://doi.org/10.1002/2015JC011496>, 2016.
- Ciavatta, S., Brewin, R. J. W., Skákala, J., Polimene, L., de Mora, L., Artioli, Y., and Allen, J. I.: Assimilation of Ocean-Color Plankton Functional Types to Improve Marine Ecosystem Simulations, *Journal of Geophysical Research: Oceans*, 123, 834–854, <https://doi.org/10.1002/2017JC013490>, 2018.
- 1000 CMEMS: Operational Sea Surface Temperature and Ice Analysis (OSTIA), <https://doi.org/10.48670/moi-00165>, 2023.
- Crisp, D., Dolman, H., Tanhua, T., McKinley, G. A., Hauck, J., Bastos, A., Sitch, S., Eggleston, S., and Aich, V.: How Well Do We Understand the Land-Ocean-Atmosphere Carbon Cycle?, *Reviews of Geophysics*, 60, e2021RG000 736, <https://doi.org/10.1029/2021RG000736>, 2022.
- 1005 Danilov, S., Sidorenko, D., Wang, Q., and Jung, T.: The Finite-volume Sea ice–Ocean Model (FESOM2), *Geoscientific Model Development*, 10, 765–789, <https://doi.org/10.5194/gmd-10-765-2017>, 2017.
- Davila, X., Gebbie, G., Brakstad, A., Lauvset, S. K., McDonagh, E. L., Schwinger, J., and Olsen, A.: How Is the Ocean Anthropogenic Carbon Reservoir Filled?, *Global Biogeochemical Cycles*, 36, e2021GB007 055, <https://doi.org/10.1029/2021GB007055>, 2022.
- 1010 de Boyer Montégut, C., Madec, G., Fischer, A. S., Lazar, A., and Iudicone, D.: Mixed layer depth over the global ocean: An examination of profile data and a profile-based climatology, *Journal of Geophysical Research: Oceans*, 109, <https://doi.org/https://doi.org/10.1029/2004JC002378>, 2004.
- Denvil-Sommer, A., Gehlen, M., and Vrac, M.: Observation system simulation experiments in the Atlantic Ocean for enhanced surface ocean pCO₂ reconstructions, *Ocean Science*, 17, 1011–1030, <https://doi.org/10.5194/os-17-1011-2021>, 2021.
- 1015 DeVries, T.: The Ocean Carbon Cycle, *Annual Review of Environment and Resources*, 47, 317–341, <https://doi.org/10.1146/annurev-environ-120920-111307>, 2022.
- DeVries, T., Holzer, M., and Primeau, F.: Recent increase in oceanic carbon uptake driven by weaker upper-ocean overturning, *Nature*, 542, 215–218, <https://doi.org/10.1038/nature21068>, 2017.

- DeVries, T., Yamamoto, K., Wanninkhof, R., Gruber, N., Hauck, J., Müller, J. D., Bopp, L., Carroll, D., Carter, B., Chau, T.-T.-T., Doney, S. C., Gehlen, M., Gloege, L., Gregor, L., Henson, S., Kim, J. H., Iida, Y., Ilyina, T., Landschützer, P., Le Quéré, C., Munro, D., Nissen, C., Patara, L., Pérez, F. F., Resplandy, L., Rodgers, K. B., Schwinger, J., Séférian, R., Sicardi, V., Terhaar, J., Triñanes, J., Tsujino, H., Watson, A., Yasunaka, S., and Zeng, J.: Magnitude, Trends, and Variability of the Global Ocean Carbon Sink From 1985 to 2018, *Global Biogeochemical Cycles*, 37, e2023GB007780, <https://doi.org/10.1029/2023GB007780>, 2023.
- 1020 Doney, S. C., Lindsay, K., Caldeira, K., Campin, J.-M., Drange, H., Dutay, J.-C., Follows, M., Gao, Y., Gnanadesikan, A., Gruber, N., Ishida, A., Joos, F., Madec, G., Maier-Reimer, E., Marshall, J. C., Matear, R. J., Monfray, P., Mouchet, A., Najjar, R., Orr, J. C., Plattner, G.-K., Sarmiento, J., Schlitzer, R., Slater, R., Totterdell, I. J., Weirig, M.-F., Yamanaka, Y., and Yool, A.: Evaluating global ocean carbon models: The importance of realistic physics, *Global Biogeochemical Cycles*, 18, <https://doi.org/10.1029/2003GB002150>, 2004.
- 1025 Doney, S. C., Lima, I., Feely, R. A., Glover, D. M., Lindsay, K., Mahowald, N., Moore, J. K., and Wanninkhof, R.: Mechanisms governing interannual variability in upper-ocean inorganic carbon system and air–sea CO₂ fluxes: Physical climate and atmospheric dust, *Deep Sea Research Part II: Topical Studies in Oceanography*, 56, 640–655, <https://doi.org/10.1016/j.dsr2.2008.12.006>, 2009.
- 1030 Donlon, C., Martin, M., Stark, J., Roberts-Jones, J., Fiedler, E., and Wimmer, W.: The Operational Sea Surface Temperature and Sea Ice Analysis (OSTIA) system, *Remote Sensing of the Environment*, <https://doi.org/10.1016/j.rse.2010.10.017>, 2012.
- Eggleston, E. S., Sabine, C. L., and Morel, F. M. M.: Revelle revisited: Buffer factors that quantify the response of ocean chemistry to changes in DIC and alkalinity, *Global Biogeochemical Cycles*, 24, <https://doi.org/10.1029/2008GB003407>, 2010.
- 1035 EUMETSAT: OSI SAF Global medium resolution sea ice concentration climate data record 2002–2020 (v3.0), Ocean and Sea Ice Satellite Application Facility, https://doi.org/10.15770/EUM_SAF_OSI_0015, 2022.
- Evensen, G.: The Ensemble Kalman Filter: Theoretical Formulation and Practical Implementation, *Ocean Dynamics*, 53, 343–367, <https://doi.org/10.1007/s10236-003-0036-9>, 2003.
- Fay, A. R. and McKinley, G. A.: Global open-ocean biomes: mean and temporal variability, *Earth System Science Data*, 6, 273–284, <https://doi.org/10.5194/essd-6-273-2014>, 2014.
- 1040 Fennel, K., Mattern, J. P., Doney, S. C., Bopp, L., Moore, A. M., Wang, B., and Yu, L.: Ocean biogeochemical modelling, *Nature Reviews Methods Primers*, 2, 1–21, <https://doi.org/10.1038/s43586-022-00154-2>, 2022.
- Ford, D. and Barciela, R.: Global marine biogeochemical reanalyses assimilating two different sets of merged ocean colour products, *Remote Sensing of Environment*, 203, 40–54, <https://doi.org/10.1016/j.rse.2017.03.040>, *earth Observation of Essential Climate Variables*, 2017.
- 1045 Fransner, F., Counillon, F., Bethke, I., Tjiputra, J., Samuelsen, A., Nummelin, A., and Olsen, A.: Ocean Biogeochemical Predictions—Initialization and Limits of Predictability, *Frontiers in Marine Science*, 7, 508 048, <https://doi.org/10.3389/fmars.2020.00386>, 2020.
- Friedlingstein, P., O’Sullivan, M., Jones, M. W., Andrew, R. M., Bakker, D. C. E., Hauck, J., Landschützer, P., Le Quéré, C., Luijkx, I. T., Peters, G. P., Peters, W., Pongratz, J., Schwingshackl, C., Sitch, S., Canadell, J. G., Ciais, P., Jackson, R. B., Alin, S. R., Anthoni, P., Barbero, L., Bates, N. R., Becker, M., Bellouin, N., Decharme, B., Bopp, L., Brasika, I. B. M., Cadule, P., Chamberlain, M. A., Chandra, N., Chau, T.-T.-T., Chevallier, F., Chini, L. P., Cronin, M., Dou, X., Enyo, K., Evans, W., Falk, S., Feely, R. A., Feng, L., Ford, D. J., Gasser, T., Ghattas, J., Gkritzalis, T., Grassi, G., Gregor, L., Gruber, N., Gürses, Ö., Harris, I., Hefner, M., Heinke, J., Houghton, R. A., Hurtt, G. C., Iida, Y., Ilyina, T., Jacobson, A. R., Jain, A., Jarníková, T., Jersild, A., Jiang, F., Jin, Z., Joos, F., Kato, E., Keeling, R. F., Kennedy, D., Klein Goldewijk, K., Knauer, J., Korsbakken, J. I., Körtzinger, A., Lan, X., Lefèvre, N., Li, H., Liu, J., Liu, Z., Ma, L., Marland, G., Mayot, N., McGuire, P. C., McKinley, G. A., Meyer, G., Morgan, E. J., Munro, D. R., Nakaoka, S.-I., Niwa, Y., O’Brien, K. M., Olsen, A., Omar, A. M., Ono, T., Paulsen, M., Pierrot, D., Pockock, K., Poulter, B., Powis, C. M., Rehder, G., Resplandy, L., Robertson, E., Rödenbeck, C., Rosan, T. M., Schwinger, J., Séférian, R., Smallman, T. L., Smith, S. M., Sospedra-Alfonso, R., Sun, Q.,
- 1055

- Sutton, A. J., Sweeney, C., Takao, S., Tans, P. P., Tian, H., Tilbrook, B., Tsujino, H., Tubiello, F., van der Werf, G. R., van Ooijen, E., Wanninkhof, R., Watanabe, M., Wimart-Rousseau, C., Yang, D., Yang, X., Yuan, W., Yue, X., Zaehle, S., Zeng, J., and Zheng, B.: Global Carbon Budget 2023, *Earth System Science Data*, 15, 5301–5369, <https://doi.org/10.5194/essd-15-5301-2023>, 2023.
- 1060 Gaspari, G. and Cohn, S. E.: Construction of correlation functions in two and three dimensions, *Quarterly Journal of the Royal Meteorological Society*, 125, 723–757, <https://doi.org/10.1002/qj.49712555417>, 1999.
- Gasparin, F., Cravatte, S., Greiner, E., Perruche, C., Hamon, M., Van Gennip, S., and Lellouche, J.-M.: Excessive productivity and heat content in tropical Pacific analyses: Disentangling the effects of in situ and altimetry assimilation, *Ocean Modelling*, 160, 101768, <https://doi.org/https://doi.org/10.1016/j.ocemod.2021.101768>, 2021.
- 1065 Gent, P. R. and McWilliams, J. C.: Isopycnal Mixing in Ocean Circulation Models, *Journal of Physical Oceanography*, 20, 150–155, [https://doi.org/10.1175/1520-0485\(1990\)020<0150:IMIOCM>2.0.CO;2](https://doi.org/10.1175/1520-0485(1990)020<0150:IMIOCM>2.0.CO;2), 1990.
- Gerber, M., Joos, F., Vázquez-Rodríguez, M., Touratier, F., and Goyet, C.: Regional air-sea fluxes of anthropogenic carbon inferred with an Ensemble Kalman Filter, *Global Biogeochemical Cycles*, 23, <https://doi.org/10.1029/2008GB003247>, 2009.
- Gloege, L., McKinley, G. A., Landschützer, P., Fay, A. R., Frölicher, T. L., Fyfe, J. C., Ilyina, T., Jones, S., Lovenduski, N. S., Rodgers, K. B., Schlunegger, S., and Takano, Y.: Quantifying Errors in Observationally Based Estimates of Ocean Carbon Sink Variability, *Global Biogeochemical Cycles*, 35, e2020GB006788, <https://doi.org/10.1029/2020GB006788>, 2021.
- 1070 Good, S., Fiedler, E., Mao, C., Martin, M., Maycock, A., Reid, R., Roberts-Jones, J., Searle, T., Waters, J., While, J., and Worsfold, M.: The Current Configuration of the OSTIA System for Operational Production of Foundation Sea Surface Temperature and Ice Concentration Analyses, *Remote Sens.*, 12, 720, <https://doi.org/10.3390/rs12040720>, 2020.
- 1075 Good, S. A., Martin, M. J., and Rayner, N. A.: EN4: Quality Controlled Ocean Temperature and Salinity Profiles and Monthly Objective Analyses with Uncertainty Estimates, *Journal of Geophysical Research: Oceans*, <https://doi.org/10.1002/2013JC009067>, 2013.
- Gray, A. R., Johnson, K. S., Bushinsky, S. M., Riser, S. C., Russell, J. L., Talley, L. D., Wanninkhof, R., Williams, N. L., and Sarmiento, J. L.: Autonomous Biogeochemical Floats Detect Significant Carbon Dioxide Outgassing in the High-Latitude Southern Ocean, *Geophysical Research Letters*, 45, 9049–9057, <https://doi.org/10.1029/2018GL078013>, 2018.
- 1080 Gruber, N., Gloor, M., Fletcher, S. E. M., Doney, S. C., Dutkiewicz, S., Follows, M. J., Gerber, M., Jacobson, A. R., Joos, F., Lindsay, K., Menemenlis, D., Mouchet, A., Müller, S. A., Sarmiento, J. L., and Takahashi, T.: Oceanic sources, sinks, and transport of atmospheric CO₂, *Global Biogeochemical Cycles*, 23, <https://doi.org/10.1029/2008GB003349>, 2009.
- Gürses, O., Oziel, L., Karakuş, O., Sidorenko, D., Völker, C., Ye, Y., Zeising, M., Butzin, M., and Hauck, J.: Ocean biogeochemistry in the coupled ocean–sea ice–biogeochemistry model FESOM2.1–REcoM3, *Geoscientific Model Development*, 16, 4883–4936, <https://doi.org/10.5194/gmd-16-4883-2023>, 2023.
- 1085 Hauck, J., Völker, C., Wang, T., Hoppema, M., Losch, M., and Wolf-Gladrow, D. A.: Seasonally Different Carbon Flux Changes in the Southern Ocean in Response to the Southern Annular Mode, *Global Biogeochemical Cycles*, 27, 1236–1245, <https://doi.org/10.1002/2013GB004600>, 2013.
- Hauck, J., Zeising, M., Le Quéré, C., Gruber, N., Bakker, D. C. E., Bopp, L., Chau, T. T. T., Gürses, Ö., Ilyina, T., Landschützer, P., Lenton, A., Resplandy, L., Rödenbeck, C., Schwinger, J., and Séférian, R.: Consistency and Challenges in the Ocean Carbon Sink Estimate for the Global Carbon Budget, *Frontiers in Marine Science*, 7, 571720, <https://doi.org/10.3389/fmars.2020.571720>, 2020.
- 1090 Hauck, J., Gregor, L., Nissen, C., Patara, L., Hague, M., Mongwe, P., Bushinsky, S., Doney, S. C., Gruber, N., Le Quéré, C., Manizza, M., Mazloff, M., Monteiro, P. M. S., and Terhaar, J.: The Southern Ocean Carbon Cycle 1985–2018: Mean, Seasonal Cycle, Trends, and Storage, *Global Biogeochemical Cycles*, 37, e2023GB007848, <https://doi.org/10.1029/2023GB007848>, 2023a.

- 1095 Hauck, J., Nissen, C., Landschützer, P., Rödenbeck, C., Bushinsky, S., and Olsen, A.: Sparse observations induce large biases in estimates of the global ocean CO₂ sink: an ocean model subsampling experiment, *Philosophical Transactions of the Royal Society A*, 381, 20220063, <https://doi.org/10.1098/rsta.2022.0063>, 2023b.
- Hemmings, J. C. P., Barciela, R. M., and Bell, M. J.: Ocean Color Data Assimilation with Material Conservation for Improving Model Estimates of Air-Sea CO₂ Flux, *Journal of Marine Research*, 66, 87–126, <https://doi.org/10.1357/002224008784815739>, 2008.
- 1100 Hohn, S.: Coupling and decoupling of biogeochemical cycles in marine ecosystems, Ph.D. thesis, University of Bremen, 2008.
- Johnson, K. S., Plant, J. N., Coletti, L. J., Jannasch, H. W., Sakamoto, C. M., Riser, S. C., Swift, D. D., Williams, N. L., Boss, E., Haëntjens, N., Talley, L. D., and Sarmiento, J. L.: Biogeochemical sensor performance in the SOCCOM profiling float array, *Journal of Geophysical Research: Oceans*, 122, 6416–6436, <https://doi.org/10.1002/2017JC012838>, 2017.
- Johnson, R., Strutton, P. G., Wright, S. W., McMinn, A., and Meiners, K. M.: Three Improved Satellite Chlorophyll Algorithms for the Southern Ocean, *Journal of Geophysical Research: Oceans*, 118, 3694–3703, <https://doi.org/10.1002/jgrc.20270>, 2013.
- 1105 Jones, S. D., Le Quéré, C., and Rödenbeck, C.: Autocorrelation characteristics of surface ocean pCO₂ and air-sea CO₂ fluxes, *Global Biogeochemical Cycles*, 26, <https://doi.org/10.1029/2010GB004017>, 2012.
- Joos, F. and Spahni, R.: Rates of change in natural and anthropogenic radiative forcing over the past 20,000 years, *Proceedings of the National Academy of Sciences*, 105, 1425–1430, <https://doi.org/10.1073/pnas.0707386105>, 2008.
- 1110 Karakuş, O., Völker, C., Iversen, M., Hagen, W., Wolf-Gladrow, D., Fach, B., and Hauck, J.: Modeling the Impact of Macrozooplankton on Carbon Export Production in the Southern Ocean, *Journal of Geophysical Research: Oceans*, 126, e2021JC017315, <https://doi.org/10.1029/2021JC017315>, 2021.
- Keppler, L. and Landschützer, P.: Regional wind variability modulates the Southern Ocean carbon sink, *Scientific reports*, 9, 7384, <https://doi.org/10.1038/s41598-019-43826-y>, 2019.
- 1115 Kriest, I., Kähler, P., Koeve, W., Kvale, K., Sauerland, V., and Oschlies, A.: One size fits all? Calibrating an ocean biogeochemistry model for different circulations, *Biogeosciences*, 17, 3057–3082, <https://doi.org/10.5194/bg-17-3057-2020>, 2020.
- Large, W. G., McWilliams, J. C., and Doney, S. C.: Oceanic vertical mixing: A review and a model with a nonlocal boundary layer parameterization, *Reviews of Geophysics*, 32, 363–403, <https://doi.org/10.1029/94RG01872>, 1994.
- Laurindo, L. C., Mariano, A. J., and Lumpkin, R.: An improved near-surface velocity climatology for the global ocean from drifter observations, *Deep Sea Research Part I: Oceanographic Research Papers*, 124, 73–92, <https://doi.org/10.1016/j.dsr.2017.04.009>, 2017.
- 1120 Lauvset, S. K., Key, R. M., Olsen, A., van Heuven, S., Velo, A., Lin, X., Schirnack, C., Kozyr, A., Tanhua, T., Hoppema, M., Jutterström, S., Steinfeldt, R., Jeansson, E., Ishii, M., Perez, F. F., Suzuki, T., and Watelet, S.: A New Global Interior Ocean Mapped Climatology: The 1°x1° GLODAP Version 2, *Earth System Science Data*, 8, 325–340, <https://doi.org/10.5194/essd-8-325-2016>, 2016.
- 1125 Lauvset, S. K., Lange, N., Tanhua, T., Bittig, H. C., Olsen, A., Kozyr, A., Álvarez, M., Azetsu-Scott, K., Brown, P. J., Carter, B. R., Cotrim da Cunha, L., Hoppema, M., Humphreys, M. P., Ishii, M., Jeansson, E., Murata, A., Müller, J. D., Perez, F. F., Schirnack, C., Steinfeldt, R., Suzuki, T., Ulfsbo, A., Velo, A., Woosley, R. J., and Key, R.: The annual update GLODAPv2.2023: the global interior ocean biogeochemical data product, *Earth System Science Data Discussions*, 2024, 1–32, <https://doi.org/10.5194/essd-2023-468>, 2024a.
- 1130 Lauvset, S. K., Lange, N., Tanhua, T., Bittig, H. C., Olsen, A., Kozyr, A., Álvarez, M., Azetsu-Scott, K., Brown, P. J., Carter, B. R., Cotrim da Cunha, L., Hoppema, M., Humphreys, M. P., Ishii, M., Jeansson, E., Murata, A., Müller, J. D., Pérez, F. F., Schirnack, C., Steinfeldt, R., Suzuki, T., Ulfsbo, A., Velo, A., Woosley, R. J., and Key, R. M.: The annual update GLODAPv2.2023: the global interior ocean biogeochemical data product, *Earth System Science Data*, 16, 2047–2072, <https://doi.org/10.5194/essd-16-2047-2024>, 2024b.

- Le Quéré, C., Raupach, M. R., Canadell, J. G., Marland, G., Bopp, L., Ciais, P., Conway, T. J., Doney, S. C., Feely, R. A., Foster, P., Friedlingstein, P., Gurney, K., Houghton, R. A., House, J. I., Huntingford, C., Levy, P. E., Lomas, M. R., Majkut, J., Metzli, N., Ometto, J. P., Peters, G. P., Prentice, I. C., Randerson, J. T., Running, S. W., Sarmiento, J. L., Schuster, U., Sitch, S., Takahashi, T., Viovy, N., Van Der Werf, G. R., and Woodward, F. I.: Trends in the sources and sinks of carbon dioxide, *Nature Geoscience*, 2, 831–836, <https://doi.org/10.1038/ngeo689>, 2009.
- 1135 Lebehot, A. D., Halloran, P. R., Watson, A. J., McNeill, D., Ford, D. A., Landschützer, P., Lauvset, S. K., and Schuster, U.: Reconciling Observation and Model Trends in North Atlantic Surface CO₂, *Global Biogeochemical Cycles*, 33, 1204–1222, <https://doi.org/10.1029/2019GB006186>, 2019.
- 1140 Li, H., Ilyina, T., Müller, W. A., and Sienz, F.: Decadal predictions of the North Atlantic CO₂ uptake, *Nature Communications*, 7, 1–7, <https://doi.org/10.1038/ncomms11076>, 2016.
- Liao, E., Resplandy, L., Liu, J., and Bowman, K. W.: Amplification of the ocean carbon sink during El Niños: Role of poleward Ekman transport and influence on atmospheric CO₂, *Global Biogeochemical Cycles*, 34, <https://doi.org/10.1029/2020GB006574>, 2020.
- 1145 Long, M. C., Stephens, B. B., McKain, K., Sweeney, C., Keeling, R. F., Kort, E. A., Morgan, E. J., Bent, J. D., Chandra, N., Chevallier, F., Commane, R., Daube, B. C., Krummel, P. B., Loh, Z., Luijkx, I. T., Munro, D., Patra, P., Peters, W., Ramonet, M., Rödenbeck, C., Stavert, A., Tans, P., and Wofsy, S. C.: Strong Southern Ocean carbon uptake evident in airborne observations, *Science*, 374, 1275–1280, <https://doi.org/10.1126/science.abi4355>, 2021.
- Mamnun, N., Völker, C., Krumscheid, S., Vrekoussis, M., and Nerger, L.: Global Sensitivity Analysis of a One-Dimensional Ocean Biogeochemical Model, *Socio-Environmental Systems Modelling*, 5, 18 613, <https://doi.org/10.18174/sesmo.18613>, 2023.
- 1150 Mayot, N., Le Quéré, C., Rödenbeck, C., Bernardello, R., Bopp, L., Djeutchouang, L. M., Gehlen, M., Gregor, L., Gruber, N., Hauck, J., Iida, Y., Ilyina, T., Keeling, R. F., Landschützer, P., Manning, A. C., Patara, L., Resplandy, L., Schwinger, J., Séférian, R., Watson, A. J., Wright, R. M., and Zeng, J.: Climate-driven variability of the Southern Ocean CO₂ sink, *Philosophical Transactions of the Royal Society A: Mathematical, Physical and Engineering Sciences*, 381, 20220 055, <https://doi.org/10.1098/rsta.2022.0055>, 2023.
- 1155 Mayot, N., Buitenhuis, E. T., Wright, R. M., Hauck, J., Bakker, D. C. E., and Le Quéré, C.: Constraining the trend in the ocean CO₂ sink during 2000–2022, *Nature Communications*, 15, 1–11, <https://doi.org/10.1038/s41467-024-52641-7>, 2024.
- Menemenlis, D., Fukumori, I., and Lee, T.: Using Green's Functions to Calibrate an Ocean General Circulation Model, *Monthly Weather Review*, 133, 1224–1240, <https://doi.org/10.1175/MWR2912.1>, 2005.
- Mu, L., Nerger, L., Streffing, J., Tang, Q., Niraula, B., Zampieri, L., Loza, S. N., and Goessling, H. F.: Sea-Ice Forecasts With an Upgraded AWI Coupled Prediction System, *Journal of Advances in Modeling Earth Systems*, 14, e2022MS003 176, <https://doi.org/10.1029/2022MS003176>, 2022.
- 1160 Müller, J. D., Gruber, N., Carter, B., Feely, R., Ishii, M., Lange, N., Lauvset, S. K., Murata, A., Olsen, A., Pérez, F. F., Sabine, C., Tanhua, T., Wanninkhof, R., and Zhu, D.: Decadal Trends in the Oceanic Storage of Anthropogenic Carbon From 1994 to 2014, *AGU Advances*, 4, e2023AV000 875, <https://doi.org/10.1029/2023AV000875>, 2023.
- 1165 Nerger, L., Hiller, W., and Schröter, J.: PDAF - THE PARALLEL DATA ASSIMILATION FRAMEWORK: EXPERIENCES WITH KALMAN FILTERING, in: *Use of High Performance Computing in Meteorology*, pp. 63–83, WORLD SCIENTIFIC, Singapore, https://doi.org/10.1142/9789812701831_0006, 2005.
- Nerger, L., Janjić, T., Schröter, J., and Hiller, W.: A Unification of Ensemble Square Root Kalman Filters, *Monthly Weather Review*, 140, 2335–2345, <https://doi.org/10.1175/MWR-D-11-00102.1>, 2012.

- 1170 Nerger, L., Tang, Q., and Mu, L.: Efficient ensemble data assimilation for coupled models with the Parallel Data Assimilation Framework: example of AWI-CM (AWI-CM-PDAF 1.0), *Geoscientific Model Development*, 13, 4305–4321, <https://doi.org/10.5194/gmd-13-4305-2020>, 2020.
- Nerger, L., Tang, Q., and Mu, L.: The PDAF model binding for AWI-CM (AWI-CM-PDAF version 1.0 update 1), <https://doi.org/10.5281/zenodo.3822030>, 2024.
- 1175 Orr, J. C. and Epitalon, J.-M.: Improved routines to model the ocean carbonate system: mocsy 2.0, *Geoscientific Model Development*, 8, 485–499, <https://doi.org/10.5194/gmd-8-485-2015>, 2015.
- Orr, J. C., Najjar, R. G., Aumont, O., Bopp, L., Bullister, J. L., Danabasoglu, G., Doney, S. C., Dunne, J. P., Dutay, J.-C., Graven, H., Griffies, S. M., John, J. G., Joos, F., Levin, I., Lindsay, K., Matear, R. J., McKinley, G. A., Mouchet, A., Oschlies, A., Romanou, A., Schlitzer, R., Tagliabue, A., Tanhua, T., and Yool, A.: Biogeochemical protocols and diagnostics for the CMIP6 Ocean Model Intercomparison Project (OMIP), *Geoscientific Model Development*, 10, 2169–2199, <https://doi.org/10.5194/gmd-10-2169-2017>, 2017.
- 1180 Park, J.-Y., Stock, C. A., Yang, X., Dunne, J. P., Rosati, A., John, J., and Zhang, S.: Modeling global ocean biogeochemistry with physical data assimilation: a pragmatic solution to the equatorial instability, *Journal of Advances in modeling earth systems*, 10, 891–906, <https://doi.org/10.1002/2017MS001223>, 2018.
- Pérez, F. F., Becker, M., Goris, N., Gehlen, M., López-Mozos, M., Tjiputra, J., Olsen, A., Müller, J. D., Huertas, I. E., Chau, T.
- 1185 T. T., Cainzos, V., Velo, A., Benard, G., Hauck, J., Gruber, N., and Wanninkhof, R.: An Assessment of CO₂ Storage and Sea-Air Fluxes for the Atlantic Ocean and Mediterranean Sea Between 1985 and 2018, *Global Biogeochemical Cycles*, 38, e2023GB007862, <https://doi.org/10.1029/2023GB007862>, 2024.
- Peylin, P., Law, R. M., Gurney, K. R., Chevallier, F., Jacobson, A. R., Maki, T., Niwa, Y., Patra, P. K., Peters, W., Rayner, P. J., Rödenbeck, C., van der Laan-Luijkx, I. T., and Zhang, X.: Global atmospheric carbon budget: results from an ensemble of atmospheric CO₂ inversions, *Biogeosciences*, 10, 6699–6720, <https://doi.org/10.5194/bg-10-6699-2013>, 2013.
- 1190 Pham, D. T.: Stochastic Methods for Sequential Data Assimilation in Strongly Nonlinear Systems, *Monthly Weather Review*, 129, 1194 – 1207, [https://doi.org/10.1175/1520-0493\(2001\)129<1194:SMFSDA>2.0.CO;2](https://doi.org/10.1175/1520-0493(2001)129<1194:SMFSDA>2.0.CO;2), 2001.
- Pham, D. T., Verron, J., and Roubaud, M. C.: A singular evolutive extended Kalman filter for data assimilation in oceanography, *Journal of Marine Systems*, 16, 323–340, [https://doi.org/10.1016/S0924-7963\(97\)00109-7](https://doi.org/10.1016/S0924-7963(97)00109-7), 1998.
- 1195 Primeau, F. and Deleersnijder, E.: On the time to tracer equilibrium in the global ocean, *Ocean Science*, 5, 13–28, <https://doi.org/10.5194/os-5-13-2009>, 2009.
- Raghukumar, K., Edwards, C. A., Goebel, N. L., Broquet, G., Veneziani, M., Moore, A. M., and Zehr, J. P.: Impact of assimilating physical oceanographic data on modeled ecosystem dynamics in the California Current System, *Progress in Oceanography*, 138, 546–558, <https://doi.org/https://doi.org/10.1016/j.pocean.2015.01.004>, combining Modeling and Observations to Better Understand Marine Ecosystem Dynamics, 2015.
- 1200 Regnier, P., Resplandy, L., Najjar, R. G., and Ciais, P.: The land-to-ocean loops of the global carbon cycle, *Nature*, 603, 401–410, <https://doi.org/10.1038/s41586-021-04339-9>, 2022.
- Rödenbeck, C., Bakker, D. C. E., Gruber, N., Iida, Y., Jacobson, A. R., Jones, S., Landschützer, P., Metzl, N., Nakaoka, S., Olsen, A., Park, G.-H., Peylin, P., Rodgers, K. B., Sasse, T. P., Schuster, U., Shutler, J. D., Valsala, V., Wanninkhof, R., and Zeng, J.: Data-based estimates of the ocean carbon sink variability – first results of the Surface Ocean pCO₂ Mapping intercomparison (SOCOM), *Biogeosciences*, 12, 7251–7278, <https://doi.org/10.5194/bg-12-7251-2015>, 2015.
- 1205

- Sarmiento, J. L. and Gruber, N.: Carbon Cycle, in: *Ocean Biogeochemical Dynamics*, chap. 8, pp. 318–358, Princeton University Press, 2006.
- 1210 Sathyendranath, S., Jackson, T., Brockmann, C., Brotas, V., Calton, B., Chuprin, A., Clements, O., Cipollini, P., Danne, O., Dingle, J., Donlon, C., Grant, M., Groom, S., Krasemann, H., Lavender, S., Mazeran, C., Mélin, F., Müller, D., Steinmetz, F., Valente, A., Zühlke, M., Feldman, G., Franz, B., Frouin, R., Werdell, J., and Platt, T.: ESA Ocean Colour Climate Change Initiative (Ocean_Colour_cci): Version 5.0 Data, NERC EDS Centre for Environmental Data Analysis, <https://doi.org/10.5285/1dbe7a109c0244aaad713e078fd3059a>, 2021.
- 1215 Schartau, M., Engel, A., Schröter, J., Thoms, S., Völker, C., and Wolf-Gladrow, D.: Modelling carbon overconsumption and the formation of extracellular particulate organic carbon, *Biogeosciences*, 4, 433–454, <https://doi.org/10.5194/bg-4-433-2007>, 2007.
- Scholz, P., Sidorenko, D., Gurses, O., Danilov, S., Koldunov, N., Wang, Q., Sein, D., Smolentseva, M., Rakowsky, N., and Jung, T.: Assessment of the Finite-volume Sea ice-Ocean Model (FESOM2.0) – Part 1: Description of selected key model elements and comparison to its predecessor version, *Geoscientific Model Development*, 12, 4875–4899, <https://doi.org/10.5194/gmd-12-4875-2019>, 2019.
- 1220 Scholz, P., Sidorenko, D., Danilov, S., Wang, Q., Koldunov, N., Sein, D., and Jung, T.: Assessment of the Finite-Volume Sea ice–Ocean Model (FESOM2.0) – Part 2: Partial bottom cells, embedded sea ice and vertical mixing library CVMix, *Geoscientific Model Development*, 15, 335–363, <https://doi.org/10.5194/gmd-15-335-2022>, 2022.
- Schourup-Kristensen, V., Sidorenko, D., Wolf-Gladrow, D. A., and Völker, C.: A Skill Assessment of the Biogeochemical Model REcom2 coupled to the Finite Element Sea Ice Ocean Model (FESOM 1.3), *Geoscientific Model Development*, 7, 2769–2802, <https://doi.org/10.5194/gmd-7-2769-2014>, 2014.
- 1225 Sférian, R., Bopp, L., Gehlen, M., Swingedouw, D., Mignot, J., Guilyardi, E., and Servonnat, J.: Multiyear predictability of tropical marine productivity, *Proceedings of the National Academy of Sciences*, 111, 11 646–11 651, <https://doi.org/10.1073/pnas.1315855111>, 2014.
- Sidorenko, D.: The North Atlantic circulation derived from inverse models, Ph.D. thesis, University of Bremen, 2004.
- Spring, A., Dunkl, I., Li, H., Brovkin, V., and Ilyina, T.: Trivial improvements in predictive skill due to direct reconstruction of the global carbon cycle, *Earth System Dynamics*, 12, 1139–1167, <https://doi.org/10.5194/esd-12-1139-2021>, 2021.
- 1230 Stark, J., Donlon, C., Martin, M., and McCulloch, M.: OSTIA: An Operational, High Resolution, Real-Time, Global Sea Surface Temperature Analysis System, in: *Oceans 07 IEEE Aberdeen, Conference Proceedings. Marine Challenges: Coastline to Deep Sea*, IEEE, 2007.
- Sursham, D.: Improving the Simulation and Understanding of Biologically Driven Carbon Pumps in Marine Ecosystems using an Ensemble-Based Data Assimilation Method, Ph.D. thesis, University of Reading, 2018.
- 1235 Sutton, A. J., Williams, N. L., and Tilbrook, B.: Constraining Southern Ocean CO₂ Flux Uncertainty Using Uncrewed Surface Vehicle Observations, *Geophysical Research Letters*, 48, e2020GL091 748, <https://doi.org/10.1029/2020GL091748>, 2021.
- Takahashi, T., Olafsson, J., Goddard, J. G., Chipman, D. W., and Sutherland, S. C.: Seasonal variation of CO₂ and nutrients in the high-latitude surface oceans: A comparative study, *Global Biogeochemical Cycles*, 7, 843–878, <https://doi.org/10.1029/93GB02263>, 1993.
- Tang, Q., Mu, L., Sidorenko, D., Goessling, H., Semmler, T., and Nerger, L.: Improving the ocean and atmosphere in a coupled ocean–atmosphere model by assimilating satellite sea-surface temperature and subsurface profile data, *Quarterly Journal of the Royal Meteorological Society*, 146, 4014–4029, <https://doi.org/10.1002/qj.3885>, 2020.
- 1240 Terhaar, J., Frölicher, T. L., and Joos, F.: Observation-constrained estimates of the global ocean carbon sink from Earth system models, *Biogeosciences*, 19, 4431–4457, <https://doi.org/10.5194/bg-19-4431-2022>, 2022.

- 1245 Terhaar, J., Goris, N., Müller, J. D., DeVries, T., Gruber, N., Hauck, J., Perez, F. F., and Séférian, R.: Assessment of Global Ocean Biogeochemistry Models for Ocean Carbon Sink Estimates in RECCAP2 and Recommendations for Future Studies, *Journal of Advances in Modeling Earth Systems*, 16, e2023MS003 840, <https://doi.org/10.1029/2023MS003840>, 2024.
- Timmermann, R. and Beckmann, A.: Parameterization of vertical mixing in the Weddell Sea, *Ocean Modelling*, 6, 83–100, [https://doi.org/10.1016/S1463-5003\(02\)00061-6](https://doi.org/10.1016/S1463-5003(02)00061-6), 2004.
- 1250 Tsujino, H., Urakawa, S., Nakano, H., Small, R. J., Kim, W. M., Yeager, S. G., Danabasoglu, G., Suzuki, T., Bamber, J. L., Bentsen, M., Böning, C. W., Bozec, A., Chassignet, E. P., Curchitser, E., Boeira Dias, F., Durack, P. J., Griffies, S. M., Harada, Y., Ilicak, M., Josey, S. A., Kobayashi, C., Kobayashi, S., Komuro, Y., Large, W. G., Le Sommer, J., Marsland, S. J., Masina, S., Scheinert, M., Tomita, H., Valdivieso, M., and Yamazaki, D.: JRA-55 based surface dataset for driving ocean–sea-ice models (JRA55-do), *Ocean Modelling*, 130, 79–139, <https://doi.org/10.1016/j.ocemod.2018.07.002>, 2018.
- 1255 Valsala, V. and Maksyutov, S.: Simulation and assimilation of global ocean pCO₂ and air–sea CO₂ fluxes using ship observations of surface ocean pCO₂ in a simplified biogeochemical offline model, *Tellus B: Chemical and Physical Meteorology*, 62, 821–840, <https://doi.org/10.1111/j.1600-0889.2010.00495.x>, 2010.
- Verdy, A. and Mazloff, M. R.: A data assimilating model for estimating Southern Ocean biogeochemistry, *Journal of Geophysical Research: Oceans*, 122, 6968–6988, <https://doi.org/10.1002/2016JC012650>, 2017.
- 1260 Vetra-Carvalho, S., van Leeuwen, P. J., Nerger, L., Barth, A., Altaf, M. U., Brasseur, P., Kirchgessner, P., and Beckers, J.-M.: State-of-the-art stochastic data assimilation methods for high-dimensional non-Gaussian problems, *Tellus A: Dynamic Meteorology and Oceanography*, 70, 1–43, <https://doi.org/10.1080/16000870.2018.1445364>, 2018.
- Völker, C., Wallace, D. W. R., and Wolf-Gladrow, D. A.: On the role of heat fluxes in the uptake of anthropogenic carbon in the North Atlantic, *Global Biogeochemical Cycles*, 16, 85–1–85–9, <https://doi.org/10.1029/2002GB001897>, 2002.
- Wanninkhof, R.: Relationship between wind speed and gas exchange over the ocean revisited, *Limnology and Oceanography: Methods*, 12, 351–362, <https://doi.org/10.4319/lom.2014.12.351>, 2014.
- 1265 Wanninkhof, R., Park, G.-H., Takahashi, T., Sweeney, C., Feely, R., Nojiri, Y., Gruber, N., Doney, S. C., McKinley, G. A., Lenton, A., Le Quéré, C., Heinze, C., Schwinger, J., Graven, H., and Khatiwala, S.: Global ocean carbon uptake: magnitude, variability and trends, *Biogeosciences*, 10, 1983–2000, <https://doi.org/10.5194/bg-10-1983-2013>, 2013.
- While, J., Totterdell, I., and Martin, M.: Assimilation of pCO₂ data into a global coupled physical-biogeochemical ocean model, *Journal of Geophysical Research: Oceans*, 117, <https://doi.org/10.1029/2010JC006815>, 2012.
- 1270 Williams, N. L., Juranek, L. W., Feely, R. A., Johnson, K. S., Sarmiento, J. L., Talley, L. D., Dickson, A. G., Gray, A. R., Wanninkhof, R., Russell, J. L., Riser, S. C., and Takeshita, Y.: Calculating surface ocean pCO₂ from biogeochemical Argo floats equipped with pH: An uncertainty analysis, *Global Biogeochemical Cycles*, 31, 591–604, <https://doi.org/10.1002/2016GB005541>, 2017.
- Wunsch, C.: *The Ocean Circulation Inverse Problem*, Cambridge University Press, Cambridge, England, UK, <https://doi.org/10.1017/CBO9780511629570>, 1996.